Dissertation

submitted to the

Combined Faculties of the Natural Sciences and Mathematics

of the Ruperto-Carola-University of Heidelberg, Germany

for the degree of

Doctor of Natural Sciences

Put forward by

Nikolay Belov

born in: Leningrad, Russia (the USSR)

Oral examination: April 15th, 2015

Nuclear effects in

atomic and solid state physics

Referees:

Priv.-Doz. Dr. Zoltán Harman

Prof. Dr. Jürgen Berges

Zusammenfassung

Unterschiedliche Kerneffekte in atomaren Systemen und in einer speziellen Klasse von Festkörpern, in unkonventionellen Supraleitern, werden untersucht. Der erste betrachtete Prozess, innere Paarkonversion in Schwerionen, kann eine wichtige Rolle in zahlreichen Streuprozessen spielen, die mit existierenden oder zukünftigen hochenergetischen Schwerionen-Beschleunigeranlagen untersucht werden. Es wurde festgestellt, dass die Kernanregungsrate und damit die Anzahl der erzeugten Paare stark durch planare Gitterführung der Ionen durch einen Kristall erhöht wird. Der zeitinvertierte Prozess zur Paarkonversion, resonante Kernanregung durch Positronenannihilation, ist ein alternativer Mechanismus in der Wechselwirkung von Positronen mit Materie, und stellt einen zustandsselektiven Weg der Kernanregung dar, der komplementär zu Photo- und Coulomb-Anregung ist. Weiterhin werden Effekte der schwachen Wechselwirkung im Zusammenhang mit Paritätsverletzung in unkonventionellen p-Wellen-Supraleitern untersucht. Wir schlagen Schemata zur effizienten Erhöhung des Effekts vor, so dass dieser zukünftig experimentell untersucht werden kann. Die betrachteten Effekte stellen neue Phänomene an der Schnittstelle von Atom- und Kernphysik und Quantenelektrodynamik dar, und bieten effektive Möglichkeiten zur Untersuchung von fundamentalen Wechselwirkungen.

Abstract

Various nuclear effects in atomic systems and in a particular type of solids, namely, in unconventional superconductors, are investigated. The first process considered, internal pair conversion in heavy ions, can play an important role in numerous scattering processes to be examined at existing or upcoming high-energy heavy-ion-accelerator facilities. The rate of nuclear excitation and thus the number of created pairs is found here to be strongly increased by ion planar channeling through a crystal. The time-reversed process of pair conversion, nuclear excitation by resonant positron annihilation, provides an alternative mechanism of positron-matter interaction and constitutes a state-selective way to excite nuclei which is complementary to photo- and Coulomb excitation. Furthermore, weak-interaction effects are examined in the context of parity violation in unconventional p-wave superconductors. We suggest schemes to efficiently enhance the effect and to enable its future experimental study. The considered effects represent new phenomena at the interface of atomic and nuclear physics and quantum electrodynamics, and provide effective ways to investigate fundamental interactions.

Within the framework of this thesis, the following article has been published in refereed journals:

- ”State-selective high-energy excitation of nuclei by resonant positron annihilation” [1]
  N. A. Belov, Z. Harman, Phys. Lett. B 741, 61 (2015).

The following articles have been submitted or are in preparation for publication in refereed journals:

- ”Parity violation effects in the Josephson junction of a p-wave superconductor” [2]
  N. A. Belov, Z. Harman, submitted (2014); arXiv:1411.1878.
- ”Pair creation in heavy ion channeling” [3]
  N. A. Belov, Z. Harman, submitted (2014); arXiv:1411.5711.
- ”Theory of nuclear excitation by resonant positron annihilation” [4]
  N. A. Belov, Z. Harman, in preparation.
- ”Bound-free and free-free pair production processes in muonic atoms” [5]
  N. A. Belov, Z. Harman, in preparation.

Contents

Introduction **3**
§ 1 Nuclear effects in atoms . . . 3
§ 2 Parity violation as a nuclear effect in atoms and in solid state . . . 4
§ 3 Nuclear effects investigated in the present work . . . 5

I Internal pair conversion **9**
§ 4 Introduction to internal pair conversion . . . 9
§ 5 Probability of the process . . . 10
§ 6 Multipole transitions ($L > 0$) . . . 12
§ 7 Monopole transitions ($L = 0$) . . . 16
§ 8 Numerical results . . . 17
§ 9 Suitable nuclear transitions . . . 22
§ 10 Discussion . . . 25

II Pair creation in muonic atoms **27**
§ 11 Introduction to pair creation in muonic atoms . . . 27
§ 12 Pair creation coefficient for muonic atoms . . . 28
§ 13 A comment concerning free-free pair creation . . . 30
§ 14 Numerical results . . . 31
§ 15 Discussion . . . 34

III Nuclear excitation by resonance positron annihilation **37**
§ 16 Introduction to nuclear excitation by resonance positron annihilation . . . 37
§ 17 Calculation of excitation rates . . . 39
§ 18 Proposed schemes for an experimental observation . . . 42
§ 19 Numerical results for different elements . . . 44
§ 20 Discussion . . . 47

IV Internal pair conversion following Coulomb excitation **49**
§ 21 Introduction to internal pair conversion following Coulomb excitation . . . 49
§ 22 Coulomb excitation cross section in a non-relativistic approach . . . 50
§ 23 Cross section of the 2-step process . . . 52
§ 24 Numerical results in a non-relativistic approach . . . 53
§ 25 Coulomb cross section and the cross section of the 2-step process in a relativistic approach . . . 55

§ 26 Comparison to the non-resonant process 56

V Pair creation in heavy ion channeling **59**
§ 27 Introduction to pair creation in heavy ion channeling 59
§ 28 Virtual photons in ion channeling 60
§ 29 Direct pair creation process 61
§ 30 Pair creation proceeding via nuclear resonances 63
§ 31 Discussion 65

VI Parity violation in unconventional superconductors **67**
§ 32 Introduction to parity violation in unconventional superconductors 67
§ 33 Parity violation in superconductors 69
§ 34 Possible method for the measurement of the f-parameter 72
§ 35 Possible experimental setup to increase the parity violation effect 75
§ 36 Discussion 76

Summary and outlook **79**

Appendix A Evaluation of the radial integrals of the internal pair conversion matrix elements **83**

Appendix B Cross section for a two-step process **87**

Appendix C Mean spin value **93**

Bibliography **97**

Introduction

Historically, the theory of the atomic nucleus has been developed separately from other physical theories [6]. This is mostly caused by the presence of non-electromagnetic interactions, binding nucleons together in a compound system. For the description of the nucleus one needs to also account for the weak and strong interactions of the Standard Model. This explains the complexity of nuclear models. Furthermore, nuclei are usually studied not separately, but as a part of some system, for instance, an atom or a crystal.

In a basic approximation, these systems can be described as containing point-like nuclei, which are characterized by their composite charge, and interact with electrons and other nuclei by the Coulomb force; effects associated with the nuclear structure are, therefore, neglected. This simple model explains a plethora of different phenomena in atomic and solid-state physics. The internal nuclear configuration typically produces only small corrections to the description of atomic and solid-state systems [6]. However, these deviations can in certain cases carry significant information about both nuclear structure and the properties of the fundamental interactions.

§ 1 Nuclear effects in atoms

Several nuclear effects are well-known in atomic physics. These fundamental processes can be categorized as follows:

Static effects

Firstly, the main contributions to the atomic spectrum stemming from the nucleus are provided by effects known since the early 1930s. The basic fundamental phenomena of this kind are: the spectral shifts caused by finite nuclear size and finite nuclear mass [7, 8]; the influence of the nuclear spin on electron spectra [9]; the nuclear contribution to the hyperfine structure [10, 11]; and the Zeeman effect of the hyperfine structure [12]. All these phenomena are rather well understood nowadays, therefore, for a detailed description one can refer to any textbook on atomic physics, for instance, Ref. [13]. These hyperfine effects are however strongly enhanced in heavy highly charged ions. Modern experiments with ions such us hydrogenlike or lithiumlike Bi and Ho provide insight into nuclear structure via the nuclear magnetic moment, and also allow tests of quantum electrodynamics in the strongest electric fields available [14].

Modern atomic structure calculations involving quantum electrodynamic corrections give very precise results, which can be experimentally tested to ultimate accuracy. Therefore, it is crucial for some of these calculations to take nuclear properties into account. As an exam-

ple, one may consider the theoretical and experimental investigation of the electron mass [15]. In this work, an extremely accurate measurement of the magnetic moment of a hydrogenlike carbon ion is combined with a g-factor calculation in the framework of bound-state quantum electrodynamics, to yield the atomic mass of the electron with a 10^{-11} relative precision. At this level, even the otherwise minor nuclear effects contribute significantly.

Dynamical effects

Another group of nuclear effects in atoms is connected with nuclear processes dynamically involving atomic electrons. The most fundamental effect of this type is internal conversion, i.e., deexcitation of an atomic nucleus by transfer of its excitation energy to the ionization of one of the bound electrons [16]. The inverse process, i.e. nuclear excitation by electron capture, has also been predicted, however, it has not been observed yet (see e. g. Ref. [17]). Nuclear deexcitation by β-decay can initiate processes in atomic shells: for instance, in proton-rich nuclear systems having sufficient energy for the β^+ decay one can also observe nuclear decay by electron capture, i.e. a process in which a nuclear proton absorbs an inner atomic electron, thereby producing a neutron and causing the simultaneous emission of an electron neutrino. For the first experimental observation of electron capture one can refer to Ref. [18].

It is possible to examine further processes such as bound-free internal pair conversion, where an atomic nucleus produces within its deexcitation an electron-positron pair with the electron in a bound state of the same atom. The study of nuclear transitions involving atomic electrons is relevant as it allows to improve our understanding of both atomic and nuclear structure, as well as the transfer of energy between these subsystems. This can also lead to several practical applications, directly related to the interactions of matter with charged particles, ranging from electrons and positrons to heavy ions.

§ 2 Parity violation as a nuclear effect in atoms and in solid state

The next phenomenon considered in this work is the electroweak interaction between the nucleus and electrons. The main observable effect in this case is provided by the parity-violating terms of the weak interaction, since they change the parity of electronic states and can be observed on the strong background of electromagnetic forces. The observation of this effect is appealing for both atomic and solid-state physics.

The parity violation has been firstly detected experimentally in the beta decay of cobalt-60 in 1957 by C. S. Wu and collaborators [19]. Later many other experimental schemes for its observation and investigation have been realized. For instance, in atomic physics, parity-violation experiments have been performed by the observation of the forbidden M1 transition $7s_{1/2} \to 6s_{1/2}$ in cesium, which possesses a symmetry-breaking admixture of the $6p_{1/2}$ electron state with its neighboring state $7s_{1/2}$ (Ref. [20]).

In solid-state physics, the parity-violating terms of the electroweak interaction between electrons and nuclei of the crystal lattice can have a slight influence on conducting and superconducting properties of the material [21]. One of the solid-state systems where one can propose to measure the symmetry-breaking contribution is an unconventional superconductor. The main

advantage of the investigation of parity violation in superconductors is the compact size of the experimental setup in comparison to modern accelerator-based experimental techniques. It is also of academic interest to see whether such a microscopic effect can manifest itself on the macroscopic scale.

§ 3 Nuclear effects investigated in the present work

This work presents an investigation of several not yet fully studied nuclear contributions in atomic physics, as well as in a special solid-state system, namely, in unconventional superconductors. The atomic effects considered in this work are: internal pair conversion with the creation of a free or bound electron; internal pair conversion following Coulomb excitation; pair creation in heavy ion channeling; pair production in muonic atoms; and nuclear excitation by resonance positron annihilation. Finally, we discuss parity violation in unconventional superconductors.

The first considered process is *internal pair conversion in heavy ions*. A considerable variety of particles can be produced in nucleus-nucleus collisions involving heavy ions. Among these particles one may observe outgoing positrons in coincidence with the change of the charge of the target ion. They can be created either in direct electron-positron pair production by a virtual photon with simultaneous capture of an electron to an atomic bound state [22], or through a nuclear excitation, followed by bound-free nuclear pair conversion. In the second case, the positrons created are monochromatic, i.e. their kinetic energy is well defined by energy conservation. These fundamental schemes can play an important role in numerous processes which are going to be examined at the Facility for Antiproton and Ion Research (FAIR) in the nearest future [23]. In the framework of FAIR experiments it will be possible to consider the bound-free and free-free pair production in the Coulomb field of heavy ions within their collision. Therefore, it is important to investigate the pair conversion process itself, as well as in a combination with the *Coulomb excitation of the nucleus*, as a mechanism to populate nuclear levels with MeV energies.

Furthermore, we investigate whether the rate of excited nuclei or the number of created pairs can be increased by the implementation of *ion planar channeling* through a crystal at certain resonance conditions [24]. In this case, after multiple interfering interactions, the nucleus is excited with a significantly enhanced probability, therefore, we expect that the rate of pairs created by the corresponding deexcitation also increases. This technique for the enhancement of pair production is also investigated in the present work.

Generally, pair creation in strong electromagnetic fields, such the Coulomb fields of heavy colliding ions combined for a short time or the crystal field in channeling, provide alternatives to pair production in optical or X-ray lasers fields [25]. Therefore, the study of such mechanisms is of significance in fundamental research in quantum electrodynamics, connected with fermion production in strong electromagnetic fields (see, e. g. Ref. [26–29]).

The pair-creation process can also be studied in a more exotic system, namely, in *muonic atoms*. The muonic atom is a system consisting of a nucleus, bound electrons, and at least one muon in a bound atomic state. The investigation of muonic atoms is of importance for several applications. For instance, muonic hydrogen has been used in precise experiments for the determination of the proton radius [30], exploiting the much higher overlap of bound muons

with the nucleus, as compared to bound electrons. Usually, muonic atoms are created with a muon occupying a highly excited state, causing a cascade transition of the muon to the lowest-possible state [31]. Having an approximately 200 times larger mass than an electron, in heavier atoms, a muon can produce a pair of an electron and a positron within its transition between low-lying bound atomic states. Therefore, the investigation of the pair production with both a bound or a free electron created is relevant for muonic cascade studies. This deexcitation mechanism is also studied in this work.

The time-reversed process of internal pair conversion can play a role in the interaction of positrons with matter. Positron collisions with atomic matter lead to a number of processes [32–36], among which annihilation with shell electrons is one of the most prominent effects. Typically, annihilation leads to the emission of gamma rays. Alternatively, the same nucleus may resonantly absorb the whole energy of the annihilating particles and become excited. This single-step process is termed *Nuclear Excitation by Resonant Positron Annihilation (NERPA)*. NERPA constitutes a way to excite nuclei which is alternative to photo- and Coulomb excitation. The great advantage of photo-excitation is the monochromacity of the X- or γ-ray beam and the resonant character of the excitation. The accessible transitions are, however, of electric dipole ($E1$) type. On the other hand, Coulomb excitation, i.e. the excitation by the inelastic scattering of massive charged particles, may induce transitions of arbitrary multipolarities, however, without any selectivity of the nuclear energy levels. NERPA has an attractive combination of the above advantages: the resonant character of the excitation and a significant cross section regardless of the multipolarity. In particular, NERPA can resonantly induce monopole transitions. A possibility to excite such transitions is particularly important for studies of deformed nuclei. Another important application is a collective nuclear excitation, the giant monopole resonance [37,38]. In the case of giant nuclear resonances of any multipolarity, NERPA bears all the above-mentioned advantages of Coulomb excitation.

Weak interaction effects are discussed in the present work by focusing on *parity violation phenomena in superconductors*. The idea that parity violation effects can appear in superconductors was proposed by A.I. Vainstein and I.B. Khriplovich in 1974 [21]. It has been shown in that work that this electroweak contribution is negligibly small in conventional s-wave superconductors. The theoretical treatment of this effect in unconventional p-wave ferromagnetic superconductor is presented in this work. In these materials superconducting and ferromagnetic phases may coexist, which helps to improve the effect. Our calculation shows that the parity violation effect is significantly stronger in our systems than for the s-wave case. We also suggest novel methods for the measurement and control of the effect, yielding further enhancements.

To cover all the mentioned phenomena, this thesis is organized as follows. In Chapter I, the pair conversion mechanism in ions is discussed. Here, the main analytical formulas are derived, which are used in most of the following parts of this work. Two cases of internal pair conversion , namely, the cases when a free or a bound electron is created, are compared in different atoms and energy regions. In order to perform quantitative investigations, the pair conversion coefficients have been introduced. They are defined as the ratio of the probability of

a certain type of pair conversion to the probability of γ emission in the same nuclear transition. Certain mathematical derivations related to this Chapter are given in Appendix A.

Chapter II is devoted to pair production in muonic atoms. Here, we also have to take into account the nuclear size contribution in the wave functions of the bound muon. The main improvement of our theoretical description is required by the presence of vacuum polarization corrections, which are described in this work in terms of the Uehling potential [39]. The results of corresponding numerical investigations show very similar dependencies of the pair production rates on energy and nuclear charge as in the nuclear internal conversion case.

Chapter III contains the investigation of nuclear excitation by resonance positron annihilation. On the one hand, from the point of view of analytical derivations, the description of this process does not differ much from that of internal pair conversion. On the other hand, it is promising for possible applications, therefore, it is rather relevant to find special situations where the contribution of NERPA is significant. Such cases with corresponding numerical investigations are discussed in Chapter III, with some derivations presented in Appendix B.

Chapter IV describes pair production following Coulomb excitation and Chapter V demonstrates the significant increase of the corresponding rate of the nuclear excitation by the implementation of ion planar channeling through a crystal. The nuclear excitation is described in this case in terms of the interaction with equivalent photons in the crystal. For the deexcitation step the results for internal pair conversion received in Chapter I are incorporated.

The final Chapter VI presents the investigation of parity violation properties of the weak interaction. This property is studied in unconventional superconductors. Therefore, the corresponding theory is formulated in Chapter VI and in Appendix C.

Chapter I

Internal pair conversion

§ 4 Introduction to internal pair conversion

The creation of particle-antiparticle pairs from vacuum [40] is one of the most intriguing features of quantum field theory. A broad variety of pair creation mechanisms have been predicted and experimentally observed, e.g., in intense optical or X-ray fields [25, 41–51], in ion-ion [52–56], ion-photon [22] and ion-electron [57] collisions, in tokamak plasmas [58], as well as in astrophysical environments such as, e.g., pulsars [59]. In projected experiments at the Facility for Antiproton and Ion Research (FAIR), it will be possible to study pair creation in the Coulomb field of heavy ions during their collision [23].

The study of an alternative mechanism of electron-positron pair creation, the bound-free internal electron-positron pair creation is put forward in this Chapter [see Fig. 4.1]. This process presents a new channel of nuclear deexcitation by the creation of an electron-positron pair with the electron occupying a discrete atomic state in the same atom, while the positron, due to its positive charge, is created in a free (unbound) state. The corresponding free-free process with both fermions created as free has been described for the first time in the work of Rose and Uhlenbeck [60] and has been experimentally observed by Bloom [61]. A complete theory of the free-free process has been introduced by Soff, Schlüter and Greiner for nuclear transitions with angular momenta $L > 0$ [62] and for electric monopole (E0) transitions [63]. The second case is of interest since it relates to a radiationless transition, i.e. only internal conversion and the pair conversion process are allowed. Furthermore, in the case of a bare ion in absence of atomic electrons, even internal conversion is forbidden and bound-free and free-free pair production are the only possible electromagnetic decay channels.

It has been noticed by Soff and coworkers [63] that the bound-free process is naturaly rare, since it requires a vacant bound electron state with a large overlap with the nucleus. The situation can be changed in the case of a bare heavy ion or in a heavy ion with the vacant $1s_{1/2}$-state for the created electron. Therefore, the calculations are provided in the present Chapter for heavy ions. The cases when the bound-free process can be comparable to or even can have a greater contribution than the free-free process are also discussed here. These cases are relevant for different applications in atomic physics and astrophysics, to be discussed later in Chapter III.

In this Chapter the theoretical description of the bound-free internal pair conversion process is presented. This theoretical study is accompanied by results of numerical calculations. Some suitable nuclear transitions are shown correspondingly where bound-free pair conversion has a significant contribution.

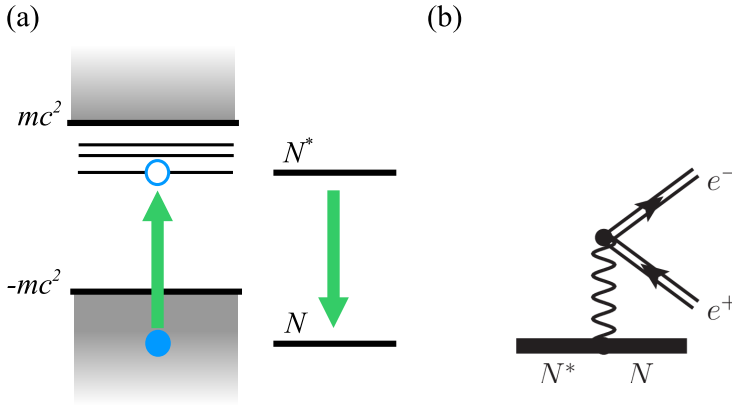

Figure 4.1 – (a) The illustration of internal pair conversion by the corresponding nuclear and fermionic level schemes. mc^2 is the rest energy of the electron, and N^* (N) denotes the nuclear initial (final) state. (b) The leading Feynman diagram of internal pair conversion. Thick lines denote nuclear states, double lines denote fermions in the Coulomb field of the nucleus, and the wave line represents a virtual photon exchanged between the nucleus and the electron-positron field. Here, the electron created may be bound or unbound.

§ 5 Probability of the process

Let us consider the electromagnetic Hamiltonian for an atomic system consisting of the nucleus and fermions (electrons and positrons) as a sum of the unperturbed (H_0) and perturbation (interaction, H_I) parts,

$$H = H_0 + H_I. \tag{5.1}$$

It is possible to construct the S-matrix, which connects the initial and final states of the system:

$$|f\rangle = |t = +\infty\rangle = S\,|t = -\infty\rangle = S\,|i\rangle, \tag{5.2}$$

where the initial (i) and final (f) wave functions are eigenfunctions of the free Hamiltonian H_0. As follows from the S-matrix theory, this matrix is defined by the equation [64]:

$$S = T\left[e^{-i\int d^4x H_I(x)}\right], \tag{5.3}$$

where T is the Wick time-ordering operator, x is a 4-dimensional Minkovsky-space vector. With the help of the Wick theorem [64], written for some functional $S_V(\phi_1, .., \phi_m)$ of the quantum fields $\phi_1, .., \phi_m$ participating in the considered process, one can reduce T-ordering to normal N-ordering:

$$T\left[e^{iS_V(\phi_1 ... \phi_m)}\right] = N\left[e^{1/2\sum_{i,j}\frac{\delta}{\delta\phi_i}\Delta_{ij}\frac{\delta}{\delta\phi_j}} e^{iS_V(\phi_1 ... \phi_m)}\right]. \tag{5.4}$$

In this equation the convolution operator is $\Delta_{ij} = \langle f|T[\phi_i\phi_j]|i\rangle$.

For our case of interest – the description of the nuclear-electron interaction – one operates with 3 quantum fields: $\Psi(x)$ for the nucleus, $\psi(x)$ for fermions, and $A(x)$ for photons. Furthermore, only the convolutions between fields with the same nature appear to be non-zero. In

common notations, these non-zero convolutions are [64]:

$$\Delta_\Psi(x_1,x_2) = \langle f|T[\overline{\Psi}(x_1)\Psi(x_2)]|i\rangle, \tag{5.5}$$
$$\Delta_\psi(x_1,x_2) = \langle f|T[\overline{\psi}(x_1)\psi(x_2)]|i\rangle, \tag{5.6}$$
$$\Delta_A^{\mu\nu}(x_1,x_2) = \langle f|T[A^\mu(x_1)A^\nu(x_2)]|i\rangle. \tag{5.7}$$

Here, x_1 and x_2 are also 4-dimensional vectors. The bar over the field operators' symbols means the complex conjugate. The interaction part of the Hamiltonian is [65]:

$$H_I(x) = e\overline{\psi}(x)\gamma_\mu\psi(x)A^\mu(x) + e\overline{\Psi}(x)\gamma_\mu\Psi(x)A^\mu(x), \tag{5.8}$$

where e is the unit charge and γ^μ are the Dirac matrices [64] with $\mu = 0, 1, 2, 3$. For Greek indexes, the Einstein summation convention is assumed here. The first nonzero contribution to the S-matrix appears to be of second order. The present calculation is restricted to this contribution. One can derive the second order of the S-matrix using Eqs. (5.3-5.8). Here, only the contributions containing all 3 fields are presented:

$$\begin{aligned} S^{(2)} = {} & \frac{-e^2}{2}\Big(N[\overline{\Psi}(x_1)\gamma_\mu\Psi(x_1)\overline{\psi}(x_2)\gamma_\nu\psi(x_2)] + N[\Delta_\Psi(x_1,x_2)\gamma_\mu\psi(x_1)\overline{\psi}(x_2)\gamma_\nu] \\ & + N[\Delta_\psi(x_2,x_1)\overline{\Psi}(x_1)\gamma_\mu\gamma_\nu\Psi(x_2)] + \Delta_\Psi(x_1,x_2)\Delta(x_2,x_1)_\psi\gamma_\mu\gamma_\nu\Big) \\ & \times\Big(N[A^\mu(x_1)A^\nu(x_2)] + \Delta_A^{\mu\nu}(x_1,x_2)\Big). \end{aligned} \tag{5.9}$$

Furthermore, since we consider the a situation with external nuclear and fermionic lines, and a virtual photon mediating the electromagnetic interaction, the only term of $S^{(2)}$ that survives is

$$S^{(2)} = \frac{-e^2}{2}N\left[\overline{\Psi}(x_1)\gamma_\mu\Psi(x_1)\overline{\psi}(x_2)\gamma_\nu\psi(x_2)\right]\Delta_A^{\mu\nu}(x_1,x_2). \tag{5.10}$$

It contains the photon propagator of the form [64]:

$$\Delta_A(x_1,x_2) = -\frac{ig^{\mu\nu}}{(2\pi)^4}\int d^4k\frac{e^{-ik(x_1-x_2)}}{k^2+i\cdot 0}, \tag{5.11}$$

where $g^{\mu\nu}$ is the metric tensor, and the integration is performed over the 4-momentum k of the photon. The small imaginary part $+i\cdot 0$ defines the integration contour within the integration of this function near its pole. The fermion part becomes a product of nuclear and electronic 3-currents, and the time-dependent part contains electron, positron and nuclear decay energies (E, E' and ω, correspondingly). Therefore, the $S^{(2)}$-matrix element has the form [62]:

$$\begin{aligned} S_{if}^{(2)} = {} & \frac{+ie^2}{(2\pi)^4}\int d\vec{r}_n\int d\vec{r}_e\, j_n(\vec{r}_n)j_e(\vec{r}_e) \\ & \times \int d\vec{k}e^{i\vec{k}(\vec{r}_n-\vec{r}_e)}\int dk_0\frac{1}{\vec{k}^2-k_0^2-i0}\int dt_e e^{i(E+E'+k_0)t_e}\int dt_n e^{-i(\omega+k_0)t_n}. \end{aligned} \tag{5.12}$$

The last two integrals evaluate to Dirac δ-functions, therefore, after integration over k_0, one can obtain [62]:

$$S_{fi}^{(2)} = \frac{ie^2}{(2\pi)^2}\int d\vec{r}_n\int d\vec{r}_e\, j_n(\vec{r}_n)j_e(\vec{r}_e)\int d\vec{k}\frac{e^{i\vec{k}(\vec{r}_n-\vec{r}_e)}}{\vec{k}^2-\omega^2-i0}\delta(E+E'-\omega). \tag{5.13}$$

The evaluation of the integral over the photon momentum leads to [62]

$$S^{(2)}_{fi} = -2\pi i U^{(2)}_{fi}\delta(E+E'+\omega), \tag{5.14}$$

$$U^{(2)}_{fi} = -\alpha\int d\vec{r}_n\int d\vec{r}_e\, j_n(\vec{r}_n)\, j_e(\vec{r}_e)\frac{e^{i\omega|\vec{r}_n-\vec{r}_e|}}{|\vec{r}_n-\vec{r}_e|}, \tag{5.15}$$

where α is the fine-structure constant. Therefore, the transition probability is given as a sum over the magnetic quantum numbers of initial and final nuclear states, as well as over the Dirac angular momentum quantum numbers κ, κ' of the created electron and positron, and over their magnetic quantum numbers [62]:

$$P_{e^-_b e^+_f} = \frac{2\pi}{2J_i+1}\sum_{M_i=-J_i}^{J_i}\sum_{M_f=-J_f}^{J_f}\sum_{\substack{\kappa=-\infty\\ \kappa\neq 0}}^{\kappa=+\infty}\sum_{\substack{\kappa'=-\infty\\ \kappa'\neq 0}}^{\kappa'=+\infty}\sum_{\mu=-j}^{j}\sum_{\mu'=-j'}^{j'} W, \tag{5.16}$$

$$W = 2\pi|U^{(2)}_{if}|\delta(E+E'-\omega).$$

Here, J_i and J_f are the angular momenta of the nuclear initial and final states and j and j' are angular momenta of the electron and positron states.

§ 6 Multipole transitions ($L > 0$)

As has been noticed in Ref. [62], the derivations of the free-free pair conversion equations are different for the cases when the nuclear transition momentum L is equal or non-equal to zero. The same is valid in the bound-free case. In analogy with the free-free pair conversion coefficient for the case $L > 0$: $\beta_{\rm ff} = P_{e^-_f e^+_f}/P_\gamma$ [62] – ratio of the pair production probability and the gamma emission probability – the bound-free pair conversion coefficient can be defined as:

$$\beta_{\rm bf} = P_{e^-_b e^+_f}/P_\gamma. \tag{6.1}$$

The equation for $\beta_{\rm bf}$ can be derived in a similar way to $\beta_{\rm ff}$ [62], with the substitution of a bound wave function for the created electron instead of one belonging to the continuous spectrum. We provide our derivation in the zero nuclear radius assumption with the help of Refs. [22, 62, 65]. First of all, due to the theoretical achievements of the last section [see Eq. 5.16], the bound-free pair production probability is:

$$P_{e^-_b e^+_f} = \frac{-4\pi^2\alpha}{2J_i+1}\sum_{M_i=-J_i}^{J_i}\sum_{M_f=-J_f}^{J_f}\sum_{\substack{\kappa=-\infty\\ \kappa\neq 0}}^{\kappa=+\infty}\sum_{\substack{\kappa'=-\infty\\ \kappa'\neq 0}}^{\kappa'=+\infty}\sum_{\mu=-j}^{j}\sum_{\mu'=-j'}^{j'} \tag{6.2}$$

$$\left|\int_0^\infty d\vec{r}_n\int_0^\infty d\vec{r}_e\, j_n(\vec{r}_n)\, j_e(\vec{r}_e)\frac{\exp i\omega|\vec{r}_n-\vec{r}_e|}{|\vec{r}_n-\vec{r}_e|}\right|^2\delta(E+E'-\omega).$$

The integrations are performed over electron and nuclear coordinates. δ-function determines the energy relation between the electron (E'), the positron (E) and the photon (ω), emitted by the nucleus.

By substituting 4-currents by 3-currents and charge densities, one can rewrite the integrals in Eq. (6.2) similarly to Ref. [62] as:

$$-\alpha \int_0^\infty d\vec{r}_n \int_0^\infty d\vec{r}_e \left(\rho_n(\vec{r}_n)\rho_e(\vec{r}_e) - \vec{j}_n(\vec{r}_n)\hat{I}\vec{j}_e(\vec{r}_e)\right) \frac{\exp i\omega|\vec{r}_n - \vec{r}_e|}{|\vec{r}_n - \vec{r}_e|} = \sum_{L=1}^{\infty}\sum_{M=-L}^{L} (U^m(L,M) + U^e(L,M)) + U^0, \tag{6.3}$$

with

$$\begin{aligned} U^e &= 4\pi i\alpha\omega \left(\sum_{\tau=e,l} \int_0^\infty d\vec{r}_n \int_{r_n}^\infty d\vec{r}_e \vec{j}_n(\vec{r}_n) A_L^{M(\tau)^*}(\omega\vec{r}_n) \vec{j}_e(\vec{r}_e) B_L^{M(\tau)}(\omega\vec{r}_e) \right. \\ &+ \sum_{\tau=e,l} \int_0^\infty d\vec{r}_n \int_0^{r_n} d\vec{r}_e \vec{j}_n(\vec{r}_n) B_L^{M(\tau)^*}(\omega\vec{r}_n) \vec{j}_e(\vec{r}_e) A_L^{M(\tau)}(\omega\vec{r}_e) \\ &- \int_0^\infty d\vec{r}_n \int_{r_n}^\infty d\vec{r}_e \rho_n(\vec{r}_n) j_L(\omega\vec{r}_n) Y_L^{M*}(\vec{n}_{r_n}) \rho_e(\vec{r}_e) h_L(\omega\vec{r}_e) Y_L^M(\vec{n}_{r_e}) \\ &\left. + \int_0^\infty d\vec{r}_n \int_0^{r_n} d\vec{r}_e \rho_n(\vec{r}_n) h_L(\omega\vec{r}_n) Y_L^{M*}(\vec{n}_{r_n}) \rho_e(\vec{r}_e) j_L(\omega\vec{r}_e) Y_L^M(\vec{n}_{r_e}) \right), \end{aligned} \tag{6.4}$$

$$\begin{aligned} U^m &= 4\pi i\alpha\omega \left(\int_0^\infty d\vec{r}_n \int_{r_n}^\infty d\vec{r}_e \vec{j}_n(\vec{r}_n) A_L^{M(m)^*}(\omega\vec{r}_n) \vec{j}_e(\vec{r}_e) B_L^{M(m)}(\omega\vec{r}_e) \right. \\ &\left. + \int_0^\infty d\vec{r}_n \int_0^{r_n} d\vec{r}_e \vec{j}_n(\vec{r}_n) B_L^{M(m)^*}(\omega\vec{r}_n) \vec{j}_e(\vec{r}_e) A_L^{M(m)}(\omega\vec{r}_e) \right), \end{aligned} \tag{6.5}$$

$$U^0 = -\alpha \int_0^\infty d\vec{r}_n \int_0^{r_n} d\vec{r}_e \rho_n(\vec{r}_n)\rho_e(\vec{r}_e) \left(\frac{1}{r_n} - \frac{1}{r_e}\right), \tag{6.6}$$

where j_L and $h_L \equiv h_L^{(1)}$ are the Bessel and Hankel spherical functions [66], Y_L^M are spherical harmonics, $\vec{n}_r = \vec{r}/r$ denotes the angular part of the vector $\vec{r}$, and the following notations have been introduced [62]:

$$A_L^{M(\tau)}(\omega\vec{r}) = C_L^{M(\tau)}(j_L, \omega\vec{r}), \tag{6.7}$$

$$B_L^{M(\tau)}(\omega\vec{r}) = C_L^{M(\tau)}(h_L, \omega\vec{r}), \tag{6.8}$$

$$C_L^{M(e)}(\zeta_L, \omega\vec{r}) = -\sqrt{\frac{L}{2L+1}}\zeta_{L+1}(\omega r) Y_{LL+1}(\vec{n}_r) + \sqrt{\frac{L+1}{2L+1}}\zeta_{L-1}(\omega r) Y_{LL-1}(\vec{n}_r), \tag{6.9}$$

$$C_L^{M(m)}(\zeta_L, \omega\vec{r}) = -\zeta_L(\omega r) Y_{LL}^M(\vec{n}_r), \tag{6.10}$$

$$Y_{LL'}^M(\vec{n}) = (-1)^{L+M}\sqrt{2L+1} \sum_\mu \begin{pmatrix} 1 & L' & L \\ -\mu & M+\mu & -M \end{pmatrix} Y_{L'}^{M+\mu}(\vec{n})\xi_{-\mu}, \tag{6.11}$$

where the spherical unit vectors are:

$$\xi_0 = e_z, \tag{6.12}$$

$$\xi_{\pm 1} = \mp\frac{1}{\sqrt{2}}(e_x \pm i e_y). \tag{6.13}$$

Following Eq. (6.6) it is important to stress that one has to assume some nuclear model (e. g. the nuclear drop model) for the nuclear charge distribution and performe an integration for the calculation of the internal pair production coefficient in the case of electrical monopole (E0) nuclear transitions.

However, the further derivation of U^e and U^m involves a splitting of the double integral over nuclear and fermionic coordinates into a product of nuclear and fermionic parts. This can be performed in the non-penetration approximation, where the overlap integral of the bound-electron wave function within the nuclear volume is neglected. This simplification is generally used in the calculation of quantities related to the interaction of shell electrons with the nucleus [62, 63, 67, 68]. The full description of this procedure can be found in [62], thus this procedure is shown in the present work on the simple example of U^m only. The equation (6.5) for U^m can be rewritten in the following way [62]:

$$\begin{aligned} U^m &= 4\pi i\alpha\omega\left(\int_0^\infty d\vec{r}_n \int_0^\infty d\vec{r}_e \vec{j}_n(\vec{r}_n) A_L^{M(m)^*}(\omega\vec{r}_n)\vec{j}_e(\vec{r}_e) B_L^{M(m)}(\omega\vec{r}_e)\right. \\ &- \int_0^\infty d\vec{r}_n \int_0^{r_n} d\vec{r}_e \vec{j}_n(\vec{r}_n) A_L^{M(m)^*}(\omega\vec{r}_n)\vec{j}_e(\vec{r}_e) B_L^{M(m)}(\omega\vec{r}_e) \\ &+ \left.\int_0^\infty d\vec{r}_n \int_0^{r_n} d\vec{r}_e \vec{j}_n(\vec{r}_n) B_L^{M(m)^*}(\omega\vec{r}_n)\vec{j}_e(\vec{r}_e) A_L^{M(m)}(\omega\vec{r}_e)\right). \end{aligned} \tag{6.14}$$

In Eq. (6.14), the two last terms are neglected due to the non-penetration assumption. The first term can be written as the product of nuclear and electronic parts [62]:

$$U^m = 4\pi i\alpha\omega V^m_{nucl} M^m. \tag{6.15}$$

The nuclear part disappears in the bound-free pair conversion coefficient $\beta_{\rm bf}$ after dividing by P_γ [see Eq. (6.1)]. Therefore, only the electronic matrix element M^m has to be calculated and the pair conversion coefficient is independent on the nuclear model. A similar result with Eq. (6.15) can be received for electrical transitions (i.e. for U^e).

The next step is the calculation of the fermionic matrix elements in all equations above. The wave functions for the bound electron and the free positron are written in the form [65]:

$$\psi_{jlm}(r,\theta,\phi) = \begin{pmatrix} g_\kappa(r)\Omega_{jlm}(\theta,\phi) \\ i f_\kappa(r)\Omega_{jl'm}(\theta,\phi) \end{pmatrix}, \tag{6.16}$$

where

$$\Omega_{jlm}(\theta,\phi) = \sum_{m_s=\pm 1/2} \langle L1/2 - m_s m_s | jm\rangle Y_{l,m-m_s}(\theta,\phi)\chi_{m_s}. \tag{6.17}$$

Here, the χ_{m_s} are the spinors defined as [65]

$$\chi_{\frac{1}{2}} = \begin{pmatrix} 1 \\ 0 \end{pmatrix} \text{ and } \chi_{-\frac{1}{2}} = \begin{pmatrix} 0 \\ 1 \end{pmatrix}. \tag{6.18}$$

These are coupled using the Clebsch-Gordan coefficients $\langle L1/2 - m_s m_s | jm\rangle$ with the spherical harmonics to form spherical spinors Ω_{jlm}, which are eigenstates of the total angular momentum j. For the Dirac angular momentum quantum numbers it holds: $\kappa = \mp(J + 1/2)$ and $L' = L \pm 1$ for $J = L \pm 1/2$.

In contarast to free-free internal pair production [62], the bound-free case operates with bound radial functions f and g; other issues are the same. Thus, following the derivations of [62], one arrives to an expression for the pair conversion coefficient with the new functions f and g:

$$\beta_{\rm bf}(EL) = \sum_{\kappa\kappa'} \frac{4\pi\alpha\omega}{L(L+1)} |\kappa\kappa'| \times |(\kappa - \kappa')(R_3 + R_4) + L(R_1 + R_2 + R_3 - R_4)|^2 \sigma, \quad (6.19)$$

$$\beta_{\rm bf}(ML) = \sum_{\kappa\kappa'} \frac{4\pi\alpha\omega}{L(L+1)} |\kappa\kappa'| \times |(\kappa + \kappa')(R_5 + R_6)|^2 \sigma, \quad (6.20)$$

where a short-hand notation for a squared $3j$-symbol [69] was introduced:

$$\sigma = \begin{pmatrix} j & j' & L \\ \frac{1}{2} & -\frac{1}{2} & 0 \end{pmatrix}^2. \quad (6.21)$$

This $3j$-symbol embodies the transition selection rules, i.e. it is non-zero when

$$|j - L| \leq j' \leq j + L, \quad (6.22)$$

$$\text{or} \quad (6.23)$$

$$||\kappa| - |\kappa'|| \leq L \leq |\kappa| + |\kappa'| - 1. \quad (6.24)$$

The radial integrals in Eqs. (6.19-6.20) are

$$R_1 = \int_0^\infty g_\kappa g_{\kappa'} h_L(\omega r) r^2 dr, \quad (6.25)$$

$$R_2 = \int_0^\infty f_\kappa f_{\kappa'} h_L(\omega r) r^2 dr, \quad (6.26)$$

$$R_3 = \int_0^\infty f_\kappa g_{\kappa'} h_{L-1}(\omega r) r^2 dr, \quad (6.27)$$

$$R_4 = \int_0^\infty g_\kappa f_{\kappa'} h_{L-1}(\omega r) r^2 dr, \quad (6.28)$$

$$R_5 = \int_0^\infty f_\kappa g_{\kappa'} h_L(\omega r) r^2 dr, \quad (6.29)$$

$$R_6 = \int_0^\infty g_\kappa f_{\kappa'} h_L(\omega r) r^2 dr. \quad (6.30)$$

$$(6.31)$$

The analytical evaluation of these integrals in the point-nucleus approximation is presented in Appendix A. Alternatively, the radial integrals can be calculated assumping a finite nuclear radius. This calculation has to be provided with wave functions obtained from a numerical solution of the Dirac equation containing the potential of an extended nucleus. Computer codes used for our evaluation of such functions can be found in [70]. The results of zero and finite nuclear radius calculations and their comparison are presented in the following sections.

§ 7 Monopole transitions ($L = 0$)

Gamma emission is forbidden for the case of electric-monopole (E0) nuclear transitions, therefore, the coefficient β cannot be introduced as in the previous Section. However, the ratios between probabilities for the bound-free pair production ($P_{\rm bf}$), the free-free process ($P_{\rm ff}$) and internal conversion (P_e) can be used for the characterization of this process. Therefore, the following 4 ratios can be introduced:

$$\eta = P_{\rm ff}/P_e, \tag{7.1}$$
$$\delta_1 = P_{\rm bf}/P_e, \tag{7.2}$$
$$\delta_2 = P_{\rm bf}/P_{\rm ff}, \tag{7.3}$$
$$\delta_3 = \frac{P_{\rm bf}}{P_{\rm bf} + P_{\rm ff} + P_e}. \tag{7.4}$$

The coefficient η has been introduced by Soff et al. in Ref. [63]. The other three coefficients are introduced in this work for the first time. All these coefficients have to be calculated in a certain assumption of the nuclear charge distribution in Eq. (6.6). The first coefficient η has been calculated employing the nuclear drop model in [63]. The other coefficients δ_1–δ_3, which describe the strength of the bound-free pair conversion process, can be also derived in the same assumption. It is natural after considering derivations for the EL and ML cases that the internal pair conversion in the E0 case provides similar formulas as in the case of free-free pair conversion, however, containing the bound wave functions for the electron produced. These results for pair conversion probabilities have the form

$$P_{\rm bf} = \frac{\pi\alpha^2}{9}|M|^2 R^{4\gamma-4}|D_{\rm bf}|^2, \tag{7.5}$$
$$\frac{dP_{\rm ff}}{dE} = \frac{\pi\alpha^2}{9}|M|^2 R^{4\gamma-4}\sum_{\kappa=\pm1}|D_{\rm bf}(\kappa)|^2, \tag{7.6}$$
$$P_e = \frac{\pi\alpha^2}{9}|M|^2 R^{4\gamma-4}|D_e|^2, \tag{7.7}$$

where M is the nuclear transition matrix element, R is the nuclear radius in the liquid nuclear drop model. The summation in the free-free case is taken over the positron's Dirac angular momentum quantum number κ. The modulus square of the electron matrix elements D are given as

$$|D_{\rm ff}(\kappa=+1)|^2 = \left|\lim_{r\to0}\frac{f_{\rm f}f'_{\rm f}}{r^{2\gamma-2}}\right|, \tag{7.8}$$
$$|D_{\rm ff}(\kappa=-1)|^2 = \left|\lim_{r\to0}\frac{g_{\rm f}g'_{\rm f}}{r^{2\gamma-2}}\right|, \tag{7.9}$$
$$|D_{\rm bf}|^2 = \left|\lim_{r\to0}\frac{g_{\rm f}g'_{\rm b}}{r^{2\gamma-2}}\right|, \tag{7.10}$$
$$|D_e|^2 = \left|\lim_{r\to0}\frac{g''_{\rm b}g'_{\rm f}}{r^{2\gamma-2}}\right|, \tag{7.11}$$

where $\gamma = \sqrt{\kappa^2 - (\alpha Z_0)^2}$ for positrons. One can see that the formulas for matrix elements $|D_{\rm bf}|^2$ and $|D_e|^2$ are similar, however, different wave functions are included in them. Subindexes f and b refer to free or bound cases of created electron (f' and g'), positron (f and g), as well as incoming bound electron (f'' and g'') for the case of electron conversion. Using the equations for the bound (for $1s_{1/2}$ state) and free wave functions (A.3), one can receive the final equation for $|D_{\rm bf}|^2$:

$$|D_{\rm bf}|^2 = \left| 2\sqrt{E+1}\frac{(2p)^\gamma e^{-\pi B/2}|\Gamma(a+1)|}{2\sqrt{\pi p}\Gamma(b)}(2\alpha Z)^{\gamma+1/2}\sqrt{\frac{1+\gamma}{2\Gamma(2\gamma+1)}}\cos(\eta)\right|^2, \tag{7.12}$$

where all abbreviations are similar with the $L \neq 0$ case. Here, $a = \gamma + iB$, $b = 2\gamma + 1$, $e^{-2i\eta} = \frac{\gamma+iB}{-\kappa+iB/E}$, $B = \frac{\alpha Z_0 E}{p}$, $p = \sqrt{E^2-1}$, where E is the positron energy in relativistic units. $\Gamma(x)$ stands for the gamma function [66].

Using, for instance, the equation for $|D_e|^2$ from [63]:

$$|D_e|^2 = \frac{1}{\pi}\left(\frac{\gamma+1}{2}\right)^2 \frac{(4\alpha Z\overline{p})^{2\gamma}e^{\pi\overline{B}}}{\overline{p}(\Gamma(2\Gamma+1))^3}\left|\Gamma(\gamma+i\overline{B})\right|^2 2\alpha Z(\omega+2\gamma), \tag{7.13}$$

where

$$\overline{E} = \gamma + \omega, \tag{7.14}$$

$$\overline{p} = \sqrt{\overline{E}^2 - 1}, \tag{7.15}$$

$$\overline{B} = \frac{\alpha Z\overline{E}}{\overline{p}}, \tag{7.16}$$

one obtains for δ_1 that it is given as the ratio of squared fermionic matrix elements,

$$\delta_1 = \frac{|D_{\rm bf}|^2}{|D_e|^2}. \tag{7.17}$$

The others δ-coefficients can be calculated using Eq. (7.12) and results from Ref. [63]. Note that the result [63]

$$|D_{\rm ff}|^2 = \frac{1}{\pi^2}\left(\frac{\gamma+1}{2}\right)^2 \frac{2(4pp')^{2\gamma}e^{\pi(B-B')}|\Gamma(\gamma+iB)|^2|\Gamma(\gamma+iB')|^2(EE'-\gamma^2)}{pp'(\Gamma(2\gamma+1))^4}, \tag{7.18}$$

due to Eq. (7.6) can be only used for the calculation of the δ_2 and δ_3 values after integration over all possible positron energies.

§ 8 Numerical results

As the pair conversion process is an important building block of processes investigated in the further Chapters, it is important to analyze the dependence of the pair conversion coefficient on different system parameters. Therefore, the current Section provides numerical results for the internal pair conversion process. The calculation of the bound-free pair-conversion coefficients $\beta_{\rm bf}$ for different multipolarities of nuclear transitions on an example of ^{208}Pb leads to

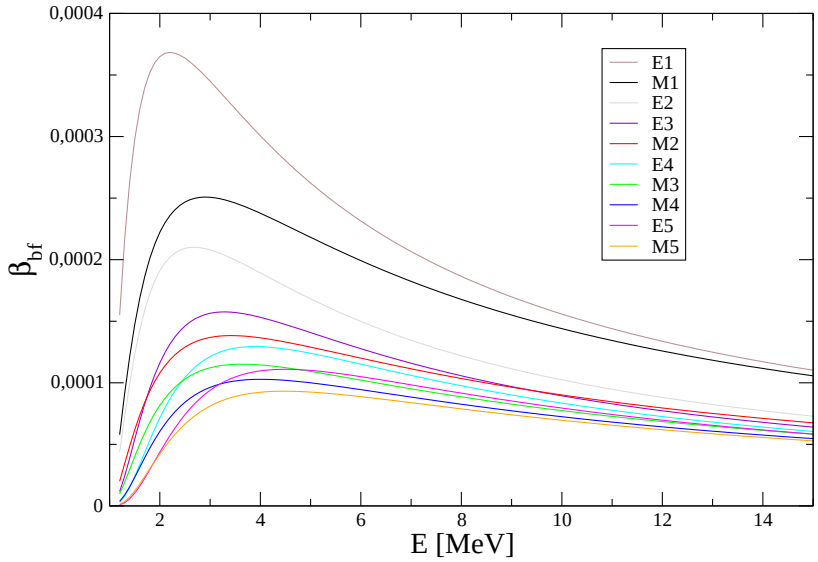

Figure 8.1 – The bound-free pair conversion coefficient, calculated for nuclear transitions with different multipolarities in $^{208}_{82}$Pb.

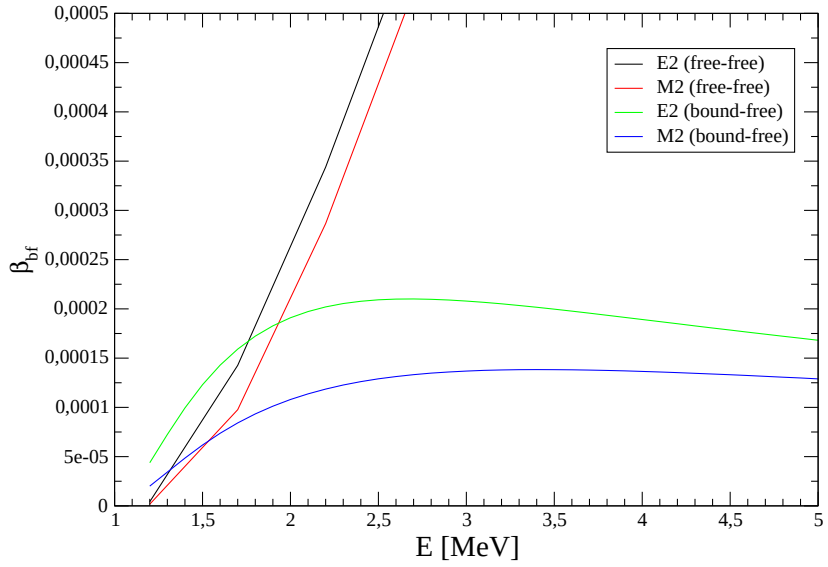

Figure 8.2 – The comparison of the transition energy dependence of the bound-free and free-free pair conversion coefficients, calculated for E2 and M2 transitions in $^{208}_{82}$Pb.

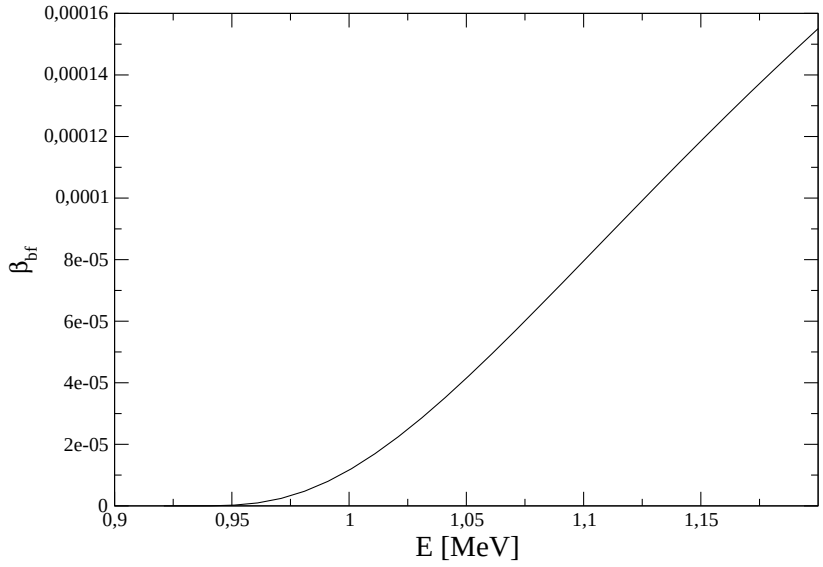

Figure 8.3 – The bound-free pair conversion coefficient as a function of the transition energy E for E1 nuclear transitions, calculated at energies about $2mc^2 \approx 1.022\,\mathrm{MeV}$ in $^{208}_{82}\mathrm{Pb}$.

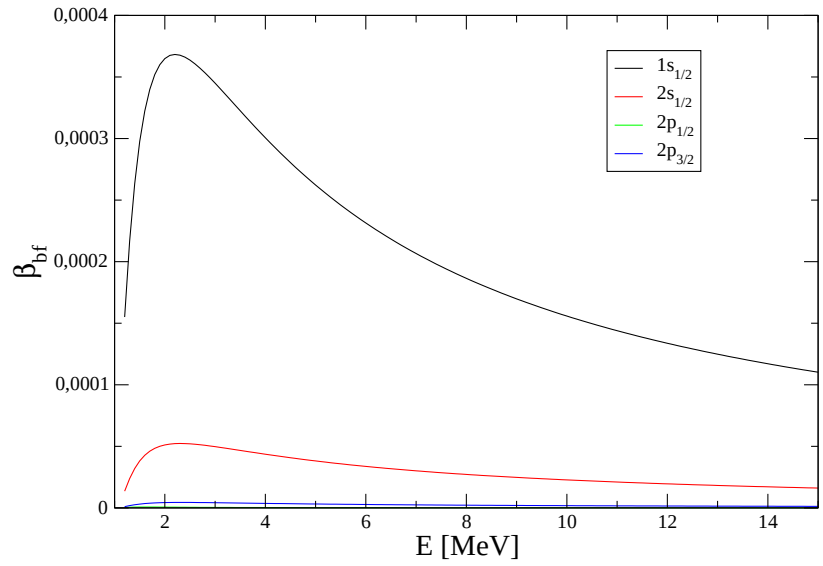

Figure 8.4 – The bound-free pair conversion coefficient, calculated for different atomic shells and E1 nuclear transition in $^{208}_{82}\mathrm{Pb}$.

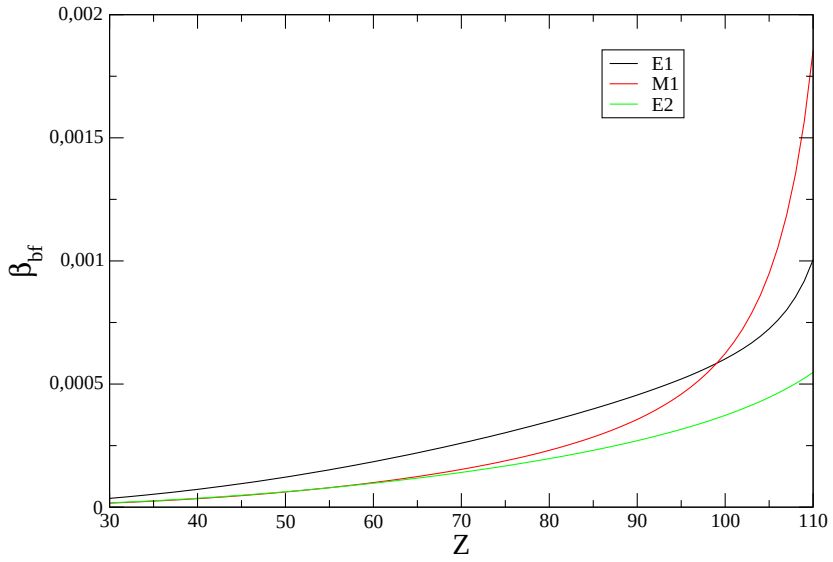

Figure 8.5 – The dependence of the bound-free pair conversion coefficient at the main peak on the nuclear charge Z for E1, E2 and M1 nuclear transitions.

dependencies shown in Fig. 8.1. One can see in this figure that that β_{bf} exhibits a maximum at transition (virtual photon) energies about 2 MeV for all transition multipolarities. This behavior is analogous to the energy dependence of the bound-free pair creation cross section in heavy ion collisions [71]. Also the figure shows that the pair conversion coefficient is on the same order of magnitude for all transition multipolarities.

For heavy ions the situation appears when the free-free effect is weaker than the bound-free effect in the vicinity of the maximum of the latter (see Fig. 8.2). Furthermore, even at energies below the usual pair-creation threshold of $2mc^2$ one can observe the bound-free process in certain cases (Fig. 8.3). This region is energetically forbidden for the creation of free electrons, which makes it interesting for experimental investigations of the bound-free process.

Fig. 8.4 illustrates that in the bound-free case in most situations it is sufficient to consider conversion into the $1s_{1/2}$ atomic shell only, as it provides the largest contribution. One can also observe that the lower binding energies of the higher electronic shells shift the peak maxima to lower transition energies. The dependence of β at the main peak on the nuclear charge can be found in Fig. 8.5. One can see here that β fastly grows with the increase of the nuclear charge, making the case of heavy ions more prominent for experimental investigations.

Using the numerical solution of the Dirac equation one can analyze the difference between calculations of the bound-free coefficient in zero- and finite-nuclear-radius assumptions. The numerical solution used in the present work employs fermionic wave functions calculated with a spherical nucleus model with the radius of $R = 1.2\,A^{1/3}$ fm, where A is the total number of nucleons. The shift caused by the finite-nuclear-radius assumption (Fig. 8.6) appears to be small at present level of theoretical accuracy and can be, therefore, neglected in comparison with the contribution of other atomic levels for a bound electron presented in Fig. 8.4.

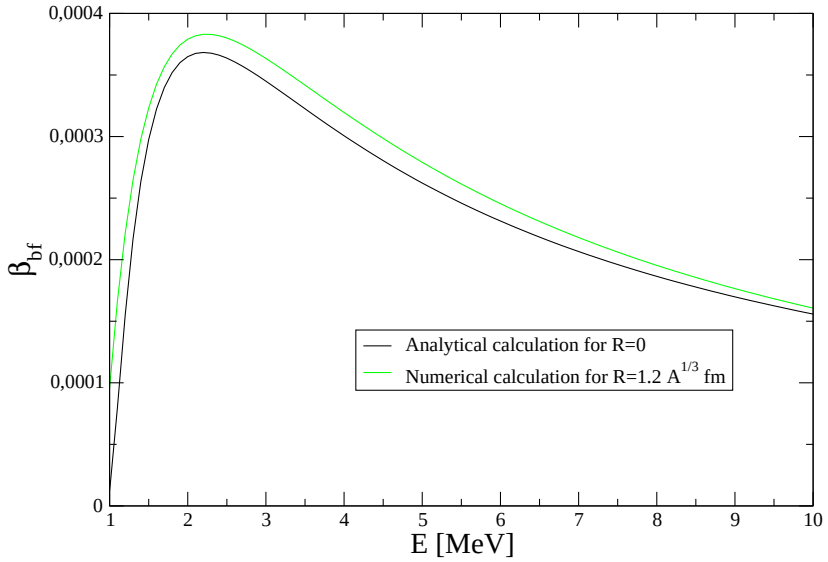

Figure 8.6 – The comparison of zero and finite nuclear radius calculations for the Bound-Free Pair Conversion Coefficient β_{bf} for E1 nuclear transitions in $^{208}_{82}$Pb.

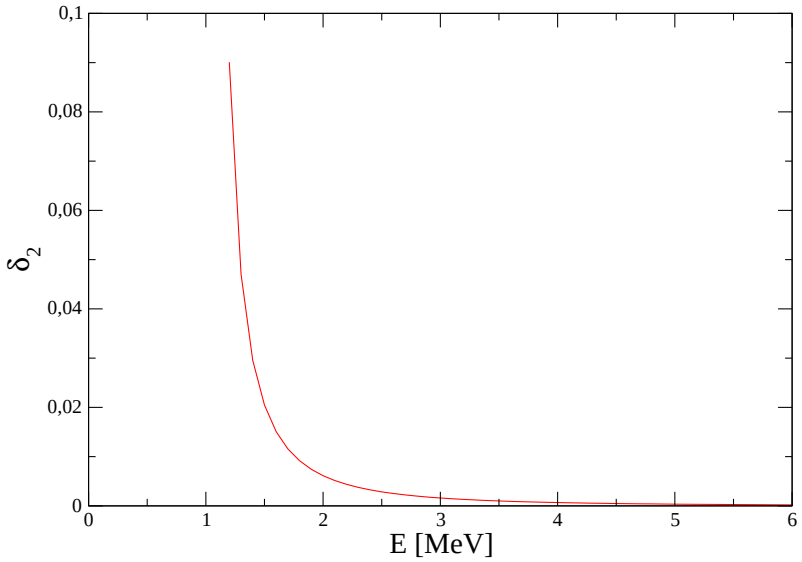

Figure 8.7 – The δ_2-coefficient (see text for notations) for E0 nuclear transitions in $^{40}_{20}$Ca as a function of the transition energy E.

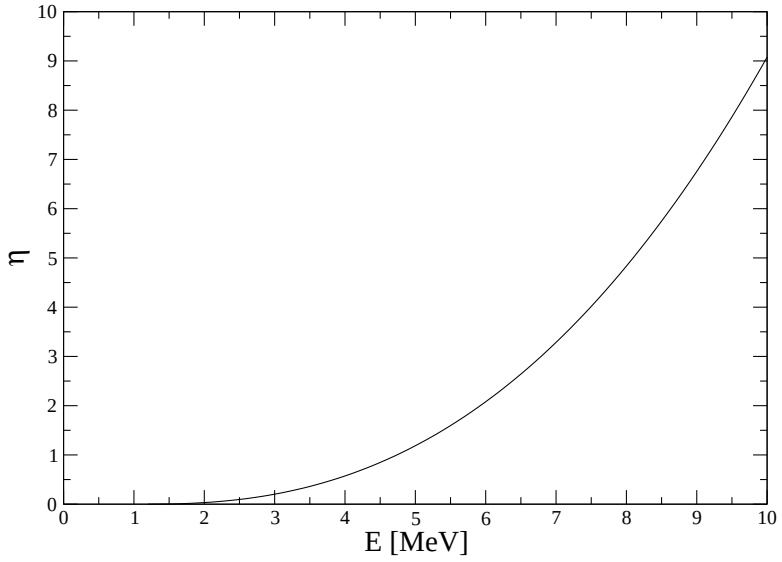

Figure 8.8 – The η-coefficient (see text for notation) for E0 nuclear transitions in $^{214}_{84}$Po as a function of the transition energy E.

In Figs. 8.7, 8.8, 8.9 and 8.10 the results for the coefficients η, δ_1, δ_2 and δ_3 are presented in the case of E0 transitions in Ca and Po. Here, firstly, one can see that the contribution of the bound-free process for heavy Po is more significant than for the light element Ca. In Po, our bound-free pair conversion process can be as much as 3 orders of magnitude stronger than the free-free one. Secondly, the main bound-free contribution interval is situated at low energies for both cases.

Summarizing the numerical results of this Section, one can come to a conclusion that the contribution of the investigated bound-free process is most significant:
(i) for high nuclear charges;
(ii) at transition energies about $2mc^2$, i.e. below or just above the free-free pair production threshold;
(iii) around the peaks for EL and ML nuclear transitions with $L > 0$;
(iv) at low energies for E0 transitions.

Having understood these features, the last task in the investigation of internal pair conversion is to present nuclei and transitions which fulfill the mentioned conditions. These cases are provided in the following Section.

§ 9 Suitable nuclear transitions

E0 case

The free-free pair conversion has been investigated experimentally in Refs. [72] and [73] on nuclear E0 transitions in different elements. In these experiments, the excited 0^+ states have

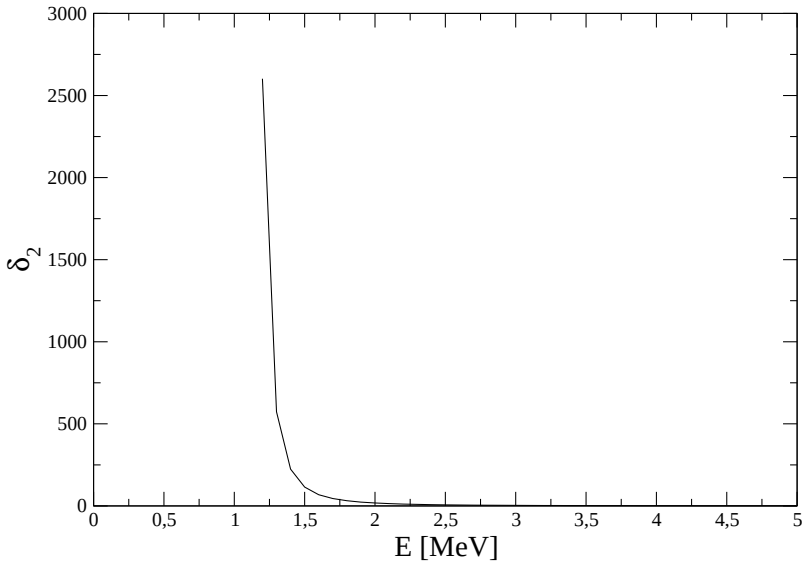

Figure 8.9 – The δ_2-coefficient (see text for definition) for E0 nuclear transitions in $^{214}_{84}$Po as a function of the transition energy E.

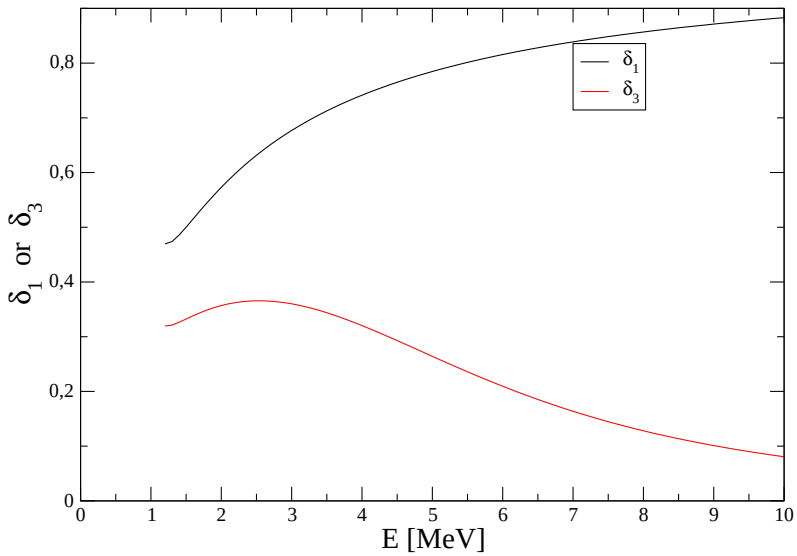

Figure 8.10 – The δ_1 and δ_3 -coefficients (see text for definition) for E0 nuclear transitions in $^{214}_{84}$Po as a function of the transition energy E.

been populated in the (p, p') reaction [72] or by β-decay [73]. In the E0 transitions $0^+ \to 0^+$, the internal conversion and the free-free pair conversion have been studied, and their probability ratio has been measured. The comparison of the theoretical value of the η-coefficient with these and other experiment data for E0 is introduced in [63] for different transitions in several elements. We provide the calculation of the δ ratios of bound-free and free-free processes for the same transitions. It appeares that the best transition for the experimental investigation of the bound-free process is the $0^+ \to 0^+$ transition in $^{214}_{84}$Po with an energy of 1.416 MeV. The lifetime of the excited state is 99 ps. The coefficients for this transitions are evaluated to be $\eta = 0.0026$, $\delta_1 = 0.49$, $\delta_2 = 212.7$ and $\delta_3 = 0.33$. Such significant ratios, especially the outstanding δ_2-value, open the possibility for an experimental investigation of the bound-free pair conversion.

Table 9.1 – The comparison of $\beta_{\rm ff}$ (experimental and theoretical values [74]) and calculated value of $\beta_{\rm bf}$ for E1 and M1 nuclear transitions in Pb.

Nucleus	Transition multipolarity	Level scheme	ω (keV)	$\beta_{\rm ff} \cdot 10^4$ experiment	$\beta_{\rm ff} \cdot 10^4$ theory	$\beta_{\rm bf} \cdot 10^4$ theory
$^{206}_{82}$Pb	E1	$5^- \to 4^+$	1719	3.26	3.4	3.3
$^{207}_{82}$Pb	M1	$7/2^- \to 5/2^-$	1770	2.73	3.1	2.1

Table 9.2 – Suitable transitions with $\omega < 2mc^2$. Data are taken from the Nuclear Database [75].

Nucleus	Transition multipolarity	Level scheme	ω (keV)	$\beta_{\rm bf} \cdot 10^5$
$^{202}_{82}$Pb	E2	$2^+ \to 0^+$	960.7	0.010
$^{205}_{82}$Pb	E2	$9/2^- \to 5/2^-$	987.5	0.091
$^{207}_{83}$Bi	E2	$13/2^- \to 9/2^-$	931.8	$1.5 \cdot 10^{-5}$
$^{208}_{83}$Bi	E3	$10^- \to 7^+$	921.0	$2.34 \cdot 10^{-14}$
$^{213}_{88}$Ra	E2	$9/2^- \to 5/2^-$	1062.5	1.46

E1 and M1 transitions

One can also consider other suitable cases with non-zero multipolarity, $L > 0$. In Ref. [74] free-free pair conversion in nuclear E1 and M1 transitions in Pb (lead) have been experimentally investigated. The initial states of ^{206,207}Pb nuclei have been populated by electron capture decay of ^{206,207}Bi, respectively. The 5^- level of ^{206}Pb at 3403 keV has been populated with a 90% probability, the $7/2^-$ state (2339 keV) of ^{207}Pb with a probability of 7%. The 5^- state decays by an E1 transition to 4^+, the $7/2^-$ level by a M1 transition to $5/2^-$. Having the energies in the region of the maximum of $\beta_{\rm bf}$, these two transitions (see Tab. 9.1) can be also suggested for experimental studies of bound-free pair conversion.

Low energies

For the interesting case of nuclear energies less than $2mc^2$, when the free-free pair conversion channel is closed, one can also introduce suitable bound-free transitions. This is due to the fact that the electron created is bound, i.e. for its production less energy is needed than for the production of a free particle. Examples are given in Tab. 9.2. For transitions with $\omega < 2mc^2$, the free-free process is forbidden, therefore, the bound-free process may be investigated without the disturbing background of free-free pair conversion.

One may consider different mechanisms for the population of initial states to observe the bound-free pair conversion effect. For the 0^+ excited state in ^{214}Po this may be the beta decay of ^{214}Bi [73, 76]. For the 5^- state in ^{206}Pb it is the electron capture decay of ^{206}Bi or more than 10 other possible production channels [77]. The same is valid for the $7/2^-$ state in ^{207}Pb [78]. Initial states for transitions, presented in Tab. 9.2, can be also populated in different reactions (1 to 10 reactions for each element) [78–82].

The estimation of the probability of the total process for a certain case is briefly concluding this Section. For example, the 2^+ level in ^{202}Pb (see Tab. 2) has a lifetime about $\tau \approx 0.1$ ns. Since the E2 transition $2^+ \to 0^+$ is the only way for this state to decay, the γ-emission probability in this case is $P_\gamma = 1/\tau \approx 10^8$ s^{-1}. The bound-free pair conversion coefficient is found to be $\beta_{\rm bf} \approx 2 \cdot 10^{-6}$, thus the total bound-free process probability in this decay is $P^{tot}_{\rm bf} \approx 200 s^{-1}$. The same procedure for the $10^- \to 7^+$ E3 transition in ^{208}Bi gives us $P^{tot}_{\rm bf} \approx 0.3$ s^{-1}. The quantities $P^{tot}_{\rm bf} = \beta_{\rm bf} P_\gamma$ present the order of magnitude of typical rates of internal pair conversion.

The theory and numerical calculations of this Chapter are provided in an assumption that the final state of the system is not split due to the electron-nucleus coupling, i.e. the hyperfine splitting is negligible. However, this is completely true only for the 0-spin nuclear states (0^+). For other cases one has to consider the transitions between hyperfine levels of the total system. However, in the absence of a sufficiently high resolution to see the influence of this splitting in an experiment, these hyperfine sublevel contributions will sum up into one contribution of an unresolved state. Our results for the transition rates assuming a spinless nucleus are equivalent to this unresolved-state contribution. Therefore, in this Chapter we do not consider hyperfine splitting even in the case of the $9/2^-$ final state in ^{207}Bi, i.e., the nuclear state with the highest spin.

§ 10 Discussion

In this Chapter analytical and numerical results for the bound-free pair creation process have been received. Numerical calculations have been provided for different EL and ML nuclear transitions with the transition momentum $L > 0$, as well as for E0 nuclear transitions. At some transition energies for heavy ions it appeared that this coefficient is greater than or comparable to that of the free-free case. The results for E0 transitions are rather interesting since these transitions are radiationless, and the bound-free, free-free and internal conversion channels constitute the only possible electromagnetic decay processes. These findings are relevant for possible future experimental investigations.

It has been also shown that nuclear transitions corresponding to the cases when the bound-free and free-free processes are comparable in strength can be found for several elements and

can be experimentally investigated. All these results may be relevant for the later Chapters and for applications in atomic physics and astrophysics, as discussed later.

The free-free and bound-free pair conversion processes can take place when the energy of the corresponding nuclear transition is above some certain energy threshold. Another atomic system which has sufficient energy to deexcite by pair conversion is a muonic atom. A muon having an approximately 200 times larger mass than an electron is able to produce a pair of electron and positron within its transition between two bound atomic states. Therefore, the investigation of pair production with both bound and free electron creation is of interest for studies of muonic cascades. The study of this deexcitation mechanism is considered in the next Chapter.

Chapter II

Pair creation in muonic atoms

§ 11 Introduction to pair creation in muonic atoms

The pair conversion process in a more exotic system, namely, in muonic atoms, is considered in the present Chapter. The muonic atom is a system consisting of a nucleus, bound electrons, and at least one muon in a bound atomic state. The moun decays via weak interaction, therefore, the muonic atom has a short overall lifetime. The investigation of muonic atoms is of importance for several applications. For instance, muonic hydrogen has been used in precise laser spectroscopic experiments for measuring the proton radius [30]. Interestingly, it was found that the proton radius determined by this method is smaller than the previously established value.

Usually, muonic atoms are created with a muon captured into a highly excited state, causing cascade transitions of the muon to the lowest-lying state [31]. A muon having an approximately 200 times larger mass than an electron can produce an electron-positron pair within its transition between some low-lying bound atomic states [see Fig. 11.1]. Therefore, the investigation of the pair production with both a bound or a free electron is crucial for the studies of muonic cascades.

Grotch and Kazes [83] theoretically investigated the free-free pair production process for $2s \rightarrow 1s$ transitions in muonic atoms. They derived pair creation rates in the non-relativistic approximation in the and high-Z regime. These results are improved in the present thesis, the case of the bound-free process is also considered in this Chapter.

The bound-free and free-free electron-positron pair creation accompanying muonic transitions between atomic levels are rather similar processes to internal pair conversion accompanying nuclear decay, described in the previous Chapter. From the technical point of view the main difference is that single-muon wave functions are much easier to handle than the many-body states of nuclei, therefore, the non-penetration approximation does not have to be applied in the case of muonic atoms. However, one has to take into account quantum electrodynamic (QED) corrections to muonic wave functions, since muons have large intersection with the atomic nucleus, i.e. with the region where the strongest electric fields prevail. As in the previous Chapter, some theoretical derivations from Soff, Schlüter and Greiner. [62, 63] are used in order to provide a precise.

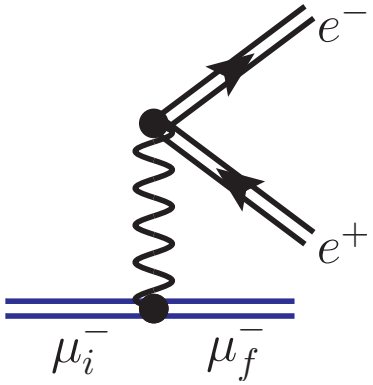

Figure 11.1 – The leading Feynman diagram of pair creation in a bound-bound muonic transition. Here, again, double black lines denote an electron or a positron in the nuclear Coulomb field, while the double blue lines stand for bound states of a negative muon. The electron created may be bound or unbound.

§ 12 Pair creation coefficient for muonic atoms

To characterize the pair creation process in monic atoms one can introduce the same quantity as in the case of the nuclear pair conversion, namely, the ratio of the probability of a certain type of pair creation to the photon emission probability in the same muonic transition:

$$\beta^{\mu}_{\mathrm{ff}} = P^{\mu}_{e^-_{\mathrm{f}}e^+_{\mathrm{f}}}/P^{\mu}_{\gamma}, \tag{12.1}$$

$$\beta^{\mu}_{\mathrm{bf}} = P^{\mu}_{e^-_{\mathrm{b}}e^+_{\mathrm{f}}}/P^{\mu}_{\gamma}. \tag{12.2}$$

These quantities are called pair creation coefficients. The required probabilities can be derived in a way similar to the derivation of the previous Chapter, with the only difference being in the use of the non-penetration approximation. One does not need to make this assumption for the muonic case, since the theory here does not operate with nuclear structure. Therefore, in equation in equation (6.14) for the matrix element U_m and in the corresponding equations for U_e and U_0 one can keep all the terms and evaluate them in analogy to the calculation of matrix elements of photon exchange between two electrons. This can be done because muons are also Dirac fermions. Using the results of Ref. [84], one may write all integrals of Bessel functions in a clear way:

$$\begin{aligned} U^e(L,M) &= J(L,M)(-1)^L C_L(\mu,+)C_L(e,+) \\ &\times \left[\frac{L+1}{2L+3}\int_0^\infty dx\int_0^\infty dy(2L+3)i\omega j_{L+1}(\omega x_<)h_{L+1}(\omega x_>)Q_\mu(x)Q_e(y)\right. \\ &\left. +\frac{L}{2L-1}\int_0^\infty dx\int_0^\infty dy(2L-1)i\omega j_{L-1}(\omega x_<)h_{L-1}(\omega x_>)P_\mu(x)P_e(y)\right], \end{aligned} \tag{12.3}$$

$$\begin{aligned} U^m(L,M) &= J(L,M)(-1)^{L+1}C_L(\mu,-)C_L(e,-)\frac{(\kappa_\mu+\kappa'_\mu)(\kappa+\kappa')}{L(L+1)} \\ &\times \frac{L+1}{2L+3}\int_0^\infty dx\int_0^\infty dy(2L+1)i\omega j_L(\omega x_<)h_L(\omega x_>)V_\mu(x)V_e(y), \end{aligned} \tag{12.4}$$

where the angular coefficients are given with $3j$-symbols as

$$J(L,M) = \sum_{\nu,\nu'}(-1)^{J_i+j+L-\nu-\mu-M}\begin{pmatrix} J_i & L & J_f \\ -\nu & M & \nu' \end{pmatrix}\begin{pmatrix} j & L & j' \\ -\mu & M & \mu' \end{pmatrix}, \tag{12.5}$$

$$C_L(\mu,c) = (-1)^{J_f+1/2}\sqrt{(2J_i+1)(2J_f+1)}\begin{pmatrix} J_i & L & J_f \\ 1/2 & 0 & -1/2 \end{pmatrix}\Pi(l_i,l_f,L,c), \tag{12.6}$$

$$C_L(e,c) = (-1)^{j'+1/2}\sqrt{(2j'+1)(2j+1)}\begin{pmatrix} j & L & j' \\ 1/2 & 0 & -1/2 \end{pmatrix}\Pi(l,l',L,c), \tag{12.7}$$

and the parity relations are

$$\Pi(l_1,l_2,l_3,c) = \begin{cases} 1, & \text{if} \quad l_1+l_2+l_3 \quad \text{is} \quad \text{even} \quad \text{and} \quad c=+; \\ 1, & \text{if} \quad l_1+l_2+l_3 \quad \text{is} \quad \text{odd} \quad \text{and} \quad c=-; \\ 0, & \text{if} \quad l_1+l_2+l_3 \quad \text{is} \quad \text{even} \quad \text{and} \quad c=-; \\ 0, & \text{if} \quad l_1+l_2+l_3 \quad \text{is} \quad \text{odd} \quad \text{and} \quad c=+. \end{cases} \tag{12.8}$$

J_i and J_f are the angular momenta of initial and final muonic states and j and j' are angular momenta of electron and positron states, respectively. Dirac quantum numbers are κ, κ' for the light fermions and κ_μ, κ'_μ for initial and final muonic states. Furthermore, the following radial functions have been introduced:

$$P_\mu(r) = U_\mu(r) + \frac{\kappa_\mu - \kappa'_\mu}{L}V_\mu(r), \tag{12.9}$$

$$P_e(r) = U_e(r) + \frac{\kappa - \kappa'}{L}V_e(r), \tag{12.10}$$

$$Q_\mu(r) = -U_\mu(r) + \frac{\kappa_\mu - \kappa'_\mu}{L+1}V_\mu(r), \tag{12.11}$$

$$Q_e(r) = -U_e(r) + \frac{\kappa - \kappa'}{L+1}V_e(r), \tag{12.12}$$

$$U_\mu = g^\mu_{\kappa'_\mu}f^\mu_{\kappa_\mu} - g^\mu_{\kappa_\mu}f^\mu_{\kappa'_\mu}, \tag{12.13}$$

$$U_e = g_{\kappa'}f_\kappa - g_\kappa f_{\kappa'}, \tag{12.14}$$

$$V_\mu = g^\mu_{\kappa'_\mu}f^\mu_{\kappa_\mu} + g^\mu_{\kappa_\mu}f^\mu_{\kappa'_\mu}, \tag{12.15}$$

$$V_e = g_{\kappa'}f_\kappa + g_\kappa f_{\kappa'}, \tag{12.16}$$

where the f and g are the radial components of the corresponding Dirac wave functions.

These matrix elements enter the calculation of the pair creation probabilities $P_{e^-_b e^+_f}$ and $P_{e^-_f e^+_f}$. For the calculation of the rates β_{bf} and β_{ff} one also has to derive the probability of gamma emission,

$$P_\gamma = \frac{8\pi\alpha\omega}{2J_i+1}\sum_{\nu\nu'}\sum_{LM}|V_\gamma|^2, \tag{12.17}$$

where the photon emission by the muonic transition current $\vec{j}^\mu$ is characterized by the matrix element

$$V_\gamma = \int d\vec{r}_\mu \vec{j}_\mu(\vec{r}_\mu)A_L^{M(\tau)*}(\omega\vec{r}_\mu). \tag{12.18}$$

Note that in these formulas the subscript μ labels quantities associated with the muon, and it is not a 4-vector index. Substituting into this expression the Bessel functions (see Eq. (6.7)), for the photon emission one has:

$$V_\gamma = \int_0^\infty dr r^2 j_L(\omega r)(\kappa_\mu + \kappa'_\mu)\langle \mu ML\rangle \left(g^\mu_{\kappa_\mu} f^\mu_{\kappa'_\mu} + f^\mu_{\kappa_\mu} g^\mu_{\kappa'_\mu} \right), \tag{12.19}$$

where we introduce the notation

$$\begin{aligned} \langle \mu ML\rangle &= \sum_{\nu,\nu'} (-1)^{2J_f - \nu' + 1/2} \sqrt{\frac{(2J_i+1)(2J_f+1)(2L+1)}{4\pi}} \\ &\times \begin{pmatrix} J_i & J_f & L \\ \nu & -\nu' & M \end{pmatrix} \begin{pmatrix} J_i & J_f & L \\ -1/2 & 1/2 & 0 \end{pmatrix}. \end{aligned} \tag{12.20}$$

All integrals can be numerically evaluated with a certain form of the Dirac wave functions.

§ 13 A comment concerning free-free pair creation

In the case of free-free pair production, the electron and positron wave functions posses high-frequent fluctuations at distances far from the mounic core, causing some problems in the integration of the matrix elements. Therefore, an additional cut-off procedure has to be applied. Here, this method is introduced for the case of a neutral atom assumption. The radial integral can be split into two parts:

$$\begin{aligned} &\int_0^\infty dx \int_0^\infty dy\, j_L(\omega x_<) h_L(\omega x_>) V_\mu(x) V_e(y) = \\ &= \int_0^\infty dx \int_0^r dy\, j_L(\omega x_<) h_L(\omega x_>) V_\mu(x) V_e(y) + \int_0^\infty dx\, j_L(\omega x) V_\mu(x) \int_r^\infty dy h_L(\omega y) V_e(y). \end{aligned} \tag{13.1}$$

This has to be evaluated for r larger than the characteristic size of the muonic wave function. The first part of the integral can be calculated without any problems. However, some difficulties appear in the evaluation of the electronic integral in the second term. The case of the neutral atom requires free wave functions, therefore, one can rewrite this integral as

$$\begin{aligned} \int_r^\infty dx h_L(\omega x) V_e(x) &= \int_r^\infty dx h_L(\omega x) \left[\sqrt{\frac{p'(E'+1)}{\pi}} \sqrt{\frac{p(E-1)}{\pi}} \frac{\kappa}{|\kappa|} j_{l'}(p'x) j_{\bar{l}}(px) \right. \\ &+ \left. \sqrt{\frac{p'(E'-1)}{\pi}} \sqrt{\frac{p(E+1)}{\pi}} \frac{\kappa'}{|\kappa'|} j_l(px) j_{\bar{l}'}(p'x) \right], \end{aligned} \tag{13.2}$$

where $l = |\kappa + 1/2| - 1/2$ and $\bar{l} = |\kappa - 1/2| - 1/2$. To calculate this, one has to evaluate integrals of the type

$$\int_r^\infty dx h_L(\omega x) j_{l_1}(\lambda x) j_{l_2}(\nu x), \tag{13.3}$$

which can be provided in the large-r approximation by means of trigonometric functions [66].

§ 14 Numerical results

Bound-free case

All calculations within this Chapter have been evaluated with the help of numerical Dirac wave functions provided by numerical procedures described in [70]. These wave functions are evaluated for the muonic case in the assumption of a finite nuclear size effects and for the case of the electron and positron in the point-nucleus approximation. In the muonic potential an additional term has been used, representing the vacuum polarization correction by means of the Uehling potential. This is the dominant quantum electrodynamic contribution in muonic atoms [39]. However, this QED effect together with finite nuclear effects appeared to yield minor corrections to the pair creation coefficients obtained. This work presents results of numerical calculations of the bound-free pair production process in different muonic transitions in different ions having initially only one muon and no electrons. In these calculations the created electron is assumed to be produced in the $1s$ atomic state.

The left subfigures in Fig. 14.1 present the bound-free pair production coefficient for 2 different muonic transitions in different bare muonic ions which, for simplicity, do not contain bound electrons initially. The right subfigure of Fig. 14.1 displays the energies of the muonic transitions. In the case of the $3p \to 2s$ muonic transition, the pair production coefficient possesses a maximum at the nuclear charge $Z = 75$, with the muonic transition energy being $E = 2.5$ MeV. This approximately corresponds to the maximum of the pair conversion coefficient in the case of nuclear pair conversion presented in the previous Chapter.

Free-free case

In the free-free case, numerical procedures of Ref. [70] have been used to calculate the relativistic muonic wave functions in the field of the finite-size nucleus, again with the implementation of the Uehling potential in order to include the vacuum polarization effect. The wave functions of free fermions have been calculated separately in regions near and far from the muonic core, according to the comment above [see Eqs. (13.1–13.3)]. The first integral in Eq. (13.1) has been evaluated with numerically constructed functions, the second one with analytical free-particle Dirac wave functions [85, 86] in spherical coordinates.

The results of these numerical investigations of the free-free pair production are presented in Fig. 14.2. There one can find again the pair production coefficient in dependence on the nuclear charge Z for different muonic transitions, together with the corresponding transition energies. One can see on Fig. 14.2 that the behavior of the free-free pair production coefficient is very similar to that of nuclear pair conversion. The same can be noticed about the order of magnitude of the received values of the pair creation coefficients.

Further results

As already mentioned, the above results have been obtained in the assumption that the created electron occupies the $1s$ atomic state. However, it is also interesting to see the contributions of another electronic states. Tab. 14.1 contains these contributions up to the electron principal

$3p \rightarrow 2s$ transition:

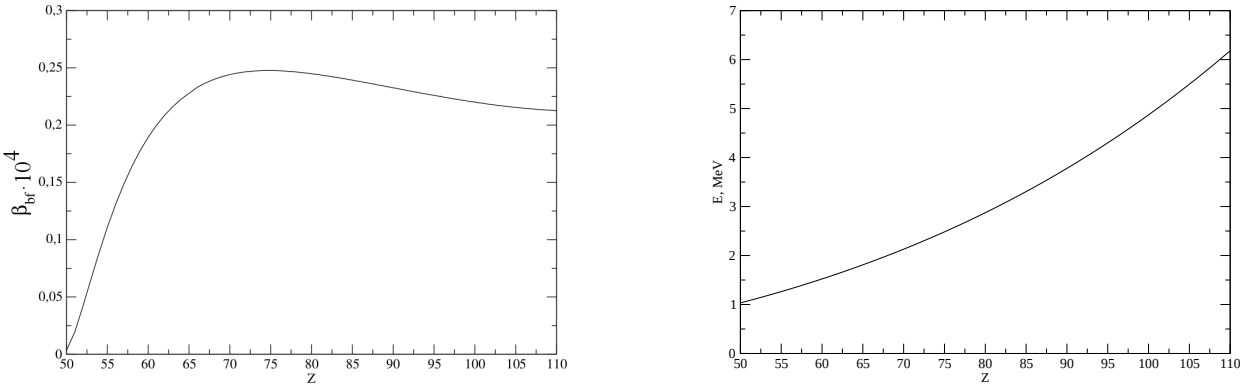

$5p \rightarrow 3s$ transition:

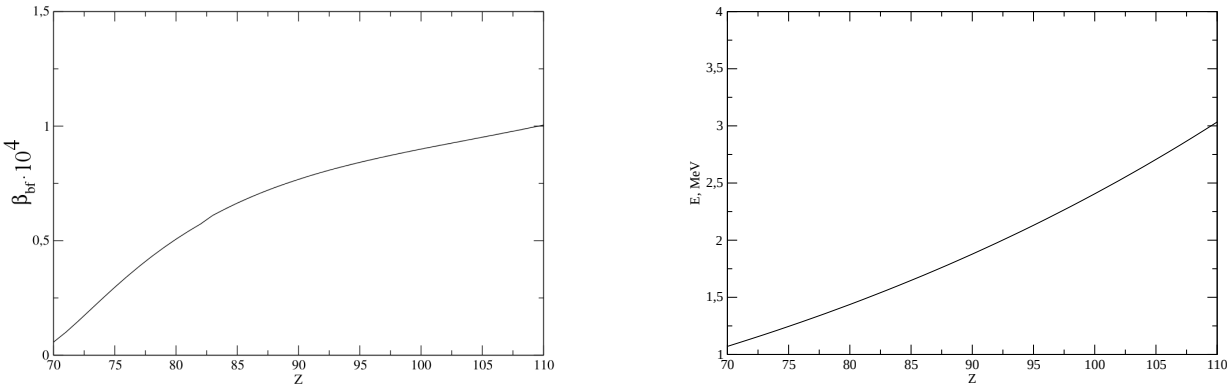

Figure 14.1 – (**left**) Bound-free pair creation coefficients for 2 different muonic transitions in different bare muonic atoms and (**right**) the corresponding energies of the muonic transition. The total nucleon number is $A = 2.5\,Z$.

quantum number $n = 4$. This table shows that the $1s$ final states indeed possesses the the largest creation rates, however, higher s-states still have significant contributions.

The last issue to be discussed in this Section is the charge state of the atom. The muonic atom is usually created by muon capture into some high-lying atomic level. It is followed by a muon cascade, causing multiple electron emissions from the atom. Therefore, by the time when the muon reaches the state suitable for pair production, the atom is not neutral any more. However, there are still some bound electrons in it (for details, see [87]). Their amount depends on the certain experimental situation, and it certanly influences our pair creation rates. Fig. 14.3 shows the dependence of the pair production coefficient on the number of the rest electrons in the atom. This curve is obtained in an assumption of an effective nuclear charge which is "felt" by the created electron and positron. One can see that this dependence possesses a significant increase of the total rate with the increase of the number of the rest electrons, i.e. the more neutral the atom is, the higher the pair creation rate.

$2p \rightarrow 1s$ transition:

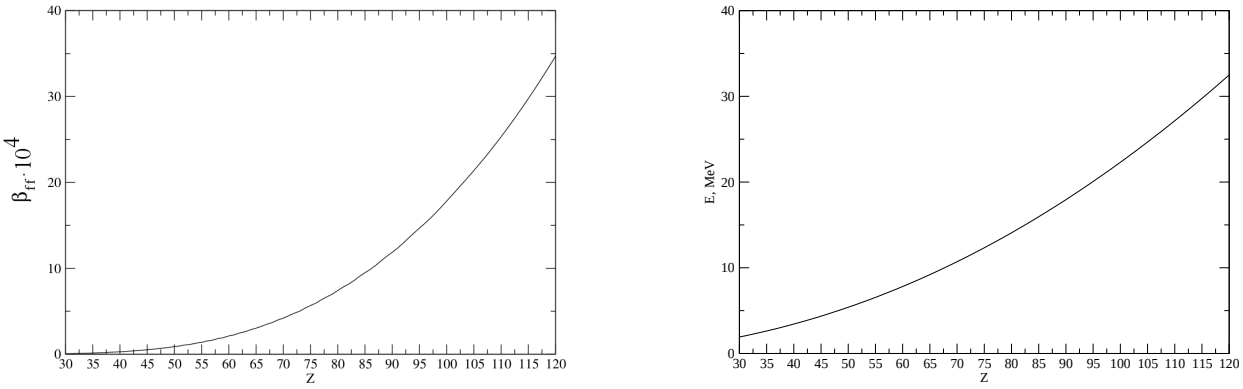

$3p \rightarrow 2s$ transition:

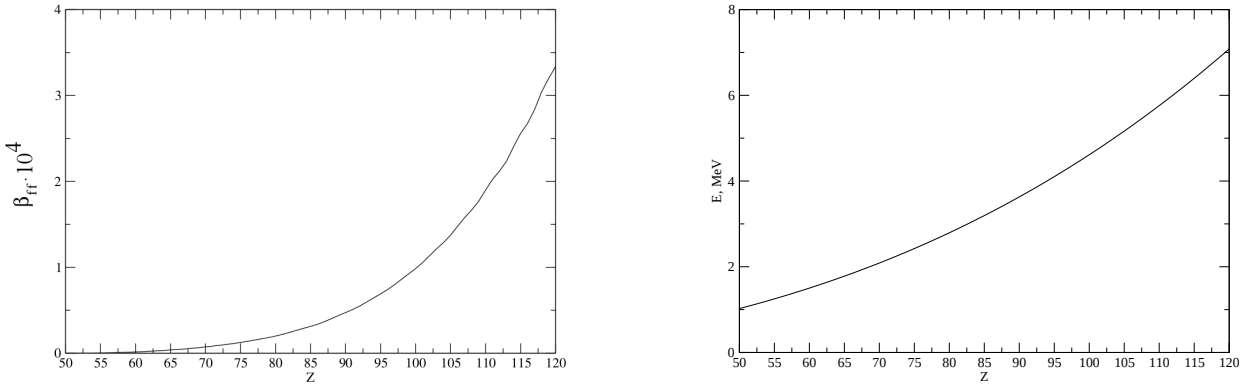

$5p \rightarrow 3s$ transition:

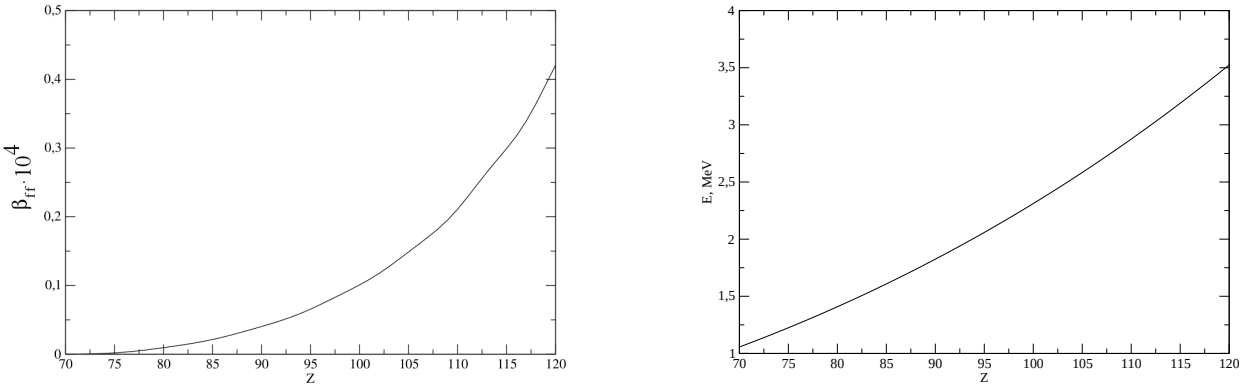

Figure 14.2 – (**left**) The free-free pair production coefficient for different muonic transitions in different bare muonic atoms and (**right**) the corresponding energies of the muonic transition. The total nucleon number is $A = 2.5\,Z$.

Table 14.1 – Bound-free partial pair production coefficients for different electron states for an E1 muonic transition ($5p_{1/2} \to 3s_{1/2}$) in $^{238}_{92}$U with the photon energy ω = 1.976 MeV. A summation over all possible positron states is performed. The total pair production coefficient for all presented electron states is $\beta = 0.10160 \cdot 10^{-3}$.

Electron state	Positron energy, MeV	$\beta_{\rm bf}$ (partial)
$1s_{1/2}$	1.594	$0.79948 \cdot 10^{-4}$
$2s_{1/2}$	1.498	$0.12396 \cdot 10^{-4}$
$2p_{1/2}$	1.498	$0.14195 \cdot 10^{-5}$
$2p_{3/2}$	1.494	$0.22033 \cdot 10^{-7}$
$3s_{1/2}$	1.479	$0.35890 \cdot 10^{-5}$
$3p_{1/2}$	1.479	$0.48730 \cdot 10^{-6}$
$3p_{3/2}$	1.478	$0.91905 \cdot 10^{-8}$
$3d_{3/2}$	1.478	$0.11756 \cdot 10^{-8}$
$3d_{5/2}$	1.478	$0.36390 \cdot 10^{-10}$
$4s_{1/2}$	1.473	$0.77666 \cdot 10^{-7}$
$4p_{1/2}$	1.473	$0.13268 \cdot 10^{-5}$
$4p_{3/2}$	1.472	$0.27341 \cdot 10^{-6}$
$4d_{3/2}$	1.472	$0.16598 \cdot 10^{-5}$
$4d_{5/2}$	1.472	$0.36877 \cdot 10^{-6}$
$4f_{5/2}$	1.472	$0.18431 \cdot 10^{-7}$
$4f_{7/2}$	1.472	$0.12314 \cdot 10^{-8}$

§ 15 Discussion

In this Chapter the results for the bound-free and free-free cases of pair production in muonic atoms are presented and compared with the results of the previous Chapter on nuclear pair conversion. It has been discussed in the previous Chapter that in some cases, mostly in heavier elements and at low deexcitation energies around 2 MeV, the bound-free process contribution appears to be larger than the free-free one. From Figs. 14.1 and 14.2 one can see that a similar situation is repeated in the case of muonic atoms.

It is impossible for the muonic case to select an element and a transition and vary the transition energy, as has been done in the previous Chapter. However, even here it is possible to observe some behaviors similar to the case of the nuclear pair conversion. For instance, the maximum of bound-free pair production coefficient appears at some low energy in the $3p_{1/2} \to 2s_{1/2}$ transition (Fig. 14.1).

As already mentioned, the main technical difference between problems solved here and in the previous Chapter is in the implementation of the non-penetration approximation for the calculation of the matrix elements. This assumption has been used for the case of nuclear pair conversion for simplicity, but it is not necessary here. Therefore, the the results for pair creation in muonic atoms opens a way to check the non-penetration approximation. Our numerical calculations have demonstrated that it is quite a reasonable assumption in the muonic case, and therefore, since the extent of the nucleus is even smaller than the size of muonic orbitals, it is even more applicable for the nuclear process.

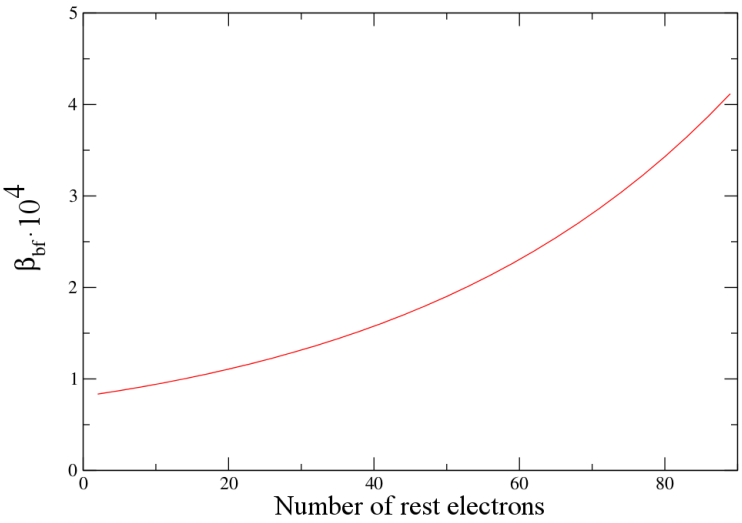

Figure 14.3 – The dependence of the pair creation coefficient β_{bf} on the number of the rest electrons in the atom (^{238}U) in the assumption that there are no electrons in the K-shell after the muonic cascade. The muon undergoes a $5p_{1/2} \rightarrow 3s_{1/2}$ transition.

At last let us discuss an application of such studies with muonic atoms. The transition decay width of the pair creation process is, in accordance with the Cutkosky rules, the imaginary part of a mixed two-loop vacuum polarization self-energy correction to the binding energy of the bound muonic state. Therefore, a measurement of pair creation rates and their comparison to theory provides an additional benchmark for the correctness of the QED theory of bound muons, which was also employed to the determination of the proton radius via muonic hydrogen spectroscopy. The mentioned two-loop correction can be tested separately. Pair creation measurements could therefore provide a contribution to the solution of the proton radius puzzle. At the higher nuclear charges where pair creation occurs, the QED terms are even larger than for hydrogen, thus such tests via pair creation measurements would be particularly sensitive to possible deviations.

Chapter III

Nuclear excitation by resonance positron annihilation

§ 16 Introduction to nuclear excitation by resonance positron annihilation

Positron collisions with atomic matter lead to a number of processes [32–36], among which annihilation with shell electrons is one of the most prominent effects. The annihilation of a free electron-positron pair leads to the emission of two gamma rays. The single gamma-ray emission is possible only in the vicinity of an atomic nucleus due to the momentum recoil of the latter [88]. This process of single gamma-ray emission was examined before [89] and is well understood. Alternatively, one can investigate the case when the same nucleus resonantly absorbs the whole energy of the annihilating particles and becomes excited. This single-step process, termed nuclear excitation by resonant positron annihilation (NERPA), is represented in Fig. 16.1(a) by the level schemes of the atomic electron shells and the nucleus. This figure demonstrates that the threshold energy ω for a possible nuclear excitation is decreased from the double electron mass by the electron binding energy $E_b^{e^-}$, i.e. $\omega = 2mc^2 - E_b^{e^-}$. The process was first introduced by Present and Chen [90].

Generally, NERPA may be followed by different nuclear deexcitation processes leading to a nuclear ground or excited state. In the important case of non-exotic nuclei, where the nuclear state excited by NERPA is situated about 1-2 MeV above the threshold energy, the main channel of the nuclear deexcitation is the radiative decay. The leading diagram of this two-step process, labeled as NERPA-γ, is illustrated in Fig. 16.1(b).

NERPA constitutes a way to excite nuclei which is alternative to other channels, such as photo- and Coulomb excitation. Photo-excitation experiments are conventionally done with bremsstrahlung, synchrotron or inverse Compton sources. X-ray free electron lasers, providing the highest photon intensities, are presently limited to the keV photon energy regime [91, 92]. The great advantage of photo-excitation is the monochromaticity of the X- or gamma-ray beam and the resonant character of the nuclear excitation. In recent theoretical studies, significant possible energy increase for photo-excitation has been predicted by the use of zepto-second laser pulses [93]. The transitions predominantly accessible this way are, however, limited by electric-dipole ($E1$) type. On the other hand, Coulomb excitation, i.e. excitation by the inelas-

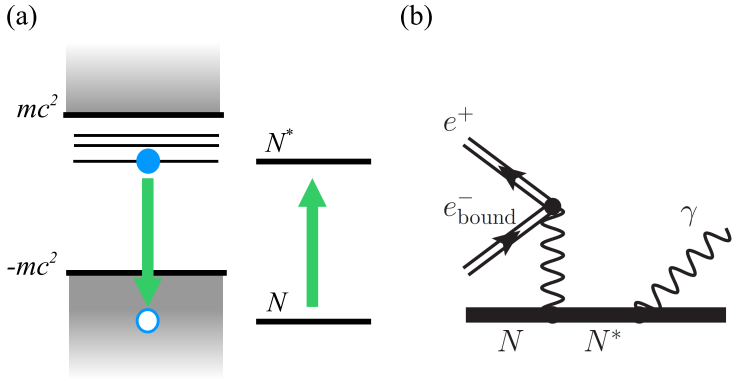

Figure 16.1 – (a) The illustration of positron annihilation via nuclear excitation by the corresponding fermionic and nuclear level schemes. mc^2 is the rest energy of the electron, and N (N^*) stands for the nuclear initial (excited) state. (b) The lowest-order Feynman diagram of the NERPA process followed by nuclear deexcitation by emission of a photon. Thick lines denote nuclear states, double lines denote fermions in the Coulomb field of the nucleus, and wave lines represent real or virtual photons.

tic scattering of massive charged particles may induce transitions of arbitrary multipolarities, although without any selectivity of the nuclear energy levels. We have shown [1] that NERPA has an attractive combination of both of these advantages: it carries a resonant character of excitation and provides a significant excitation cross section regardless of the multipolarity. Furthermore, it has been found, as discussed later, that in certain cases the NERPA cross section can be comparable to or an order of magnitude higher than that of Coulomb excitation. The present Chapter contains a complete theoretical description of NERPA, together with numerical results for a broad spectrum of elements, and the discussion of numerous practical applications of NERPA.

As it has been already mentioned, NERPA can be used for an excitation of nuclear states regardless of the multipolarity. In particular, NERPA can resonantly induce monopole transitions. A possibility to effectively excite such transitions is particularly important for studies of deformed nuclei. Another important NERPA application is the investigation of the collective nuclear excitation, the giant monopole resonance [37, 38]. This mode of nuclear excitation is termed "breathing" mode as it involves oscillation of the nuclear volume, which is the only way known for the experimental study of nuclear compressibility [94]. In the case of giant nuclear resonances of any multipolarity, NERPA appeared to be a novel method bearing all the above-mentioned advantages of Coulomb excitation.

Another direction for the applications of NERPA is the induction of nuclear excitations with high multipolarity. For instance, octupole deformations have been recently investigated, producing octupole transitions by Coulomb excitation in collisions with lighter nuclei, and monitoring the subsequent γ decay [95]. NERPA may be complementarily employed in future for such studies, relevant for benchmarking nuclear structure models. A further property of NERPA is that experiments may even be performed with neutral atoms, e.g. solid targets, without the necessity of stripping off the atomic electrons or accelerating the nuclei.

Recently, intense positron jets with MeV energies or above have been generated in laser-plasma interactions [41, 44, 96, 97], with a quasi-monoenergetic spectrum, and with positron numbers reaching 10^{10}/shot [44]. This powerful method opens a variety of potential applications in the field of positron-matter interaction. Therefore, we put forward the indirect laser excitation of nuclei via NERPA, utilizing positrons produced by strong laser pulses. This scheme is complementary to excitation by gamma photons generated via Compton backscattering as planned, e.g. for the ELI facility [25, 98], and to other direct or indirect nuclear excitation mechanisms utilizing optical [43, 99–103] or X-ray light sources [104–109].

Attempts to observe NERPA have not been conclusive so far. Only an upper bound of its cross section has been determined in the latest experiment [110] (see also [111]), therefore, the present theoretical study and future experimental work is anticipated to provide an unambiguous identification of the process and a determination of its true cross section.

Besides offering an alternative technique for nuclear spectroscopy, the theoretical and experimental investigation of NERPA is relevant for practical applications connected with positron-matter interaction. Firstly, the NERPA process may be relevant for cosmic ray studies with positron interacting with atoms in atmosphere (see e.g. [33]). Furthermore, in experimental investigations of nuclear reactors, NERPA may influence the dynamics of chain reactions involving β^+ emitters. A similar situation may occur in stellar evolution simulations [34]. The positron interacts in both cases with heavy atoms or ions. It is shown in the present work, that the transition rate of the NERPA process increases with the nuclear charge, thus the strength of this channel is boosted in high-Z elements.

The main aim of the present Chapter is to introduce the theory of NERPA, to provide a broad spectrum of numerical results and to discuss the possible situations allowing one to observe and experimentally investigate the process. To cover these goals, the Chapter is organized as follows: in § 17, the theory of nuclear excitation by positron annihilation is formulated in general terms; § 18 illustrates one of the suitable variants of the nuclear level scheme which can be used for the experimental investigation of the process. Finally, in § 19, numerical results for the NERPA effect in different elements are presented and discussed.

§ 17 Calculation of excitation rates

Non-monopole nuclear transitions

The NERPA process can be considered as the time reversed process of the electron-positron internal pair conversion with a bound electron accompanying the decay of an excited nucleus, described in Chapter I. In analogy with that derivation, the transition rate (probability per unit time) of NERPA is given by

$$P_{\mathrm{N}}^{j',j} = \frac{\delta(E+E'-\omega)}{[J_i,j',j]} \sum_{M_i=-J_i}^{J_i} \sum_{M_f=-J_f^*}^{J_f^*} \sum_{\mu=-j}^{j} \sum_{\mu'=-j'}^{j'} (2\pi)^2 \left| \alpha \int d\vec{r}_n \int d\vec{r}_f j_n(\vec{r}_n) j_f(\vec{r}_f) \frac{e^{i\omega|\vec{r}_n-\vec{r}_f|}}{|\vec{r}_n-\vec{r}_f|} \right|^2 . \quad (17.1)$$

Here, again, j and j' are the total angular momentum quantum numbers of the e^+ and e^- states, respectively, J_i and J_f^* are angular momenta of the nuclear initial and final states, and the M-s and μ-s are the associated magnetic quantum numbers. Furthermore, α is the fine-structure constant, $\vec{r}_n$ and $\vec{r}_f$ denote nuclear and fermionic coordinates. E and E' are the positron and electron

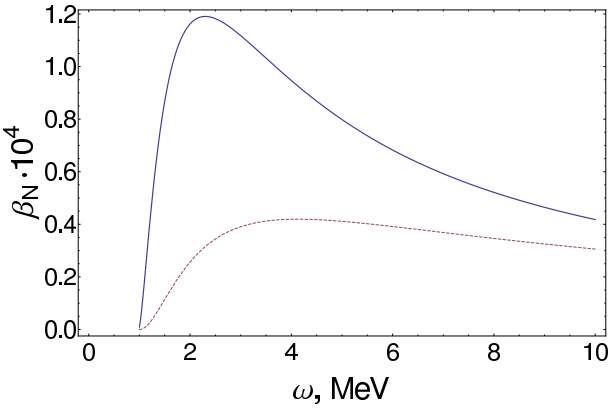

Figure 17.1 – The NERPA coefficient $\beta_N^{j',j}$ for $E2$ nuclear transition between $1/2+$ and $5/2+$ nuclear states vs. the photon energy ω for $Z = 50$ (^{115}Sn). Blue solid line: the case of $j = L - 1/2$, brown dashed line: $j = L + 1/2$.

energies, respectively, and, just as before, j_n and j_f are nuclear and fermionic 4-currents [88]. Also, the notation $[j_1, ..., j_k] = \prod_{i=1}^{k}(2j_i + 1)$ has been introduced for brevity. In the non-penetration approximation, introduced in Chapter I, it is again possible to factorize the NERPA transition rate as $P_N^{j',j} = \beta_N^{j',j} P_\gamma$, where P_γ is the rate for the state reached by NERPA to decay by γ emission into the initial state. One can provide this factorization for nuclear transitions of any multipolarity, with the exception of E0.

For the coefficient $\beta_N^{j',j}$ one may obtain expressions for any electric ($\lambda = E$) or magnetic ($\lambda = M$) nuclear transition multipolarity, i.e. for any (non-zero) values of the angular momentum L of the virtual photon:

$$\beta_N^{j',j}(\lambda L) = \frac{[J_f]}{[J_i, j', j]} \sum_{\kappa\kappa'} \frac{4\pi\alpha\omega}{L(L+1)} s|\kappa\kappa'|\rho_\lambda, \tag{17.2}$$

where the radial part for the $\lambda = E$ case is $\rho_E = |(\kappa - \kappa')(R_3 + R_4) + L(R_1 + R_2 + R_3 - R_4)|^2$, and for the $\lambda = M$ case $\rho_M = |(\kappa + \kappa')(R_5 + R_6)|^2$. We have also introduced the following notation in terms of a $3j$-symbol [69]: $s = \begin{pmatrix} j & j' & L \\ \frac{1}{2} & -\frac{1}{2} & 0 \end{pmatrix}^2$. The radial integrals R_a, $a \in \{1, \ldots, 6\}$ are defined as in Appendix A with the analytical form of the radial Coulomb-Dirac wave functions for bound and free particles. All results are obtained here for the $1s_{1/2}$ electron orbital, yielding the highest rate of NERPA.

Fig. 17.1 shows as an example the calculated dependence of the NERPA coefficient $\beta_N^{j',j}$ for an electric-quadrupole ($E2$) nuclear transition between $1/2+$ and $5/2+$ states on the virtual photon energy ω in ^{115}Sn. Curves are shown for two different possible positron angular momenta $j = L \pm 1/2$. Both values $\beta_N^{j',L\pm1/2}$ have to be taken into account in the calculation of the total cross section. One can see that nuclear transitions with energies about 2 MeV, which corresponds to the maximum of these curves, are preferred. It is also important to note here that the β_N values are fast increasing with rise in the atomic number, therefore, cross sections are largest in heavy atoms.

Monopole nuclear transitions

The case of electric monopole (E0) nuclear transitions excited by the NERPA process is separately discussed here. These $0^+ \to 0^+$ transitions are important for the investigation of the spectrum of deformed nuclei, since 0^+ states in heavy deformed nuclei are formed by a superposition of many oscillation modes and are objects of interest for microscopic nuclear models [112].

The direct one-photon nuclear excitation is forbidden in this case, therefore we compare the first (nuclear) step of the NERPA process to the dominant allowed nuclear decay channel of $0^+ \to 0^+$ nuclear transitions, namely, internal conversion (IC). The ratio $\delta_{\mathrm{N}}^{j',j}$ of the probabilities of the NERPA process and IC in the non-penetration approximation can be written as

$$P_{\mathrm{N}}^{j',j} = \delta_{\mathrm{N}}^{j',j} P_{\mathrm{IC}}. \tag{17.3}$$

Transition rates for the E0 case can be derived with the help of, e.g., Ref. [63] in a way similar to the derivation of Chapter I. The transition probabilities of the NERPA and IC processes are given by:

$$P_{\mathrm{N}}(j', j) = \frac{1}{[j, j']} \frac{\pi\alpha^2}{9} |M|^2 R^{4\gamma-4} |D_{\mathrm{N}}^{\kappa,\kappa'}|^2, \tag{17.4}$$

$$P_{\mathrm{IC}} = \frac{\pi\alpha^2}{9} |M|^2 R^{4\gamma-4} |D_{\mathrm{IC}}|^2. \tag{17.5}$$

Both expressions include the same matrix element M, the nuclear radius R and the individual radial parts:

$$|D_{\mathrm{N}}^{\kappa,\kappa'}|^2 = \left| \lim_{r\to 0} \frac{g_\kappa g_{\kappa'}}{r^{2\gamma-2}} \right|, \tag{17.6}$$

$$|D_{\mathrm{IC}}|^2 = \left| \lim_{r\to 0} \frac{g_{\kappa''} g_{\kappa'}}{r^{2\gamma-2}} \right|. \tag{17.7}$$

The radial functions g_κ and $g_{\kappa'}$ are the same as in the $L > 0$ case with Dirac quantum numbers for the free positron κ and the bound electron κ' in the case of NERPA as well as for initially bound κ'' and finel free κ' electron in the case of IC. Substituting the radial functions yields

$$|D_{\mathrm{N}}|^2 = \left| 2\sqrt{E+1} \frac{(2p)^\gamma e^{-\pi B/2} |\Gamma(a+1)|}{2\sqrt{\pi p}\,\Gamma(b)} (2\alpha Z)^{\gamma+1/2} \sqrt{\frac{1+\gamma}{2\Gamma(2\gamma+1)}} \cos(\eta) \right|^2, \tag{17.8}$$

where all abbreviations are the same as in the $L \neq 0$ case of IC (see, e.g., Appendix A). For D_{IC} one obtains, in accordance with [63]:

$$|D_{\mathrm{IC}}|^2 = \frac{1}{\pi} \left(\frac{\gamma+1}{2} \right)^2 \frac{(4\alpha Z\overline{p})^{2\gamma} e^{\pi\overline{B}}}{\overline{p}(\Gamma(2\Gamma+1))^3} \left| \Gamma(\gamma + i\overline{B}) \right|^2 2\alpha Z(\omega + 2\gamma), \tag{17.9}$$

where $\overline{E} = \gamma + \omega$, $\overline{p} = \sqrt{\overline{E}^2 - 1}$, $\overline{B} = \frac{\alpha Z \overline{E}}{\overline{p}}$. The sought-after ratio then is given by

$$\delta_{\mathrm{N}}^{j',j} = \frac{|D_{\mathrm{N}}^{\kappa,\kappa'}|^2}{4|D_{\mathrm{IC}}|^2}. \tag{17.10}$$

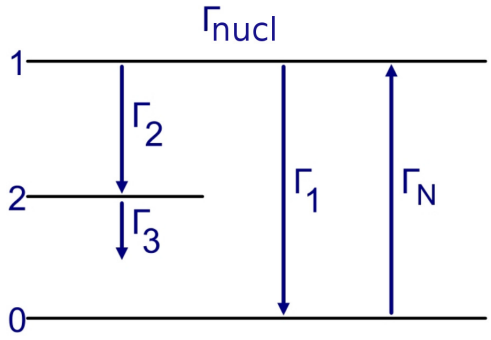

Figure 18.1 – Nuclear level scheme put forward for the observation of NERPA. Level 0 denotes the initial state, level 1 is the state populated by NERPA, and level 2 is the final metastable state. The resonance widths are assumed to satisfy $\Gamma_3 \ll \{\Gamma_1, \Gamma_2\}$.

§ 18 Proposed schemes for an experimental observation

Non-monopole nuclear transitions

A strightforward approach to observe the NERPA process is to detect the photons emitted by the decaying nuclei, but this is a comparably weak effect superimposed on the background of other photon emission processes in the studied system. To circumvent this problem, as in Refs. [90, 113], it is possible to consider nuclei with a long-living state, which can be populated by some radiative transition from the state excited by NERPA. The decay of this metastable state is the signature of the NERPA process, which may be measured with some time delay after the excitation takes place. The level scheme of the nucleus may be the one presented on Fig. 18.2 (a). Within this scheme, the state labeled as 2 is metastable, meaning that for its decay width holds: $\Gamma_3 \ll \{\Gamma_1, \Gamma_2\}$, where the Γ-s denote transition widths as in Fig. 18.2(a). Γ_N stands for the resonance width of the NERPA transition, which is related to the γ emission width as

$$\Gamma_N = \sum_j [j] \beta_N^{1/2,j} \Gamma_1 . \tag{18.1}$$

The cross section of the total process in dependence on the positron kinetic energy E (and corresponding momentum $p = \sqrt{E^2 - 1}$) is given by the expression

$$\sigma_{N\gamma}(E) = \frac{2\pi^2}{p^2} \frac{\Gamma_2^\gamma}{\Gamma_{\text{nucl}}} \frac{\Gamma_{\text{tot}}/(2\pi)}{(E - E_{\text{res}})^2 + \Gamma_{\text{tot}}^2/4} \Gamma_N \,, \tag{18.2}$$

where E_{res} is the resonance energy, Γ_2^γ is the resonance width of the γ decay of the final NERPA state to the metastable state. This width is connected to the internal conversion coefficient α_{IC} through $\Gamma_2^\gamma = \Gamma_2/(1 + \alpha_{\text{IC}})$. $\Gamma_{\text{nucl}} = \hbar/\tau$ is the total width of the considered nuclear level, expressed in terms of its lifetime τ. For a derivation of cross sections of nuclear-resonant processes, see Appendix B. It follows from this relation that the total resonance line width is given as the sum of the nuclear and atomic K-shell widths [114]: $\Gamma_{\text{tot}} = \Gamma_{\text{nucl}} + \Gamma_K$. The nuclear excitation cross section σ_N can be obtained from the above formula by substituting the branching ratio $\Gamma_2^\gamma/\Gamma_{\text{nucl}}$ by 1.

Table 18.1 – Data for different elements which suit the nuclear level scheme in Fig. 18.2 (a). Notations are as defined there and in the text. The symmetry ("symm.") of the nuclear levels involved – total angular momentum, parity – is given. Nuclear data are taken from Ref. [75].

Element	^{72}Ge	^{174}Hf	^{115}Sn	^{115}In
$E_{\rm res}$ (keV)	456	281	430	90
level 0 symm.	0^+	0^+	$1/2^+$	$9/2^+$
level 1 (keV); symm.	1464; 2^+	1227; 2^+	1417; $5/2^+$	1078; $5/2^+$
level 2 (keV); symm.	691; 0^+	91; 2^+	613; $7/2^+$	336; $1/2^+$
lifetime of level 2, τ_2	444 ns	1.66 ns	3.26 μs	4.5 h
Γ_1 (eV)	$1.8 \cdot 10^{-5}$	$9.00 \cdot 10^{-4}$	$1.39 \cdot 10^{-3}$	$5.54 \cdot 10^{-4}$
Γ_2^γ (eV)	$1.7 \cdot 10^{-7}$	$4.04 \cdot 10^{-4}$	$9.9 \cdot 10^{-5}$	$1.05 \cdot 10^{-4}$
Γ_3 (eV)	$1.5 \cdot 10^{-9}$	$3.965 \cdot 10^{-7}$	$2.02 \cdot 10^{-10}$	$4.06 \cdot 10^{-20}$
$\beta_{\rm N}$	$2.7 \cdot 10^{-5}$	$7.6 \cdot 10^{-5}$	$4.1 \cdot 10^{-5}$	$1.9 \cdot 10^{-6}$
$\Gamma_{\rm nucl}$ (eV)	$1.5 \cdot 10^{-4}$	$1.83 \cdot 10^{-3}$	$1.88 \cdot 10^{-3}$	$6.6 \cdot 10^{-4}$
Γ_K (eV)	1.37	33.0	7.9	7.3
$\sigma_{\rm N}(E_{\rm res})$ (b)	$4.3 \cdot 10^{-5}$	$1.1 \cdot 10^{-4}$	$1.5 \cdot 10^{-4}$	$1.7 \cdot 10^{-5}$
$\sigma_{{\rm N}\gamma}(E_{\rm res})$ (b)	$3.1 \cdot 10^{-9}$	$6.1 \cdot 10^{-6}$	$3.1 \cdot 10^{-6}$	$1.1 \cdot 10^{-6}$

In Tab. 18.1 results for 4 different elements are presented, namely, for ^{72}Ge, ^{174}Hf, ^{115}Sn, and ^{115}In. All these elements possess the level scheme presented in Fig. 18.1, and an $E2$ nuclear transition for the NERPA process. For ^{174}Hf, the cross section $\sigma_{{\rm N}\gamma}$ is the largest. However, here, the metastable level has a comparably short lifetime τ_2, which may not be sufficient for an experimental differentiation of the signal from the direct electron-positron photoannihilation process. The comparably large value of the cross section together with the lifetime τ_2 for the case of ^{115}Sn and ^{115}In are most suitable for a possible measurement. The NERPA process is significantly enhanced for some elements such as e.g. ^{174}Hf and ^{115}Sn. Besides the increase of the β coefficient with Z, it is also because for these isotopes, the nuclear transition energy renders β nearly maximal (see Fig. 17.1). In the case of ^{115}In, it is rather the small resonant positron kinetic energy that boosts the total NERPA cross section due to the pre-factor $\propto 1/p^2$ in Eq. (18.2).

Monopole nuclear transitions

The case of electric monopole (E0) nuclear transitions excited by the NERPA process has to be separately discussed. As mentioned in the previous section, the case of electric monopole nuclear transitions excited by the NERPA process is of relevance for the investigation of the spectrum of deformed nuclei, since 0^+ states in heavy deformed nuclei are formed by a superposition of many oscillation modes and are objects of interest for microscopic nuclear models [112].

E0 NERPA excitations can be useful for the investigation of 0^+ level cascades in heavy deformed nuclei. ^{168}Er is a typical example of such nuclei, having a 0^+ ground state and a 0^+ excited state at an energy of 1.217 MeV, which can decay by $E2$ gamma emission to a

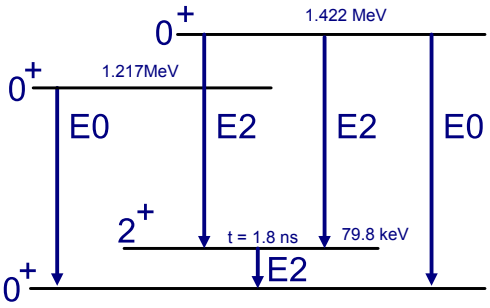

Figure 18.2 – The lowest 0^+ and 2^+ nuclear levels in $^{168}_{68}$Er. See text for details.

metastable 2^+ level at an energy of 79.8 keV with a lifetime of 1.853 ns (see Fig. 18.2). Here, the γ-decay of the metastable level follows the NERPA process. In principle, one may also find several other 0^+ levels with higher energies, however, for E0 NERPA excitation it is better to consider low energies just above the pair production threshold. For the described level scheme, the lifetime of the excited 0^+ level and the intensity of the $0^+ \to 0^+$ transition are unknown, however, it is possible to calculate the rate of IC transition between these levels, for instance following Ref. [115], and then, with the help of the δ coefficient, the rate and width of the NERPA transition. Then one can obtain the cross section of the total NERPA process depending on the probability of the $0^+ \to 2^+$ deexcitation via $E2$ γ decay. As a result, the expression for the NERPA cross section at resonance can be received:

$$\sigma_{\mathrm{N}\gamma}(E_{\mathrm{res}}) = \frac{4\pi}{p^2}\frac{\Gamma_{\mathrm{N}}}{\Gamma_\gamma}\,, \tag{18.3}$$

where (in SI units) [116]

$$\Gamma_\gamma = 0.123 \cdot 10^{10} \cdot \hbar (E_\gamma)^5 \cdot B_{E2}\,. \tag{18.4}$$

Here, B_{E2} is the reduced transition probability of the $0^+ \to 2^+$ deexcitation [in units of $e^2(\mathrm{fm}^4)$], Γ_γ and E_γ are expressed in MeV, $\hbar$ in MeV·s.

In the case of the first excited 0^+ state in ^{168}Er, the values are the following: $\Gamma_{\mathrm{IC}} = 7.08 \cdot 10^{-12}$ MeV, $\delta = 0.17$, $\Gamma_{\mathrm{N}} = 1.19 \cdot 10^{-12}$ MeV, yielding

$$\sigma(E = E_{res})[\mathrm{b}] = 1.12 \cdot 10^{-11}/B_{E2}. \tag{18.5}$$

The cross section of the total NERPA process may be determined experimentally. This measurement allows one to obtain the reduced $E2$ transition probability for the second step of the NERPA process. This quantity is connected with the nuclear deformation parameter, thus the latter can be inferred from NERPA measurements and may be used to benchmark nuclear structure models.

§ 19 Numerical results for different elements

Several elements over the whole range of the periodic table may feature significant NERPA cross sections. Numerical results for some important cases are listed in Tabs. 19.1 and 19.2. The light elements such as C, N, O and Fe (see Tab. 19.1) typically occur in biological environments

Table 19.1 – Results for a range of light elements. ΔE denotes the energy of the excited nuclear state, Γ_γ and $\Gamma_{\rm nucl}$ are its radiative and total decay width, respectively. See text for further details. Nuclear data are taken from Ref. [75].

Element	^{12}C	^{14}N	^{16}O	^{56}Fe
ΔE (keV)	4439	2313	6917	2958
$E_{\rm res}$ (keV)	3418	1289	5899	1947
Multipolarities	$2^+ \overset{E2}{\to} 0^+$	$1^+ \overset{M1}{\to} 0^+$	$0^+ \overset{E2}{\to} 2^+$	$0^+ \overset{E2}{\to} 2^+$
$\beta_{\rm N}$	$2.1 \cdot 10^{-8}$	$9.1 \cdot 10^{-10}$	$9.1 \cdot 10^{-7}$	$3.2 \cdot 10^{-5}$
$\Gamma_{\rm nucl}$ (eV)	$1.08 \cdot 10^{-2}$	$9.7 \cdot 10^{-3}$	$1.4 \cdot 10^{-1}$	$2.4 \cdot 10^{-2}$
Γ_γ (eV)	$1.08 \cdot 10^{-2}$	$9.7 \cdot 10^{-3}$	$1.4 \cdot 10^{-1}$	$5.1 \cdot 10^{-4}$
Γ_K (V)	$2.0 \cdot 10^{-3}$	$3.6 \cdot 10^{-3}$	$6.0 \cdot 10^{-3}$	$6.1 \cdot 10^{-1}$
$\sigma_{\rm N}$ (b)	$1.1 \cdot 10^{-5}$	$2.2 \cdot 10^{-5}$	$2.1 \cdot 10^{-4}$	$2.1 \cdot 10^{-3}$
$\sigma_{\rm C}$ (b)	6.7	0.039	9.4	2.1

and in solar plasmas. In addition, Fe is present in large quantities in the radiation zone of the Sun. The results for these light atoms are also of importance in cosmic ray studies and in medical positron tomography research. Table 19.1 summarizes widths and resonance cross sections for the one-step NERPA process for these elements. For Fe, the NERPA cross section $\sigma_{\rm N}$ is even larger then in the case of ^{115}Sn and ^{115}In (see Tab. 18.1). However, $\sigma_{\rm N}$ compared with the corresponding cross sections for Coulomb excitation with high-energy protons (or positrons) appears to be not so strong.

Further results for elements with different Z can be seen from the Tab. 19.2. In several cases, for instance, ^{38}K and for the 2101-keV transition in ^{18}F, NERPA is up to an order of magnitude stronger than the Coulomb excitation. For other elements, such as ^{14}N and ^{21}Ne, the cross sections are comparable. Separately, the case of the excitation of nuclear giant resonances should be stressed. The data for the giant dipole resonance (in ^{208}Pb and ^{110}Sn) and for the quadrupole resonance in ^{110}Sn can be found in Tab. 19.3).

The strongest NERPA excitation so far has been identified for a 13.5-MeV giant dipole resonance (GDR) in ^{208}Pb. Since for such resonances the nuclear level width is in the MeV range, these resonances also feature the highest integrated NERPA cross sections. For instance, the estimation of the NERPA cross section integrated with the effective resonance width reaches $\int \sigma_{\rm N}(E)dE = 3.4 \cdot 10^4$ b·eV for the mentioned GDR in ^{208}Pb, exceeding previous values for e.g. ^{115}In by 8 orders of magnitude. GDRs can be efficiently excited even with a broadband positron source generated in laser-plasma interactions by existing novel methods [41, 97]. E.g., for a positron beam with a 0.5-MeV width, Coulomb excitation of the GDR is not significant, since it requires positron kinetic energies higher by approximately $2mc^2$ than NERPA. Therefore, exciting GDRs with laser-generated positron beams may be a viable alternative to observe NERPA, circumventing the difficulties caused by the low nuclear line width in elements such as ^{115}In [110]. Furthermore, NERPA can be used for the excitation of a certain energy region of a giant resonance, enabling the investigation of the thermal evolution of the GDR width and structure. Normally such studies are done by Coulomb excitation [117, 118] which does not

Table 19.2 – Results for a range of medium-Z elements. ΔE denotes the energy of the excited nuclear state, Γ_γ and Γ_{nucl} are its radiative and total decay width, respectively. See text for further details. Nuclear data are taken from Ref. [75].

Element	^{38}K	^{14}N	^{18}F	^{18}F	^{21}Ne
ΔE (keV)	2646	5691	1081	2101	2788
E_{res} (keV)	1629	4670	60	1080	1767
Multipolarities	$3^+ \xrightarrow{E1} 4^-$	$1^+ \xrightarrow{E1} 1^-$	$1^+ \xrightarrow{E1} 0^-$	$1^+ \xrightarrow{E1} 2^-$	$3/2^+ \xrightarrow{E1} 1/2^-$
β_{N}	$3.2 \cdot 10^{-6}$	$1.2 \cdot 10^{-7}$	$2.1 \cdot 10^{-8}$	$5.3 \cdot 10^{-7}$	$2.2 \cdot 10^{-7}$
Γ_{nucl} (eV)	$6.7 \cdot 10^{-7}$	$6.0 \cdot 10^{-2}$	$3.4 \cdot 10^{-5}$	$1.9 \cdot 10^{-4}$	$8.1 \cdot 10^{-6}$
Γ_γ (eV)	$6.6 \cdot 10^{-7}$	$2.2 \cdot 10^{-2}$	$3.4 \cdot 10^{-5}$	$7.1 \cdot 10^{-5}$	$1.4 \cdot 10^{-6}$
Γ_K (eV)	$1.8 \cdot 10^{-2}$	$3.6 \cdot 10^{-3}$	$9.5 \cdot 10^{-3}$	$9.5 \cdot 10^{-3}$	$1.4 \cdot 10^{-2}$
σ_{N} (b)	$2.6 \cdot 10^{-7}$	$4.2 \cdot 10^{-5}$	$1.2 \cdot 10^{-5}$	$4.5 \cdot 10^{-5}$	$2.4 \cdot 10^{-7}$
σ_{C} (b)	$2.4 \cdot 10^{-8}$	$7.1 \cdot 10^{-5}$	$1.9 \cdot 10^{-5}$	$5.3 \cdot 10^{-6}$	$4.2 \cdot 10^{-8}$

Table 19.3 – Results for giant resonances in ^{208}Pb and ^{110}Sn. ΔE denotes the energy of the excited nuclear state, Γ_γ and Γ_{nucl} are its radiative and total decay width, respectively. See text for further details. Nuclear data are taken from Ref. [75].

Element	^{208}Pb	^{110}Sn	^{110}Sn
ΔE (keV)	13500	14800	29000
E_{res} (keV)	12600	13800	28000
Multipolarities	$0^+ \xrightarrow{E1} 1^-$	$0^+ \xrightarrow{E1} 1^-$	$0^+ \xrightarrow{E2} 2^+$
β_{N}	$9.6 \cdot 10^{-5}$	$3.2 \cdot 10^{-5}$	$3.0 \cdot 10^{-5}$
Γ_{nucl} (eV)	$4 \cdot 10^{6}$	$8 \cdot 10^{6}$	$8 \cdot 10^{6}$
Γ_γ (eV)	$4 \cdot 10^{6}$	$8 \cdot 10^{6}$	$8 \cdot 10^{6}$
Γ_K (eV)	$5.5 \cdot 10^{1}$	$7.9 \cdot 10^{0}$	$7.9 \cdot 10^{0}$
σ_{N} (b)	$5.5 \cdot 10^{-3}$	$1.5 \cdot 10^{-3}$	$3.9 \cdot 10^{-4}$
σ_{C} (b)	$6.3 \cdot 10^{2}$	$9.9 \cdot 10^{2}$	$2.0 \cdot 10^{5}$

allow a selective excitation but only an energy-selective detection of subsequent γ decays. The problem of the theoretical description of the excitation of the certain part of the GDR is caused by the complicated resonance structure consisting of the superposition of the several nuclear states. To calculate the integrated excitation cross section in this case one has to use some model for the GDR strength function. For instance, it can be the double-Lorentzian model of the strength function [119, 120] for the case of the wide incoming positron distribution or some more precise model, e.g. [121].

Another application of giant resonances where the energy selectivity of NERPA due to its resonance structure is beneficial is the feeding of highly deformed states by the low-energy GDR component [122]. This feeding effect is relevant for the investigation of the low-energy limit of the radiative dipole strength [123], which, in turn, has consequences in astrophysical

simulations of the r-process nucleosynthesis of exotic nuclei [124].

§ 20 Discussion

In summary, positron annihilation with a shell electron is put forward as an alternative way to induce transitions in nuclei at the MeV level. This channel combines advantages of processes typically used to excite nuclei, namely, Coulomb- and photo-excitation. NERPA provides a resonant character of the excitation together with a significant cross section for any multipolarity of the excited nuclear transition.

Nowadays laser-produced positron beams may provide sufficient flux for efficient indirect nuclear excitation. This work shows that cross sections are largest in medium-Z and heavy elements with the nuclear transition energy near the maximum of the cross section about 2 MeV. In elements satisfying these properties and also possessing a metastable state populated by NERPA, the slow γ decay may provide appropriate time gating for the observation of the reaction. The NERPA process is, furthermore, potentially relevant in numerous applications connected with positron-matter interaction, and is also anticipated to provide one with a novel means for the investigation of the structure of deformed nuclei and for nuclear model tests.

Chapter IV

Internal pair conversion following Coulomb excitation

§ 21 Introduction to internal pair conversion following Coulomb excitation

A large amount of different particles are produced in nucleus-nucleus collisions involving heavy ions. In the framework of FAIR experiments in the near future it will be possible to observe the bound-free and free-free pair production in the in the combined electromagnetic field of two colliding nuclei, which becomes supercritical for a short amount of time during the collision [23].

This Chapter introduces a new mechanism of pair production which can take place in ion-ion collisions. Here, the target nucleus is excited by a Coulomb collision with the projectile, and it subsequently deexcites by internal pair conversion. Here, both bound-free and free-free internal pair conversion may happen.

The theory of this nuclear-resonant electron-positron pair creation in heavy ion collisions can be constructed by considering two steps. In the first step, the projectile nucleus, which is supposed to be light compared to the target one, excites the heavy, completely ionized target via Coulomb excitation. Then, the target nucleus within its deexcitation produces an electron-positron pair with the electron bound in the same ion. The second part of this process is already described above in Chapter I. Therefore, we can use corresponding results concerning the internal pair conversion coefficient β. The present Chapter considers mostly the first step of this process, as well as the cross section of the final 2-step process.

This Chapter is organized as follows. In § 22, the derivation of the Coulomb excitation cross section is presented for our purposes in the non-relativistic approximation. Then, in § 23, the cross section of the 2-step process is discussed. § 24 contains numerical results for the described processes in the non-relativistic case. A comparison to the relativistic case is given in § 25. Finally, in § 26, a comparison to the non-resonant, direct pair creation process is provided.

§ 22 Coulomb excitation cross section in a non-relativistic approach

The T-matrix of the Coulomb excitation of the heavy ion from an initial state α to a final state β in the non-relativistic case has the following form as an expansion by 2^l-pole momenta [125]:

$$T = \sum_{lm}(-1)^m R_l^{-m}\langle\beta J_\beta M_\beta|Q_l^m|\alpha J_\alpha M_\alpha\rangle, \tag{22.1}$$

$$R_l^m = \frac{4\pi Z_t Z_p}{2l+1}\int \zeta_b^{(-)*}(\vec{r})\frac{Y_l^m(\Omega)}{r^{l+1}}\zeta_a^{(+)}(\vec{r})d\vec{r}, \tag{22.2}$$

where J_α and J_β are initial and final nuclear angular momenta, M_α and M_β are the corresponding projections, Q_l^m is a component of the 2^l-pole moment operator with a projection taking values $m = -l, ..., +l$, and Z_t and Z_p are the charges of the target and the projectile, respectively. Ω denotes the angular coordinates of the outgoing projectile. The initial and final wave functions of the incident particle have the form of a Coulomb wave function [125]:

$$\zeta_a^{(+)}(\overrightarrow{r}) = \frac{4\pi}{k_a r}\sum_{l'm'} i^{l'} F_{l'}^{(+)}(k_a, r)Y_{l'}^{m'*}(0,0)Y_{l'}^{m'}(\Omega'), \tag{22.3}$$

$$\zeta_b^{(-)}(\overrightarrow{r}) = \frac{4\pi}{k_b r}\sum_{l''m''} i^{l''} F_{l''}^{(-)}(k_b, r)Y_{l''}^{m''*}(\Omega)Y_{l''}^{m''}(\Omega'), \tag{22.4}$$

where k_a and k_b are momenta of the incident particle before and after collision, Y_l^m is a spherical function, Ω' denotes the angular part of $\vec{r}$ and the Coulomb function is [125]:

$$F_l^{(\pm)}(k, r) = W_l^{(\pm)}(Z_t Z_p M/k, kr), \tag{22.5}$$

$$W_l^{(\pm)}(\eta, \rho) = \frac{2^l e^{-\pi\eta/2}|\Gamma(l+1+i\eta)|}{\Gamma(2l+2)}\rho^{l+1}e^{-i\rho}{}_1F_1(l+1\pm i\eta; 2l+2; \mp 2i\rho), \tag{22.6}$$

with the reduced mass $M = \frac{M_t M_p}{(M_t+M_p)}$, where M_t and M_P are masses of the target and projectile, and Γ is a gamma function as defined in Ref. [66]. After integration over Ω' one obtains for R_l^m [125]

$$R_l^m = \frac{(4\pi)^3 Z_t Z_p}{2(2l+1)\sqrt{\pi}k_a k_b}N_l^m(k_a, k_b, \Omega), \tag{22.7}$$

$$N_l^m(k_a, k_b, \Omega) = Y_l^m(\Omega)\sum_{l'}(-1)^{l'}\sqrt{2l'+1}Y_{l'}^{0*}(\Omega)\int_0^\infty dr\frac{1}{r^{l+1}}F_{l'}(k_a, r)F_{l'}(k_b, r). \tag{22.8}$$

The last radial integral contains highly oscillating function as integrand, which can cause some problems in a direct numerical evaluation. Nevertheless, this integral can be calculated by the change of the integration order of the main integral and in of the integral representations of the hypergeometric functions ${}_1F_1$. For instance, in the calculation of the integral

$$I = \int dz z^l e^{-i(k_1+k_2)z}{}_1F_1(a_1, b, -2ik_1 z){}_1F_1(a_2, b, 2ik_2 z), \tag{22.9}$$

one can rewrite it as

$$
\begin{aligned}
I &= \int dz z^l e^{-i(k_1+k_2)z} \frac{\Gamma(b)}{\Gamma(a_1)\Gamma(b-a_1)} \frac{\Gamma(b)}{\Gamma(a_2)\Gamma(b-a_2)} && (22.10)\\
&\times \int_0^1 dt t^{a_1-1}(1-t)^{b-a_1-1} e^{-2ik_1zt} \int_0^1 du \cdot u^{a_2-1}(1-u)^{b-a_2-1} e^{+2ik_2zu} \\
&= \frac{\Gamma(b)}{\Gamma(a_1)\Gamma(b-a_1)} \frac{\Gamma(b)}{\Gamma(a_2)\Gamma(b-a_2)} && (22.11)\\
&\times \int_0^1 dt \int_0^1 du t^{a_1-1}(1-t)^{b-a_1-1} u^{a_2-1}(1-u)^{b-a_2-1} \int dz z^l e^{-i(k_1z+k_2z+2ik_1t-2ik_2u)z} \\
&= \frac{\Gamma(b)}{\Gamma(a_1)\Gamma(b-a_1)} \frac{\Gamma(b)}{\Gamma(a_2)\Gamma(b-a_2)} \Gamma(l+1) i^{(-(l+1))} && (22.12)\\
&\times \int_0^1 dt \int_0^1 du t^{a_1-1}(1-t)^{b-a_1-1} u^{a_2-1}(1-u)^{b-a_2-1} (k_1+k_2+2k_1t-2k_2u)^{-(l+1)}.
\end{aligned}
$$

The last double integral does not contain an oscillating integrand and can be easily calculated numerically.

Following [125], it is possible to write the differential Coulomb excitation cross section as:

$$
\frac{d\sigma}{d\Omega} = \frac{1}{2J_\alpha+1} \frac{1}{2l_0+1} \frac{M^2 v_b}{4\pi^2\hbar^4 v_a} |\langle\beta\|Q^{l_0}\|\alpha\rangle|^2 \sum_m |R^m_{l_0}|^2, \tag{22.13}
$$

with the reduced quadrupole moment $|\langle\beta\|Q^{l_0}\|\alpha\rangle|$, where l_0 is the smallest possible value of l. v_a and v_b denote projectile velocities before and after the interaction with the target.

The reduced quadrupole moment $\langle\beta\|Q^{l_0}\|\alpha\rangle$ can be extracted from the expression for the probability of the corresponding γ-process in the same nucleus. This probability is given by [65]:

$$
P^\gamma_{jm} = \frac{2(2j+1)(j+1)}{j((2j+1)!!)^2} \omega^{2j+1} \frac{1}{2J_\beta+1} |\langle J_\alpha j M_\alpha m|J_\beta M_\beta\rangle|^2 |\langle\beta\|Q^j\|\alpha\rangle|^2, \tag{22.14}
$$

where ω is the nuclear transition energy, and the Clebsch-Gordan coefficients are taken in the form introduced by Edmonds [126]. For the reduced quadrupole moment one has as a result

$$
|\langle\beta\|Q^j\|\alpha\rangle|^2 = P^\gamma_j \frac{j((2j+1)!!)^2}{2(2j+1)(j+1)} \omega^{-(2j+1)} (2J_\beta+1) \sum_m \frac{1}{|\langle J_\alpha j M_\alpha m|J_\beta M_\beta\rangle|^2}. \tag{22.15}
$$

One can write the final expression for the Coulomb cross section by substituting here the obtained equation for the quadrupole moment:

$$
\begin{aligned}
\frac{d\sigma_{\text{Coulomb}}}{d\Omega} &= \frac{2J_\beta+1}{2J_\alpha+1} \frac{1}{2l_0+1} \frac{l_0((2l_0+1)!!)^2}{2(2l_0+1)(l_0+1)} && (22.16)\\
&\times \omega^{-(2l_0+1)} \frac{M^2 v_b}{4\pi^2\hbar^4 v_a} \sum_m |R^m_{l_0}|^2 \sum_m \frac{1}{|\langle J_\alpha l_0 M_\alpha m|J_\beta M_\beta\rangle|^2} P^\gamma_{l_0}.
\end{aligned}
$$

§ 23 Cross section of the 2-step process

The derivation of the cross section of the described 2-step process is similar to the derivation of the cross section of the 2-step NERPA-γ process described in Chapter III and Appendix B. Therefore, one can write an expression for the total cross section as

$$\sigma(E) = \frac{2\pi^2}{p_a^2} \frac{\Gamma_{\text{Coulomb}} \Gamma_{\text{bf}}^{\text{IPC}}}{\Gamma_{\text{tot}}} \Lambda_{\text{tot}}(E), \tag{23.1}$$

where p_a is the projectile moment, Γ_{Coulomb} is the width of the Coulomb excitation process, $\Gamma_{\text{bf}}^{\text{IPC}}$ is the width of the nuclear deexcitation by bound-free pair creation, Γ_{tot} is the total natural width of the excited nuclear state, and the Lorentz profile is:

$$\Lambda_{\text{tot}}(E) = \frac{\Gamma_{\text{tot}}/(2\pi)}{(E-\omega)^2 + \Gamma_{\text{tot}}^2/4} \tag{23.2}$$

with E being the energy transferred to the target during the collision.

The width of the Coulomb excitation may be written as [127, 128]:

$$\Gamma_{\text{Coulomb}} = \frac{(2J_\alpha + 1)\Gamma_{\text{tot}}}{2J_\beta + 1} \int \frac{d\sigma_{\text{Coulomb}}/d\Omega}{d\sigma_{\text{Rutherford}}/d\Omega} I_{\text{out}}(\Omega) d\Omega, \tag{23.3}$$

where $d\sigma_{\text{Rutherford}}/d\Omega$ is the Rutherford scattering cross section [129], $I_{\text{out}}(\Omega)d\Omega$ is the intensity of outgoing projectile particles per incoming particle in the solid angle element $d\Omega$. The last quantity is given by

$$I_{\text{out}}(\Omega)d\Omega = \frac{d\sigma_{\text{Coulomb}}/d\Omega}{\int (d\sigma_{\text{Coulomb}}/d\Omega) d\Omega}. \tag{23.4}$$

Finally, for the width Γ_{Coulomb} we can write:

$$\Gamma_{\text{Coulomb}} = \frac{\Gamma_{\text{tot}}}{\int (d\sigma_{\text{Coulomb}}/d\Omega) d\Omega} \frac{(2J_\alpha + 1)}{(2J_\beta + 1)} \int d\Omega \frac{(d\sigma_{\text{Coulomb}}/d\Omega)^2}{d\sigma_{\text{Rutherford}}/d\Omega}. \tag{23.5}$$

For a compact description of our results we use the following notation:

$$\sigma(E, E') = \lambda'(E', E) \Gamma_{\text{bf}}^{\text{IPC}} \Gamma^\gamma \Lambda_{\text{tot}}(E), \tag{23.6}$$

where ω is the nuclear excitation energy, E' is the initial projectile energy, Γ^γ is the width of the corresponding photo-excitation process and λ' is a newly introduced coefficient, having the dimension of cross section per energy.

The strength function for this process is defined as

$$S(E') = \int dE \sigma(E, E'). \tag{23.7}$$

We then define a new coefficient λ as

$$\lambda(E') = \int dE \lambda'(E', E) \Lambda_{tot}(E), \tag{23.8}$$

and assuming a narrow nuclear line we get the result

$$\lambda(E') = \lambda'(E', \omega), \tag{23.9}$$

and

$$S(E') = \lambda(E')\Gamma_{bf}^{IPC}\Gamma^{\gamma}. \tag{23.10}$$

The final analytical expression for $\lambda(E')$ reads:

$$\lambda(E') = \frac{2\pi}{p_a^2}\frac{(2J_\alpha + 1)}{(2J_\beta + 1)\int d\Omega\zeta_C(\Omega)}\int d\Omega\frac{\zeta_C^2(\Omega)}{\zeta_R(\Omega)}, \tag{23.11}$$

where

$$\zeta_C(\Omega) = \frac{d\sigma_{\text{Coulomb}}/d\Omega}{\Gamma^{\gamma}}, \tag{23.12}$$

$$\zeta_R(\Omega) = \frac{d\sigma_{\text{Rutherford}}}{d\Omega}. \tag{23.13}$$

In the next Section numerical results for $\lambda(E')$ will be presented.

The width of bound-free pair conversion can be written in terms of the bound-free pair production coefficient β_{bf} introduced in Chapter I:

$$\Gamma_{\text{bf}}^{\text{IPC}} = \beta_{\text{bf}}\Gamma^{\gamma}. \tag{23.14}$$

As it has been shown in Chapter I, this dimensionless coefficient can reach values up to 10^{-4} for nuclear transition energies just above the pair production threshold in nuclear transitions in heavy elements.

The total strength is then given by

$$S(E') = \lambda(E')\beta_{bf}(\Gamma^{\gamma})^2, \tag{23.15}$$

where β_{bf} has been considered in details in Chapter I and $\lambda(E')$ is investigated in the following sections.

§ 24 Numerical results in a non-relativistic approach

The following numbers have been used for the description of the $E1$ nuclear Coulomb excitation (from 0^+ to 1^-) in ^{208}Pb at energy $\omega = 4.84146$MeV by a light particle [130]:

$$Z_{\text{target}} = 82; \tag{24.1}$$

$$M_{\text{target}} = 208 \cdot 931.49406\,\text{MeV} - 16.8529\,\text{MeV}; \tag{24.2}$$

$$M_{\text{projectile}} = N \cdot 931.49406\,\text{MeV} + 7.288971\,\text{MeV}, \tag{24.3}$$

where Z and N are the charge and the mass number of the projectile. Here and later the nuclear masses are taken from [130]. For instance, for a proton the projectile energy is

$$E' = M_{\text{projectile}} + N_{\text{projectile}} \times 5[\text{MeV}] + \omega, \tag{24.4}$$

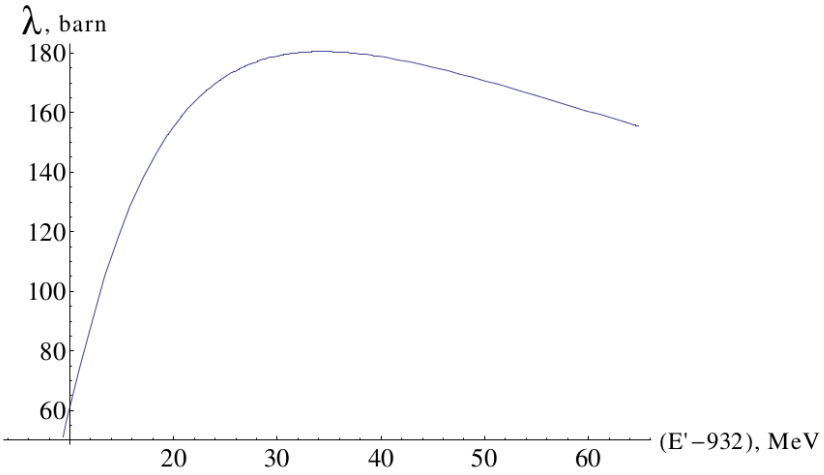

Figure 24.1 – The dependence of the λ coefficient on the incident proton energy for low proton energies.

Table 24.1 – Numerical data for different projectiles. The projectile energy is assumed to behave as $E' = M_{\text{projectile}} + N \cdot 5[\text{MeV}] + \omega$. See notations in the text.

	Z	N	λ, barn $\cdot$ MeV^{-1}	S_{bf}, barn·MeV	S_{ff}, barn·MeV
^{1}H	1	1	$0.59 \cdot 10^{+2}$	$1.7 \cdot 10^{-12}$	$1.0 \cdot 10^{-11}$
^{4}He	2	4	$4.72 \cdot 10^{+2}$	$1.3 \cdot 10^{-11}$	$8.0 \cdot 10^{-11}$
^{3}He	2	3	$3.28 \cdot 10^{+2}$	$9.2 \cdot 10^{-12}$	$5.6 \cdot 10^{-11}$
^{9}Be	4	9	$5.94 \cdot 10^{+2}$	$1.7 \cdot 10^{-11}$	$1.0 \cdot 10^{-10}$
^{12}C	6	12	$4.22 \cdot 10^{+2}$	$1.2 \cdot 10^{-11}$	$7.2 \cdot 10^{-11}$
^{6}C	6	6	$2.66 \cdot 10^{+2}$	$7.4 \cdot 10^{-12}$	$4.5 \cdot 10^{-11}$
^{23}Na	11	23	$1.45 \cdot 10^{+2}$	$4.1 \cdot 10^{-12}$	$2.5 \cdot 10^{-11}$

and the numerical value of the λ coefficient is $\lambda(E') = 58.8\,\text{barn} \cdot \text{MeV}^{-1}$. For this certain $1^- \to 0^+$ γ-transition, the lifetime is $\tau = 0.068$ fs, which gives $\Gamma^\gamma = \hbar/\tau = 9.7 \cdot 10^{-6}\,\text{MeV}$. Following the equations of Chapter I it is possible to calculate the bound-free pair production coefficient for this case: $\beta_{\text{bf}}(\omega) = 3 \cdot 10^{-4}$. Therefore, the total strength of the two-step Coulomb excitation – bound-free pair production deexcitation process is

$$S_{\text{bf}}(E') = 1.7 \cdot 10^{-12}\,\text{barn} \cdot \text{MeV}. \tag{24.5}$$

For the corresponding free-free pair production process, the pair conversion coefficient is $\beta_{\text{ff}}(\omega) = 1.8 \cdot 10^{-3}$, thus the strength of the resonance is

$$S_{\text{ff}}(E') = 1.0 \cdot 10^{-11}\,\text{barn} \cdot \text{MeV}. \tag{24.6}$$

The dependence of the λ coefficient on the incident proton energy is shown in Fig. 24.1 and Fig. 24.2. For heavier projectiles the results are presented in Table 24.1.

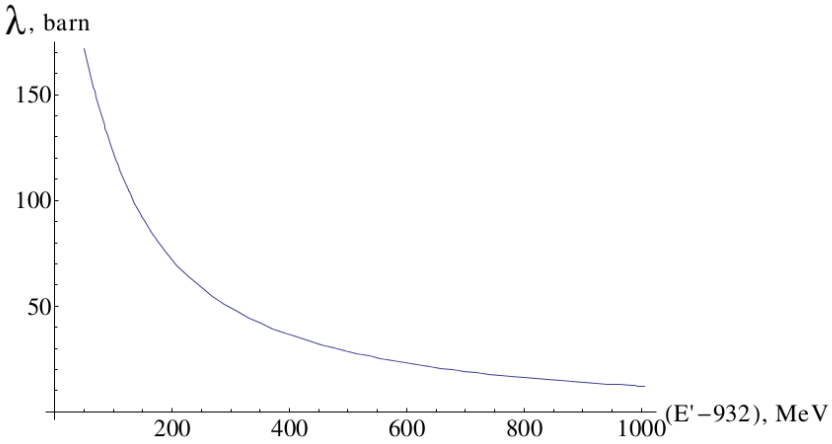

Figure 24.2 – The dependence of the λ coefficient on the incident proton energy for high proton energies.

§ 25 Coulomb cross section and the cross section of the 2-step process in a relativistic approach

One may apply the theoretical results of Ref. [131] for the description of the Coulomb excitation in the relativistic case. The equation of the Coulomb excitation rate is [131]:

$$R_{\text{Coulomb}} \equiv \Gamma_{\text{Coulomb}}/\Gamma_{tot} = \sigma_{\text{Coulomb}}/\sigma_{\text{Rutherford}}, \tag{25.1}$$

i.e. it is the ratio of the Coulomb excitation and Rutherford scattering cross sections, and

$$\sigma_{\text{Rutherford}} = \pi\rho_a^2, \tag{25.2}$$

$$\rho_a = \frac{200\gamma}{\omega[\text{MeV}]}\text{fm}, \tag{25.3}$$

$$\gamma = \frac{1}{\sqrt{1-v^2}}, \tag{25.4}$$

and in the case of EL nuclear excitation, the Coulomb cross section is

$$\sigma_{\text{Coulomb}} = \left(\frac{Z_{\text{projectile}}e^2}{\hbar c}\right)^2 \frac{B(EL)}{e^2R^{2L}}\pi R^2\eta(L), \tag{25.5}$$

where $\eta(L) = 2ln(\rho_a/R)$ for $L = 1$ and $\eta(L) = (L-1)^{-1}$ for $L \leq 1$. R is the radius of the target nucleus (e.g. $R = 1.2\,A^{1/3}$ fm for spherical nuclei such as Pb), and $B(EL)$ is the reduced transition probability. For instance, for the $E1$ nuclear transition we obtain the following values [116]:

$$\begin{aligned} B(E1, 0^+ \to 1^-) &= 6.288 \cdot 10^{-16}\omega^{-3}P_\gamma(E1, 0^+ \to 1^-) \\ &= 6.288 \cdot 10^{-16}\omega^{-3}3P_\gamma(E1, 1^- \to 0^+), \end{aligned} \tag{25.6}$$

where ω is the transition energy in units of MeV, and $P_\gamma(E1, 1^- \to 0^+) = \frac{1}{\hbar}\Gamma^\gamma$. Therefore, the width of Coulomb excitation, Γ_{Coulomb}, is proportional to the width of the corresponding

photo-excitation, Γ^{γ}, and it can be written in a similar way as in the non-relativistic case with the newly introduced coefficient X:

$$\Gamma_{\text{Coulomb}} = X\Gamma_{\text{tot}}\Gamma^{\gamma}. \tag{25.7}$$

Here, X depends on the energy and multipolarity of the nuclear transition to be excited. Then, the total cross section takes the same form as in the non-relativistic case, namely,

$$\sigma(E, E') = \lambda'(E', E)\frac{\Gamma_{bf}\Gamma_{tot}\Gamma^{\gamma}}{\Gamma_{tot}}\Lambda_{tot}(E), \tag{25.8}$$

with the new definition of the coefficient

$$\lambda'(E', E) = \frac{2\pi^2}{p_a^2}X. \tag{25.9}$$

The strength of this process is given again by:

$$S(E') = \lambda(E')\beta_{bf}(E')(\Gamma^{\gamma})^2. \tag{25.10}$$

For instance, for the nuclear transition presented in the previous Section one obtains at the incident proton energy $E' = 10$ GeV the following numerical value for the strength:

$$S = 2.7 \cdot 10^{-16}\,\text{barn} \cdot \text{MeV}. \tag{25.11}$$

This compares well to the non-relativistic value for the same proton energy, which is

$$S = 9 \cdot 10^{-15}\,\text{barn} \cdot \text{MeV}. \tag{25.12}$$

The comparison of the relativistic and non-relativistic results for the coefficient λ is presented in Fig. 25.1. One can observe here a similar behavior of these coefficients. The difference at high energies, however, is significant. Therefore, one should operate with both approximations to compare these theoretical results with future experimental investigations.

§ 26 Comparison to the non-resonant process

The described two-step process consisting of nuclear Coulomb excitation and bound-free pair conversion yields monochromatic positrons as an output. These monochromatic positrons represent a resonance on the background of positrons produced in the direct bound-free oder free-free pair production processes. Considering the bound-free pair production, one can calculate the relativistic value for the cross section at the resonance energy which can be obtained from Eq. 25.8. For instance, at the proton energy $E' = 10$ GeV this important quantity is

$$\sigma_{\text{res}} = 1.1 \cdot 10^{-10}\,\text{barn}. \tag{26.1}$$

It can be compared with the result of Ref. [132], where the authors received for the nonresonance pair production (i.e. pair production proceeding without the involvement of nuclear

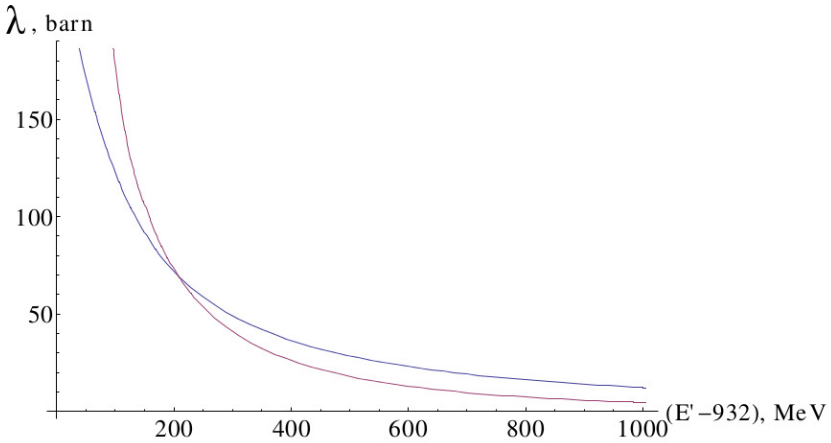

Figure 25.1 – The dependence of the λ coefficient on the incident proton energy in the relativistic (brown line) and non-relativistic (blue line) case.

excitation) at the positron energy $E_p = \omega - E_e^b$, corresponding to our nuclear excitation energy ω and the binding energy of the K-shell electron state E_e^b the approximate value

$$\frac{d\sigma_{\text{nonres}}}{dE_p} = 5.9 \cdot 10^{-3}\,\text{barn}/mc^2. \tag{26.2}$$

Therefore, one may conclude that at high outgoing positron energy resolution, e.g. at an energy resolution about $mc^2/10^6 = 0.5$ eV, the nuclear-resonant pair creation process gives a significant contribution, and, therefore, can be observed.

In summary, our theoretical results presented in the current Chapter show the possibility of the identification of nuclear-resonant pair creation in ion-ion collisions on the background of nonresonant pair production, which is going to be investigated in heavy ion scattering experiments at FAIR in the near future.

Chapter V

Pair creation in heavy ion channeling

§ 27 Introduction to pair creation in heavy ion channeling

The internal pair creation process has been investigated in the previous Chapters of this thesis. It has been considered as an alternative mechanism of electron-positron pair creation. In the present Chapter we discuss how this mechanism can be significantly improved by inducing pair creation in ion planar channeling through a crystal [see Fig. 27.1(a)]. In the reference frame of the traveling ions, the electromagnetic field of the periodic crystal structure may be regarded as a field of virtual photons with well-defined, equidistantly spaced discrete frequencies. For fast ions, these frequencies may extend into the MeV range, surpassing the pair creation threshold. In a direct channeling pair creation process, at all photon energies above this threshold value, a free-free or bound-free pair can be created; in the latter case, the electron is immediately captured into a bound state of the ion. In addition, when the virtual-photon frequency matches a nuclear transition in the channeling ion, a two-step resonant process may occur, in which first the nucleus is excited, then it decays by internal pair conversion. After multiple interfering periodic interactions of the channeling heavy ion with the crystal sites, pair creation occurs with significantly enhanced probability as compared to the collision of single ions, discussed in the previous Chapter. Pair creation with channeling ions may also be regarded as a feasible alternative to photo-production with an intense coherent gamma-ray source, which, however, does not exist yet.

Atomic and nuclear resonant excitations in axial channeling were firstly described by Okorokov [24, 133]. Recently, resonant coherent excitation (RCE) of the electron shell of ions was experimentally investigated [134–140], with ions as heavy as $^{238}U^{89+}$ [134] and transition energies as high as 6.7 keV [135]. These experiments are planned to be extended to the 100-keV $1s \rightarrow 2p$ electronic excitation of hydrogenlike $^{238}U^{91+}$ [134, 141], therefore, it is reasonable to anticipate that further developments will reach the MeV regime of pair creation. A general formalism for atomic excitations is presented in, e.g., Refs. [142–144], while in Refs. [145, 146], a framework suitable for describing nuclear excitation in channeling has been developed. Crystal-assisted pair creation by synchrotron radiation gamma photons has been theoretically formulated in [147]. In this process, only free leptons can be produced, thus one cannot exploit the advantage of resonances in the virtual-photon density of the crystal.

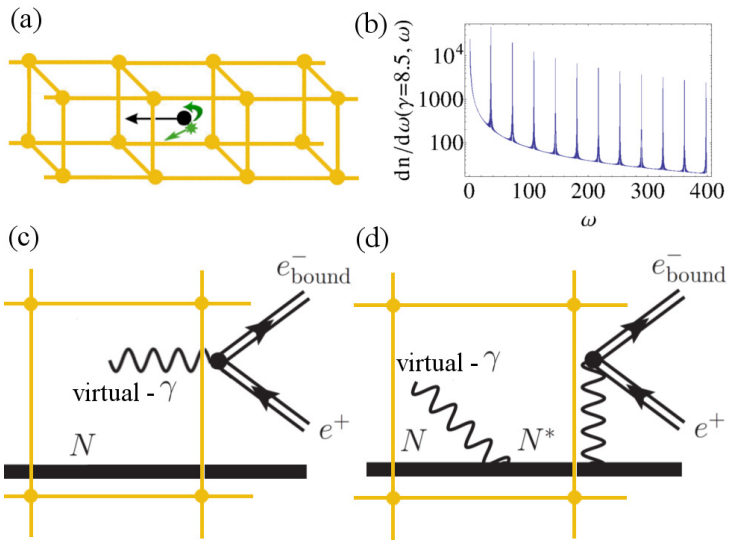

Figure 27.1 – (a) Schematic view of pair production in heavy ion channeling. (b) Typical virtual photon spectrum of the crystal, i.e. photon spectrum density $\frac{dn}{d\omega}$ as a function of the virtual photon frequency ω in units of keV. Diagrams for (c) direct pair creation by an equivalent photon and (d) pair production proceeding through nuclear excitation.

§ 28 Virtual photons in ion channeling

The two cases of direct and nuclear-resonant pair creation are schematically presented in Fig. 27.1(c) and (d), respectively. Electromagnetic processes in ion channeling can be described by the presence of virtual photons of the crystal field (see, e.g., [146]). The spectral density of virtual (equivalent) photons of frequency ω can be derived [145] by the help of the classical Weizsäcker-Williams method [148]. This approximation is valid in the ultrarelativistic case, i.e. when the Lorentz factor satisfies[1]

$$\gamma = \frac{1}{\sqrt{1-\frac{v^2}{c^2}}} \gg 10, \tag{28.1}$$

with v being the ion velocity and c the speed of light, and yields the spectral density

$$\frac{dn(\gamma,\omega)}{d\omega} = \frac{I_2(\omega)}{v\hbar\omega(2\pi)^4}\frac{\sin^2\left(\frac{\omega aN}{2\gamma v}\right)}{\sin^2\left(\frac{\omega a}{2\gamma v}\right)}e^{-\left(\frac{\omega\delta}{\gamma v}\right)^2} + \frac{I_2(\omega)}{v\hbar\omega(2\pi)^4}N\left(\frac{I_1(\omega)}{I_2(\omega)} - e^{-\left(\frac{\omega\delta}{\gamma v}\right)^2}\right). \tag{28.2}$$

Here, $\hbar$ stands for the reduced Planck constant, N is the number of atoms in a crystal channel, a denotes the lattice constant, and δ stands for the amplitude of thermal oscillations [145]. The integrals I_1 and I_2 are given by

$$\begin{aligned} I_1(\omega) &= \int d^2\vec{k}_\perp \vec{k}_\perp^2 V_{\vec{k}}^2, \\ I_2(\omega) &= \int d^2\vec{k}_\perp \vec{k}_\perp^2 V_{\vec{k}}^2 \exp^{-\vec{k}_\perp^2\delta^2}, \end{aligned} \tag{28.3}$$

[1] We note that in the present Chapter we use S.I. units in contrast to the previous Chapters of the thesis.

Table 29.1 – Cross sections (in barn) for the direct bound-free/free-free pair production by a bare ion with a charge Z, and γ corresponding to the energy ω' for $n = 6$ and $N = 100$. ω' (in MeV) is the maximum of the direct bound-free pair production cross section, following Ref. [22]. The notation $a[b]$ stands for $a \times 10^b$.

Z	ω'	γ	$\sigma_{\mathrm{PC}}^{\mathrm{chan}}$	$\sigma_{\mathrm{PC}}^{\mathrm{coll}}$	σ_{PC}
1	3.2	123	8.3[−6]/1.1[3]	8.3[−8]/1.2[1]	2.8[−10]/7.6[−10]
25	3.1	119	4.5[1]/7.0[5]	4.5[−1]/7.2[3]	1.3[−3]/3.4[−3]
50	3.1	119	1.0[3]/2.8[6]	1.0[1]/2.9[4]	2.6[−2]/6.8[−2]
75	1.5	59.3	4.9[3]/5.7[6]	4.9[1]/5.8[4]	1.7[−1]/7.5[−2]
92	1.5	59.3	1.3[4]/8.6[6]	1.3[2]/8.7[4]	4.6[−1]/2.1[−1]

with the 2-dimensional transverse wave vector $\vec{k}_\perp^2 = \vec{k}^2 - \left(\frac{\omega}{\gamma v}\right)^2$, and $V_{\vec{k}}$ being the Fourier transform of a single atom's potential in the crystal. It follows from Eq. (28.2) that at the energies $\omega_n = 2\pi n\gamma v/a$, $n \in [1, 2, 3, \dots]$, the virtual photon spectrum exhibits maxima proportional to N^2 [see Fig. 27.1(b)]. The photon energies ω_n can be experimentally tuned by choosing the proper γ of the ions. Due to restrictions caused by thermal vibrations of the lattice atoms, typically harmonics with $n < 10$ are used [149].

§ 29 Direct pair creation process

In this process, illustrated in Fig. 27.1(c), the outgoing positrons possess a continuous spectrum for free-free pair creation, and a monochromatic energy in the bound-free case. The cross section $\sigma_{\mathrm{PC}}^{\mathrm{chan}}$ of pair creation via channeling following [145] is defined as the convolution of the virtual photon density with the cross section σ_{PC} of pair creation by a real photon:

$$\sigma_{\mathrm{PC}}^{\mathrm{chan}}(\gamma) = \int d\omega \sigma_{\mathrm{PC}}(\omega) \frac{dn(\gamma, \omega)}{d\omega}\,, \tag{29.1}$$

where $\sigma_{\mathrm{PC}}(\omega)$ can either represent the cross section of bound-free (bf) or free-free (ff) pair creation by a real photon of frequency ω. The number of pairs created in unit time can be expressed as $\dot{N}_{\mathrm{PC}}^{\mathrm{chan}} = S\Phi\sigma_{\mathrm{PC}}^{\mathrm{chan}}/a^2$, with S being the cross sectional area of the ion beam and Φ its flux. The cross section for bound-free pair creation in the Coulomb nuclear field by an external photon is [22]

$$\sigma_{\mathrm{PC,bf}}(\omega) = \frac{2\pi^2\alpha\lambda_C^2}{\omega} \sum_\lambda \sum_{JLMM_{\mathrm{b}}} \left|\mathcal{M}_{\lambda JLMM_{\mathrm{b}}}(\omega)\right|^2\,, \tag{29.2}$$

where α is the fine-structure constant, λ_C denotes the electrons Compton wavelength, $\lambda = \pm 1$ is the helicity of the photon, M_{b} is the magnetic quantum number of the created bound electron, and the quantum numbers J, L and M correspond to the partial waves of the free-positron wave function. The matrix element is given as [22]

$$\mathcal{M}_{\lambda JLMM_{\mathrm{b}}}(\omega) = \int d\vec{r}\psi_b^*(\vec{r})\left[\vec{\alpha}\cdot\vec{e}_\lambda\right] e^{i\omega r}\psi_{JLM}(\vec{r})\,, \tag{29.3}$$

where ψ_{JLM} is the positron partial wave in the Coulomb field of the nucleus, $\psi_{\rm b}$ is the bound-electron wave function, and $\vec{\alpha}$ is the 3-vector of alpha matrices [65]. Formulas for free-free pair creation may be similarly derived, involving an additional summation over the partial waves of the free electron. This approach, neglecting the interaction of the created particles with the periodic field, can be employed because, for the high frequencies present here, the classical nonlinearity parameter $\xi_0 = \frac{eE}{m\omega}$ [43], written in terms of the crystals electric field strength E in the framework of the ion and the unit charge e, is much less than unity. $\sigma_{\rm PC,bf}$ has an energy threshold at $2mc^2 - E_{\rm b}$, with $E_{\rm b}$ being the binding energy of the created electron. After this threshold, $\sigma_{\rm PC,bf}$ increases with energy up to a given maximal value, whose position and value depend on the nuclear charge. This behavior is analogous to the energy dependence of the bound-free pair conversion coefficient $\beta_{\rm bf}$, as shown in Fig. 8.1.

In Tab. 29.1 the cross-section values are presented for direct pair creation for different charges Z of the ion channeling in an Au crystal, at energy ω', corresponding to the maximum of the direct bound-free pair creation cross section. It is choosen to match the energy of the 6th harmonic of the virtual photon density (28.2). The advantage of using heavy ions is justified by the following scaling low: the cross section $\sigma_{\rm PC}$ scales with the charge number as $\approx Z^{5-\epsilon}$, $0 \leq \epsilon \leq 1$ [22], and the Z-scaling of $\sigma_{\rm PC}^{\rm chan}$ is given by that of $\sigma_{\rm PC}$ [see Eq. (29.1)]. At high virtual photon energies, the pair creation cross section decreases and vanishes asymptotically. The cross section $\sigma_{\rm PC}^{\rm chan}$ is compared to the cross section $\sigma_{\rm PC}^{\rm coll}$ of the pair creation in the single Coulomb collision process (estimated from the channeling cross section with the substitution of $N = 1$), and with the cross section $\sigma_{\rm PC}$ of pair photo-production in the nuclear Coulomb field [22]. In both cases, one can see a significant increase. The cross sections can be translated to pair creation rates, assuming e.g. an ion beam cross section of $S = 1$ cm^2 and flux $\Phi = 10^{10}/(\text{cm}^2\text{s})$, yielding $\dot{N}_{\rm PC,bf}^{\rm chan}$ =600/s, 2900/s and 7800/s, for Z =50, 75 and 92, respectively.

A ratio $R(\gamma)$ of the cross section of the coherent interaction with N atoms to the incoherent one can be defined as follows: $R(\gamma) = \sigma_{\rm PC}^{\rm chan}(\gamma)/\left(N\sigma_{\rm PC}^{\rm coll}(\gamma)\right)$. This parameter measures the coherence in the channeling process. For the cases shown in Tab. 29.1, R is practically equal to unity, showing that there is no enhancement due to coherence for direct pair creation via channeling. This is explained by the broadness of the continuous spectrum of photons which can create a pair, as compared to the width $2\gamma v/(aN)$ of a photon density peak. In other words, the coherence length of photo-production is much shorter than the Lorentz-contracted crystal length aN/γ.

High ion kinetic energies are needed to meet the resonance conditions for the virtual-photon energies required for direct pair creation by ion channeling. Such energies can be reached, for instance, by the projected FAIR accelerators [23] or in the Large Hadron Collider [150]. Laser-accelerated ion beams, anticipated to eventually reach the GeV regime [151, 152], may also provide a viable alternative in future. One possible way to reduce the required ion kinetic energy is to use higher crystal-field harmonics. This may be more feasible at high ion energies than at the low energies of the RCE experiments performed thus far [134–140], because fast ions interact less with the crystal electrons, suppressing decoherence.

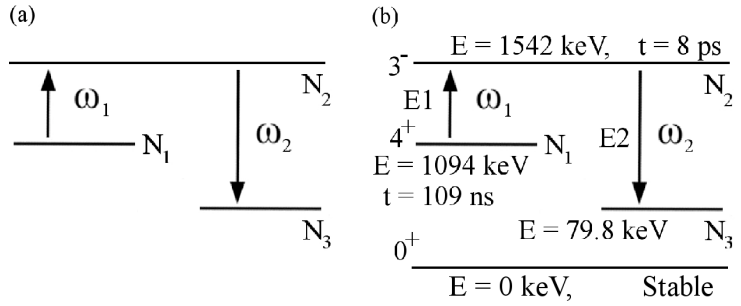

Figure 30.1 – (a) The preferred 3-level scheme and (b) the level scheme for one of the possible elements, ^{168}Er. The nuclear data are taken from Ref. [75].

§ 30 Pair creation proceeding via nuclear resonances

The cross section of the first step of the process shown on Fig. 27.1(d), namely, the RCE of the nucleus passing through the crystal, can be given as [145, 146]

$$\sigma_{\rm N}^{\rm chan}(\gamma) = \int d\omega \sigma_{\rm N}(\omega) \frac{dn(\gamma,\omega)}{d\omega}\,, \tag{30.1}$$

with the cross section of nuclear excitation with a real photon of frequency ω,

$$\sigma_{\rm N}(\omega) = g\frac{\pi c^2}{\omega_0^2}\frac{\Gamma_{\rm rad}^2}{(\omega-\omega_0)^2+\Gamma^2/4}\,, \tag{30.2}$$

where ω_0 is the nuclear excitation energy. The statistical factor $g = (2I_f+1)(2I_i+1)$ depends on the angular momenta I_i (I_f) of the initial (final) nuclear states, Γ is the total width of the excited nuclear level, and $\Gamma_{\rm rad}$ is its radiative width. To obtain the cross section for the total two-step process of ion excitation–deexcitation by pair creation, $\sigma_{\rm N}^{\rm chan}$ is multiplied by the coefficient of pair conversion. This coefficient $\beta_{\rm bf}$ is introduced in Chapter I for the bound-free case to be the ratio of the transition probabilities of pair creation and radiative decay: $\beta_{\rm bf} = P_{\rm bf}/P_{\rm rad}$. In dependence of the corresponding nuclear transition multipolarity (i.e., the angular momentum L' and parity of the transition), the following expressions can be obtained for this quantity:

$$\begin{aligned}
\beta_{\rm bf}(EL') &= \sum_{\kappa\kappa'} \frac{4\pi\alpha\omega}{L'(L'+1)} s|\kappa\kappa'\|(\kappa-\kappa')(R_3+R_4) + L'(R_1+R_2+R_3-R_4)|^2\,, \qquad (30.3)\\
\beta_{\rm bf}(ML') &= \sum_{\kappa\kappa'} \frac{4\pi\alpha\omega}{L'(L'+1)} s|\kappa\kappa'\|(\kappa+\kappa')(R_3+R_4)|^2\,,
\end{aligned}$$

where s is introduced in terms of a $3j$-symbol

$$s = \begin{pmatrix} j & j' & L \\ \frac{1}{2} & -\frac{1}{2} & 0 \end{pmatrix}^2 . \tag{30.4}$$

Here, again, κ and κ' are Dirac angular momentum quantum numbers. The radial integrals $R_1,\ldots,R_6$ are defined in Appendix A with the analytical form of the fermionic Coulomb wave functions for bound and free particles. All results are obtained for the $1s$ electron orbital having

Table 30.1 – Nuclear data [75] for different elements corresponding to the level scheme introduced at Fig. 30.1(a). Energies are given in units of keV.

	^{168}Er	^{72}Ge	^{115}Sn
E_{N_1}	1094	691.4	612.8
E_{N_2}	1542	1464	1416.9
E_{N_3}	79.8	0	0
ω_1	447.6	772.6	807.1
ω_2	1462	1464	1416.9
τ_1	109 ns	444 ns	3.26 μs
Γ (meV)	0.082	0.15	1.88
$\rho_{N_2\to N_3}$	0.0058	0.124	0.739
$\beta^{\mathrm{bf}}_{N_2\to N_3}\cdot 10^4$	9.3	0.55	2.0
$\beta^{\mathrm{ff}}_{N_2\to N_3}\cdot 10^4$	0.77	0.74	0.52

a maximal overlap with the nucleus. Equation (30.3) can be adopted to the free-free case (β_{ff}) in a straightforward manner.

The cross section of the two-step nuclear excitation-pair conversion (NEPC) process for channeling ions can be written as

$$\sigma^{\mathrm{chan}}_{\mathrm{NEPC}}(\gamma) = \sigma^{\mathrm{chan}}_{\mathrm{N}}(\gamma) B\beta\,, \tag{30.5}$$

where B is the branching ratio of the gamma decay corresponding to the pair creation transition, and $\beta = \beta_{\mathrm{bf}}$ or β_{ff}. One can see in Eq. (30.5) that the cross section for the excitation $\sigma^{\mathrm{chan}}_{\mathrm{N}}$ and the rate for the deexcitation β are independent and, in principle, may correspond to different transitions to/from some excited nuclear state N_2. The total cross section can be rewritten as

$$\sigma^{\mathrm{chan}}_{\mathrm{NEPC}}(\omega_1^{N_1\to N_2}, \omega_2^{N_2\to N_3}) = \sigma^{\mathrm{chan}}_{\mathrm{N}}(\omega_1^{N_1\to N_2}) B^{N_2\to N_3}\beta(\omega_2^{N_2\to N_3})\,. \tag{30.6}$$

The levels N_1, N_2 and N_3 are depicted on the three-level scheme of Fig. 30.1(a). The energy $\omega_2^{N_2\to N_3}$ has to exceed the bound-free pair creation threshold $2mc^2 - E_{e^-_{\mathrm{bound}}}$. The excitation energy $\omega_1^{N_1\to N_2}$ is not restricted, and from an experimental point of view it is preferable to utilize a transition with a lower energy. It is more advantageous for level N_1 to be metastable, in order to be able to prepare the nuclei in this state before injecting them into the crystal. One of the possible elements is ^{168}Er, with its level scheme shown in Fig. 30.1(b). Results for the pair conversion coefficients β for this isotope, together with data for other potentially suitable elements, ^{72}Ge and ^{115}Sn, are given in Tab. 30.1.

Once the nuclear transitions involved and the type of crystal are fixed, the only variable parameters are the thickness of the crystal determined by N, and the harmonic order n. The dependence of the ion kinetic energy, connected with γ, and of the excitation cross section $\sigma^{\mathrm{chan}}_{\mathrm{N}}$ on n at certain value of N is presented in Tab. 30.2. The largest cross section is reached at the fundamental frequency, however, the cross section decreases slowly with increasing n, therefore, it is again preferable to tune the Lorentz factor γ to higher harmonics. Values of the coherent enhancement factor R are also given in Tab. 30.2. $R(\gamma)$ only weakly depends on the element and the transition, and is mostly influenced by the harmonic order n, and by N. The

Table 30.2 – The dependence of the ion's γ factor and the excitation cross section σ_N^{chan} (in barn) on the harmonic order n at certain value of $N = 100$ for different ω_1. The last column gives the ratio R, depending on n only and not on the atomic properties for all narrow transitions (i.e. those with a line width below the bandwidth of the virtual photon spectrum).

	^{168}Er		^{72}Ge		^{115}Sn		
ω_1=	447.6 keV		772.6 keV		807.1 keV		
n	γ	σ_N^{chan}	γ	σ_N^{chan}	γ	σ_N^{chan}	R
1	104	8.2	180	0.023	188	1.8	69
2	52	7.2	90	0.020	94	1.6	66
4	26	6.2	45	0.018	47	1.3	63
6	17	5.7	30	0.016	31	1.2	61
8	13	5.3	22	0.015	23	1.1	59
10	10	5.0	18	0.014	19	1.1	57

dependence of R on γ is shown in Fig. 31.1 for the case of the 447.6-keV transition in ^{168}Er. The figure shows that, for a crystal as thin as 1000 atoms, which is the typical order of magnitude used in experiments [134], one can achieve a coherent pair creation enhancement by 3 orders of magnitude. By the help of high-energy ion beams (up to 33 GeV/u or γ=35) provided by the FAIR facility in the near future [23], one can investigate all elements in Tab. 30.2.

The first two lines of the Tab. 31.1 demonstrate the behavior of the nuclear excitation cross section σ_N^{chan} on N, the number of ion sites along the channel. One can observe a significant – quadratic – enhancement of the cross section with increase of N. Employing a thicker crystal with higher N is experimentally limited by restrictions due to deviations from a straight ion trajectory in the crystal. One may perform more realistic Monte-Carlo simulations to model the ion trajectories, if it is necessary to increase the crystal thickness even further. The total cross section of the two-step process NEPC can be calculated by Eq. (30.6), using data from Tables 30.1 and 30.2. In Tab. 31.1 (last 4 rows) results are presented for this cross section for different thicknesses of the crystal (N = 100, 1000) with a fixed harmonic number (n = 6). The rate of created pairs is also proportional to N^2.

§ 31 Discussion

We found that direct pair creation and pair creation via nuclear excitation in heavy ion collisions can be significantly enhanced by multiple periodic collisions in a crystal channeling experiment. The direct process is associated with high creation rates increasing approximately linearly with the number of crystal sites in the channel. As for pair creation proceeding via nuclear resonances, which typically have lower probabilities, the coherent nature of the excitation process yields a quadratic scaling with the number of collisions, resulting in observable pair creation rates. These studies complement the investigation of pair creation by different strong electromagnetic fields such as optical or X-ray lasers [25]. The ion kinetic energies required for such investigations can be reached by present and upcoming experimental facilities, such as, e.g., FAIR. Laser-accelerated ions may also be considered in future for such studies.

Table 31.1 – The cross section (in barn) of bound-free and free-free pair creation via nuclear resonances and the coherence parameter R, for different crystal thicknesses (N = 100, 1000) with a fixed harmonic order (n = 6). $a[b]$ stands for $a \times 10^b$.

	N	^{168}Er	^{72}Ge	^{115}Sn
σ_{N}	100	5.7[0]	1.6[-2]	1.2[0]
	1000	5.6[2]	1.6[0]	1.2[2]
$R(\gamma)$	100	60.5	60.6	60.5
	1000	601	604	602
$\sigma_{tot}^{\mathrm{bf}}$	100	3.1[-5]	1.1[-7]	1.8[-4]
	1000	3.0[-3]	1.1[-5]	1.8[-2]
$\sigma_{tot}^{\mathrm{ff}}$	100	2.5[-6]	1.4[-7]	4.7[-5]
	1000	2.5[-4]	1.4[-5]	4.6[-3]

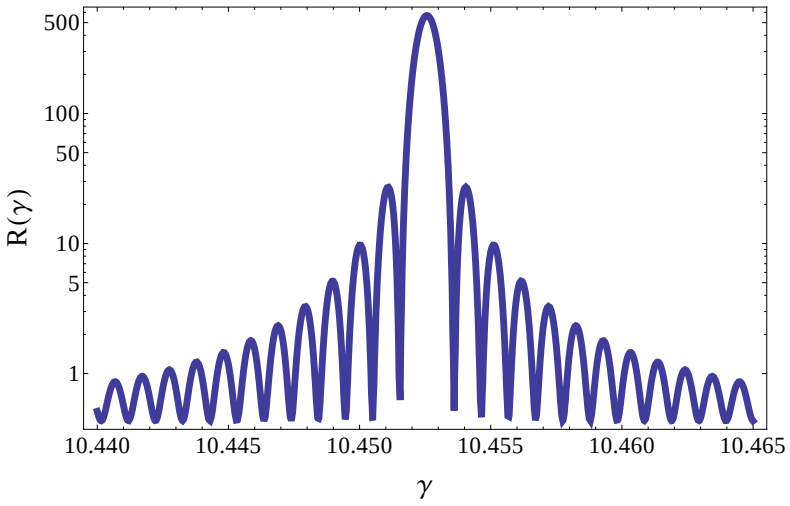

Figure 31.1 – The coherence parameter $R(\gamma)$ for the case of 447.6-keV transition in an ^{168}Er nucleus. Here, N=1000, and n=10.

Chapter VI

Parity violation in unconventional superconductors

§ 32 Introduction to parity violation in unconventional superconductors

The electroweak theory, combining two fundamental interactions – the electromagnetic and weak forces – was introduced by Salam, Glashow and Weinberg in the 1960s [153–155]. It explains the nuclear beta-decay and weak effects in high-energy physics. One of the most prominent properties of the electroweak theory is the spatial parity violation (PV). This unique phenomenon distinguishes the weak interaction from the electromagnetic one, therefore, it helps to investigate weak properties on an electromagnetic background. Firstly, PV was experimentally detected in the beta decay of ^{60}Co by Wu [19] and collaborators. Later, many other novel experiments for the PV observation have been proposed and performed. Low-energy PV experiments in atomic physics were carried out with Cs atoms (see e.g. [20, 156, 157]). The PV effect has been theoretically predicted to have a measurable influence on the vibrational spectrum of molecules in Ref. [158]. Investigations of PV effects enable tests of the standard model of elementary particle physics and impose constraints on physics beyond this model. The search for new efficient ways to re-examine and investigate the PV phenomenon is an ongoing research activity (see, for instance, [159–162]).

Another physical situation where PV effects can play a noticeable role is the interaction of electrons with the crystal lattice of nuclei in the solid state [21, 163]. While the relative contribution of the PV effect is lower in comparison to other investigation methods, PV experiments with solids are of interest because of the compact size of the experimental equipment. Possible solid-state systems where one may study the PV contribution are superconductors (SC). Such systems would enable to study the macroscopic manifestation of a quantum effect such as the electroweak interaction. The idea that PV effects can appear in SCs has been suggested by Vainstein and Khriplovich [21]. They have realized that the electroweak contribution is immeasurably small in conventional s-wave SCs. However, it was predicted [164], that the effect can be increased by using SCs of other types, e.g. p-wave SCs. Nowadays different unconventional SCs can be created and are well understood (see, e.g. [165]). Therefore, in the present study this effect is estimated to be observable in p-wave ferromagnetic SCs. Furthermore, a novel

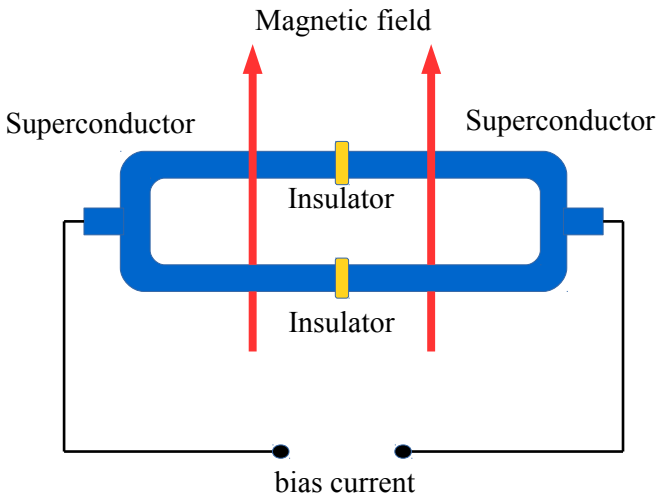

Figure 32.1 – Circular Josephson junction with two insulations, placed into a magnetic field.

method is put forward for the observation and control of the effect. The calculations presented in this Chapter yield a relative contribution of PV enhanced by several orders of magnitude as compared to the *s*-wave case, and open a way for a further improvement and experimental observation of the effect.

The SC system for studying PV considered for these purposes is a circular Josephson junction in an external magnetic field. This system is described, e.g., in Ref. [166] and consists of a circular SC with two insulating junctions (see Fig. 32.1). If the circular Josephson junction is placed in an external magnetic field, the maximal value of the SC current depends periodically on the magnetic flux through the ring. This dependence is symmetric under the reflection of the direction of the magnetic flux. However, the presence of the PV terms in the electron-nucleus interaction breaks this symmetry. This effect is investigated in the case of unconventional *p*-wave SCs.

This Chapter is organized as follows. § 33 contains the description of the PV effect in solid state, and discusses a possible superconducting system, namely, a circular Josephson junction. In § 34, a method for the possible observation and control of the PV effect is developed, and the magnitude of the PV effect for a certain SC, namely, uranium digermanide, UGe_2, is evaluated. § 35 discusses a scheme for the further improvement of the measurement technique, which can lead to a significant enhancement of the effect. Finally, a quantitative prediction of the PV effect in the considered system is provided in § 36.

§ 33 Parity violation in superconductors

Weak odd-parity interaction in superconductors

The weak odd-parity interaction in a crystal is given by the operator [21]

$$W(\vec{r}) = \frac{G}{\sqrt{2}m}\sum_i \left(Zq\vec{\sigma}\vec{p}\delta(\vec{r}-\vec{R}_i) + \kappa_I \vec{I}_i \vec{p}\delta(\vec{r}-\vec{R}_i) + i\kappa_I[\vec{I}_i \times \vec{\sigma}]\vec{p}\delta(\vec{r}-\vec{R}_i)\right), \tag{33.1}$$

where G is the Fermi constant [167], Z is the nuclear charge of crystal ions, m stands for the electron mass, q is the weak charge, and $\vec{p}$ denotes the 3-momentum of a Cooper pair. Furthermore, I_i stands for the nuclear spin, κ_I is the pre-factor of the weak interaction of electrons with nuclear spins [21]. The summation goes over the crystal sites, determined by the position vectors $\vec{R}_i$. It is obvious from this equation that if the pair spin is zero, $\sigma = 0$ (s- or d-wave), only the second term is non-vanishing. This case has been investigated before in Ref. [164]. In the p-wave case [168], the first term is also nonzero, and its approximate magnitude is Z-times larger than that of the other terms.

Now, the case of interest ($\sigma = 1$) is described in analogy to the $\sigma = 0$ case [164]. The first term of the effective interaction is [164]

$$W_{\text{eff}}^{(1)} = \frac{GZ^3 qR}{\sqrt{2}}\frac{N}{m}\vec{\sigma}\vec{p}, \tag{33.2}$$

where the weak charge is

$$q = \kappa_{1p} + \frac{A-Z}{Z}\kappa_{1n}, \tag{33.3}$$

expressed with the factors $\kappa_{1p} = \frac{1}{2}(1 - 4\sin^2\theta_{\text{C}})$ and $\kappa_{1n} = -\frac{1}{2}$, where the Cabibbo weak mixing angle [169] is given by $\sin^2\theta_{\text{C}} = 0.22529$. In the above equation, N and A are the density and mass number of nuclei, respectively, and

$$R = 4\left(\frac{a_{\text{B}}}{2ZR_0}\right)^{2-2\gamma} \Big/ \Gamma^2(2\gamma+1) \tag{33.4}$$

is the enhancement factor of relativistic effects at small distances [164], where $\gamma = \sqrt{1-\alpha^2Z^2/2}$, $R_0 \approx 1.2 \cdot A^{1/3}$ fm is the nuclear radius, a_{B} denotes the Bohr radius, and Γ denotes the gamma function of real argument. R is on the order of 10 for heavy elements. The effective term (33.2) has to be added to the standard electromagnetic Lagrangian:

$$L = -m\sqrt{1-v^2} + e\vec{A}\vec{v} - e\phi - W_{\text{eff}}^{(1)}, \tag{33.5}$$

where relativistic units are used. For the canonical momentum of an electron one obtains

$$\vec{P} = \frac{\partial L}{\partial \vec{v}} = \frac{m\vec{v}}{\sqrt{1-v^2}} + e\vec{A} - \frac{GZ^3 qRN}{\sqrt{2}2m}2m^*\vec{\sigma}, \tag{33.6}$$

where m^* is the effective mass of the electron. The mass ratio $\frac{m^*}{m}$ can exceed 10^2. The above weak modification of the electron momentum is equivalent to the substitution

$$e\vec{A} \to e\vec{A} - \frac{GZ^3 qRN}{\sqrt{2}}\frac{m^*}{m}\vec{\sigma}, \tag{33.7}$$

to be performed in all equations. This substitution is applied in the theoretical description of a superconducting ring.

Considering the case when the external magnetic field does not penetrate into the SC, one can obtain the following expression for the magnetic flux in the superconducting ring:

$$2e\Phi \to 2e\Phi - f, \tag{33.8}$$

with $\Phi = \oint d\vec{r}\vec{A}$ and

$$f = \sqrt{2}GZ^3 qRN\frac{m^*}{m}\oint d\vec{r}\vec{\sigma}. \tag{33.9}$$

This result can be used in any applications and for any SC systems. In the following Section this is applied for the circular Josephson junction. Let us discuss now the loop integral in Eq. 33.9. In the case of p-waves, the pairing spin is $\sigma = 1$. However, the integral

$$\oint d\vec{r}\vec{\sigma}(\vec{r}) \tag{33.10}$$

is non-zero only if the mean spin vector (averaged over the whole SC loop) is non-zero. Therefore, it is advisable to use an unconventional SC, which possesses a superconducting phase in coexistence with the ferromagnetic phase. This allows to control the effect by inducing magnetization in the SC. Furthermore, because of the Z^3 scaling of the weak flux f, it is advantageous to employ heavy-element SCs. A possible material with these properties is uranium digermanide, UGe_2 [170–172].

Circular Josephson junction

The suggested experimental setup for the observation of the PV effect in SC is a circular Josephson junction (JJ). A linear JJ is created by two SCs, separated by a thin insulator material. It was predicted by Josephson [173] that the insulator does not prevent the appearance of a superconducting current, however, the properties of the current depend on the thickness and material of this insulator. Nowadays JJs, being able to detect rather weak magnetic fields, have a wide spectrum of applications connected with atomic physics measurements and quantum optics [174]. In the following the point-contact limit of the JJ is considered, i.e. the insulator is assumed to be infinitely thin. However, all derivations presented here can be easily extended for other JJ models, since the PV effect breaks the symmetry in any case.

The current in the JJ in the point-contact approximation is given by the expression [175]

$$J(\phi) = J_0\Delta\frac{\tanh\left(\frac{\Delta}{2\pi}\sqrt{1 - D\sin^2(\phi/2)}\right)}{\sqrt{1 - D\sin^2(\phi/2)}}\sin\phi\,, \tag{33.11}$$

where D is the angle-averaged transmission probability, and Δ stands for the gap parameter. The phase is defined by

$$\phi = \delta_0 + 2e\int Ads\,, \tag{33.12}$$

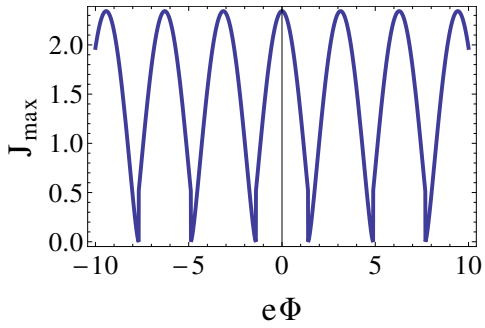

Figure 33.1 – The dependence of the maximal current $J_{\max}$ (in units of J_0) on the magnetic flux $e\Phi$ (in units of $\hbar$), with values $\Delta = 100$ and $D = 0.5$. $J_{\max}$ is calculated according to Eq. (33.14). Both energy and temperature are measured in units of Kelvin.

where the integral is to be taken across the junction [166] and δ_0 is an unknown constant phase. This expression is valid both in the clean and dirty limits of the SC.

If one now constructs a circular JJ by two identical JJ, junction a and junction b connected in parallel (see Fig. 32.1), only the following phase difference between these junctions is observable:

$$\delta_b - \delta_a = 2e \oint A ds \,, \tag{33.13}$$

where the circular integral is to be taken along the loop, and thus $\delta_b - \delta_a = 2e\Phi$. As noted above, one can only control the phase difference, thus one can write, following Ref. [166]: $\delta_a = \delta_0 + e\Phi$ and $\delta_a = \delta_0 - e\Phi$. The total current in the circular JJ as a function of the magnetic flux is then given by the expression

$$\begin{aligned} J_{\rm tot}(\Phi) &= J_0\Delta\left[\frac{\tanh\left(\frac{\Delta}{2\pi}\sqrt{1 - D\sin^2((\delta_0 + e\Phi)/2)}\right)}{\sqrt{1 - D\sin^2((\delta_0 + e\Phi)/2)}}\sin(\delta_0 + e\Phi)\right. \\ &+ \left.\frac{\tanh\left(\frac{\Delta}{2\pi}\sqrt{1 - D\sin^2((\delta_0 - e\Phi)/2)}\right)}{\sqrt{1 - D\sin^2((\delta_0 - e\Phi)/2)}}\sin(\delta_0 - e\Phi)\right]. \end{aligned} \tag{33.14}$$

This expression still depends on the arbitrary phase δ_0. However, it is possible to determine the maximal value of the current $J_{\max}$. The behavior of the maximal current can be calculated numerically for a certain gap parameter Δ and a diffusion parameter D. The dependence of $J_{\max}$ on $e\Phi$ is shown in Fig. 33.1 for the values $\Delta = 100$ (in units of temperature) and $D = 0.5$.

The dependence of $J_{\max}$ on Φ is invariant under the change of the sign of Φ. Due to the presence of the weak odd-parity interaction, as shown in the previous Section, one has to substitute Φ in all equations as

$$2e\Phi \to 2e\Phi - f \,, \tag{33.15}$$

where f is the positive admixture of the weak parity-violating term. Thus the real dependence of the maximal current on the magnetic flux is given by

$$J^{\rm real}_{\max}(\Phi) = J_{\max}(e\Phi - f/2) \,, \tag{33.16}$$

and it is not symmetric with respect to the change of the sign of Φ. The main purpose of this Chapter is to present the case in which this asymmetry can be measured. In the following

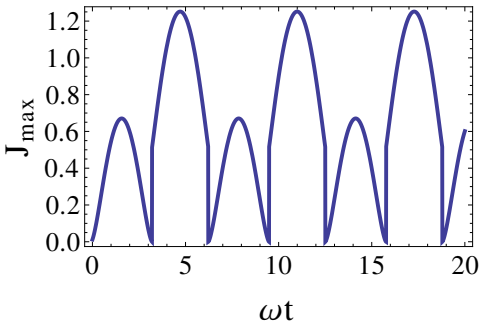

Figure 34.1 – The periodic dependence $J_{\max}(\omega t)$ without the inclusion of the weak interaction.

Sections the calculations will be discussed and a possible measurement method for determining the value of f will be presented.

§ 34 Possible method for the measurement of the f-parameter

Measurement method employing a time-periodic magnetic field

It can be challenging to directly observe the small asymmetry of the dependence of $J_{\max}^{\text{real}}$ on $e\Phi$, therefore, one may suggest to employ a time-periodic magnetic field instead of a static one. As mentioned before, it is possible to calculate the phase-independent maximal Josephson current $J_{\max}(e\Phi)$. Let $e\Phi_0$ be the first positive root of this expression. If one now introduces a periodic component to the magnetic field,

$$e\Phi(t) = e\Phi_0 + \frac{a}{2}\sin\omega t\,, \tag{34.1}$$

$J_{\max}(\omega t)$ also depends periodically on time with the period $T = 2\pi/\omega$, where ω is the angular frequency of the oscillating field. Roots of this function are reached every half of the period, i.e. with a π/ω periodicity. The typical shape of this function, calculated for the case of $J_{\max}(e\Phi)$ shown on Fig. 33.1, is presented on Fig. 34.1.

Let us now incorporate the weak interaction into this system. The weak interaction can be controlled (”switched on/off”) by introducing the magnetization in the SC ferromagnetic circular JJ, since the PV contribution is proportional to the average spin of the Cooper pairs [see the integral of the spin over a circle in Eq. (33.9)]. The periodic field coefficient a is chosen to be greater than the weak factor f, however, it is comparable to it: $a = xf$, $x \gtrapprox 1$.

Now the roots of $J_{\max}(\omega t)$ are not exactly π/ω-periodic any more. This behavior is shown on Fig. 34.2. Furthermore, in the limit $x \to 1$, the roots become almost $2\pi/\omega$ - periodic. This non-periodic behavior of roots can be observed experimentally, since it can be dynamically controlled by the periodic magnetic field.

As an alternative, one may also do the measurement at some certain phase δ_0 rather than at a maximal Josephson current. Here one can introduce again the oscillations of the magnetic field around the first root $e\Phi_0$ of the total current $J_{\text{tot}}(\delta_0, e\Phi)$. In this case, the current changes its sign during the total period $T = 2\pi/\omega$. If one takes $a = f$ after switching on the weak interaction, with magnetization being present in the SC, the total current function will be always of the same sign, as it is shown on Fig. 34.3.

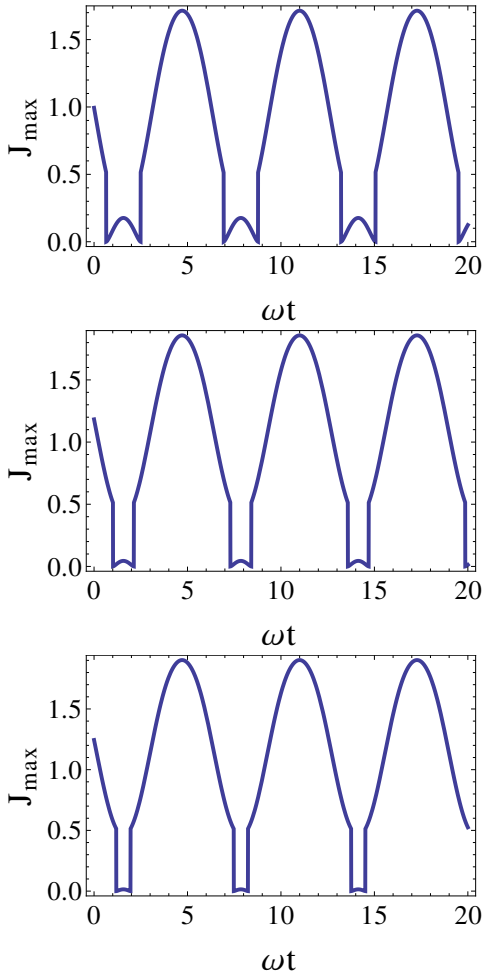

Figure 34.2 – The periodic dependence $J_{\max}(\omega t)$ with the weak interaction included, for the parameters $a = xf$, x =1.5, 1.1, 1.01, respectively.

Estimation of the effect

In the present Section the value of the admixture f to the magnetic flux through the JJ ring is evaluated [see Eqs. (33.8), (33.9)] to provide a realible estimate of the magnitude of the PV effect in SCs.

In the case of a ferromagnetic SC one can assume that pairs are polarized along the loop, therefore, their polarization can have two different opposite directions. This assumption yields for the loop integral

$$\oint d\vec{r}\vec{\sigma}(\vec{r}) = \eta \oint dr\,, \tag{34.2}$$

with the mean spin value η, which has to be determined by a self-consistent solution of the equations for superconductivity and ferromagnetism in this material. This is performed in Appendix C.

In the following part of the present Section an estimation of the PV effect is presented. The

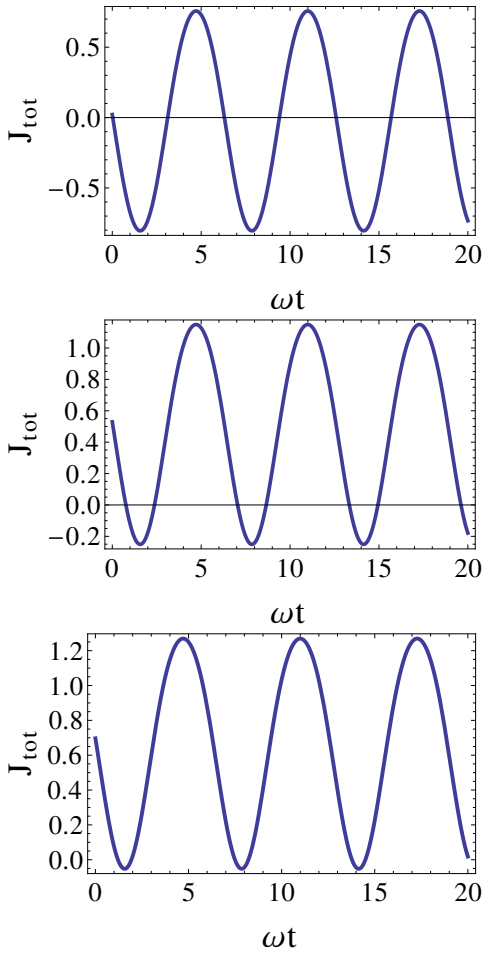

Figure 34.3 – The periodic dependence $J_{\rm tot}(\delta_0, \omega t)$. The first plot shows the case when the weak interaction is not included, and the next two plots are for the case when the weak interaction is included, with the parameters $a = xf$, $x = 1.5,\ 1.1$, respectively.

PV admixture f is expressed with the mean spin η as

$$f = \sqrt{2} G Z^3 R q N \frac{m^*}{m} \eta \oint dr\,. \tag{34.3}$$

Assuming a round JJ, the loop integral simply yields $\oint dr = 2\pi L$, the mean spin value η is to be calculated in the next Section, and the remaining factors are known: $\frac{G}{\pi\alpha^3} = 10^{-13}$, $Z = 92$. The relativistic enhancement parameter is $R \approx 11$, the value of the effective mass at the ambient pressure is in the interval [176] $\frac{m^*}{m} = 2.3 \ldots 25$, thus one may assume $\frac{m^*}{m} = 25$. The density of nuclei is [177, 178] $N = 0.25 \cdot 10^8$ cm^{-1}. Then the final value of f is

$$f = 2\pi \cdot 6.9 \cdot 10^{-4} L\eta, \tag{34.4}$$

where the length L is measured in units of cm. This result is 3 orders of magnitude larger than the value of the admixture factor in the case of an s-wave heavy SC [164]. To observe this effect one may use the method with the oscillating magnetic field, as described in the previous Section.

Since the flux, in units of $\hbar$, is given by

$$e\Phi = \frac{e\pi L^2}{\hbar} B\,, \tag{34.5}$$

the time-dependent part of the magnetic field is

$$e\Phi_0 + \frac{a}{2}\sin t = \frac{e\pi L^2}{\hbar}(B_0 + B_t \sin t)\,. \tag{34.6}$$

In case of $a \gtrapprox f$, the expression for the amplitude B_t, in units of Tesla is [cf. Eq. (33.15)]

$$0.152 \cdot 10^{20} L^2 B_t \gtrapprox \frac{f}{2}, \tag{34.7}$$

where L is given in cm. Inserting the presented estimate for f [see Eq. (34.4)], it follows:

$$B_t = 4.5 \cdot 10^{-23} \frac{\eta}{L}\,[T]. \tag{34.8}$$

As an example, for a typical size of $L = 0.1$ μm, the result is $B_t = 4.5 \cdot 10^{-18}\eta$ [T]. The fact that η can indeed reach its maximal value, $\eta_{\max} = 1$ is discussed in the Appendix C. Therefore, $B_t = 4.5 \cdot 10^{-18}$ [T]. This result is discussed in the concluding Section of the present Chapter.

§ 35 Possible experimental setup to increase the parity violation effect

It is assumed in the previous derivations that the induced magnetic field is constant along the loop. However, the required periodic component of the magnetic field can be increased if the magnetic field is only present in the region around the Josephson junctions (see Fig. 36.1). To make this statement clear, one can rewrite Eq. (34.6) as

$$\begin{aligned} e\Phi_0 + \frac{a}{2}\sin t &= \int\int dS\, \frac{e}{\hbar}(B_0 + B_t \sin t) \\ &= \frac{eS}{\hbar}(B_0 + B_t \sin t)\,, \end{aligned} \tag{35.1}$$

where S is the effective area (part of the loop area, see Fig. 36.1), where the field is given by $(B_0 + B_t \sin t)$. Therefore, in the limit $a \to f+$, the expression for the periodic component of the magnetic field is

$$B_t = 1.4 \cdot 10^{-22} \frac{\eta L}{S}\,[\mathrm{T}]\,. \tag{35.2}$$

This expression explains why the localization of the magnetic field by the decrease of the total flux increases the required magnetic field. By choosing a large ratio L/S one may reach conditions satisfying the restrictions of existing experimental techniques. A large value of the ratio may be archived, e.g., by implementing a superconducting solenoid at the field-free part of the loop (i.e. at the right side of Fig. 36.1). Furthermore, the ratio $B_t/B_0 \approx L$, therefore, the large size of the loop provides also an improvement of the effect.

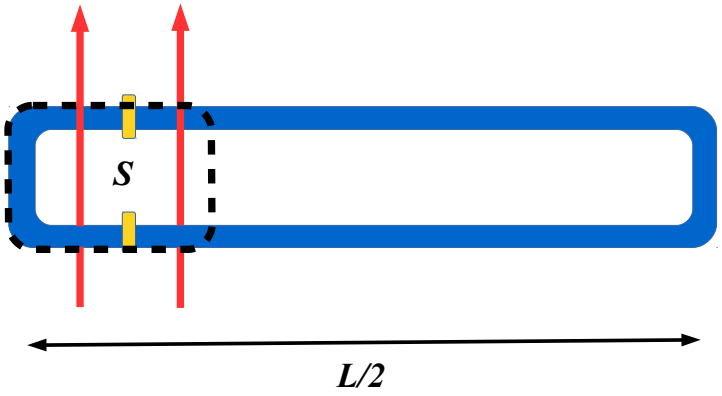

Figure 36.1 – The circular Josephson junction with an external magnetic field present in the effective area S in the vicinity of the SIS junctions only.

§ 36 Discussion

It is shown in Appendix C that the maximal mean spin value can be equal to unity, $\eta = 1$, for Cooper pairs in the unconventional ferromagnetic SC at some certain conditions, namely, in the region where the critical temperature for superconductivity T_{sc} is much smaller than the Curie temperature T_C. Thus one can finally obtain the amplitude of the periodic magnetic field required for the estimation presented in § 34 [cf. Eq. (34.8)]:

$$B_t = 4.5 \cdot 10^{-23} \frac{1}{L}\,, \tag{36.1}$$

where L is given in units of cm and B_t in units of Tesla. As an example, for the size of the circular Josephson junction a $L = 0.1$ μm, one obtains the value

$$B_t = 4.5 \cdot 10^{-18}\,[\mathrm{T}]\,. \tag{36.2}$$

Thus, the PV effect is 3 orders of magnitude stronger than in the case of the earlier theoretical works [21, 163]. These magnetic fields are close to the range of Superconducting QUantum Interference Devices (SQUIDs, see e.g. Ref. [179]).

Furthermore, the effect can be significantly improved by employing the experimental scheme described in § 35. For instance, without the implementation of this model, the magnetic field is

$$\begin{aligned} B_t &= 1.4 \cdot 10^{-22} \frac{\eta L}{S}\,[\mathrm{T}] \\ &= 4.5 \cdot 10^{-18}\,[\mathrm{T}]|_{\eta=1,\, L=0.1\mu m,\, S=\pi L^2}\,; \end{aligned} \tag{36.3}$$

then, by increasing the length of the loop to $L = 1$ mm at an unchanged effective surface S, B_t is augmented by 4 orders of magnitude:

$$B_t = 4.5 \cdot 10^{-14}[\mathrm{T}]|_{\eta=1,\, L=1mm,\, S=\pi L_o^2,\, L_o=0.1\mu m}\,. \tag{36.4}$$

Therefore, the PV effect is now 7 orders of magnitude larger than in the case of the earlier proposals [21, 163]. As a result, the PV effects in SC are anticipated to be observed in future. Such measurements will open the way to investigate the PV phenomenon by relatively compact experimental setups, and allow one to observe electroweak effects in a macroscopic system.

Summary and outlook

This thesis contains the investigation of several nuclear effects in atoms as well as in solid-state systems:

Internal pair conversion

The first process considered in this thesis is internal pair conversion in heavy atoms or ions. This is an alternative mechanism of electron-positron pair creation. Fundamental issues of the pair conversion process itself and its combination with initial Coulomb excitation of the nucleus can play an important role in numerous processes which are going to be examined at the FAIR facility in the near future [23]. In the framework of FAIR experiments it will be possible to observe bound-free and free-free pair production in the supercritical combined Coulomb field of two heavy colliding ions. Alternatively, pair creation via nuclear resonance may occur, therefore, in the present work this process has been investigated analytically and numerically. Numerical calculations have been provided for different EL and ML nuclear transitions with angular momenta $L > 0$, as well as for E0 (monopole) nuclear transitions. It appeared for heavy bare ions that in some energy regions, the rate of the bound-free pair conversion process can be greater than or comparable to the already experimentally investigated free-free case. We have found suitable experimental situations for the effective observation of the bound-free pair conversion process. Furthermore, we identified cases when pair conversion is dominant electromagnetic channel for the nucleus to decay. The present theoretical study can be useful for upcoming experimental investigations. The corresponding results are included in Refs. [1, 3, 4].

Pair conversion in muonic atoms

The pair production process in the decay of muonic atoms between discrete muonic energy levels is relevant for different applications of muonic atoms. For instance, muonic hydrogen has been used in precision experiments for determining the proton radius [30]. A surprising finding of these experiments was that the proton radius obtained is significantly smaller than the previously established value. A possible explanation of this puzzle might be some possible shortcoming of the quantum electrodynamic theory [30] of the bound muon, which relates the measured transition energies to the proton's size. Experiments on pair creation accompanying bound muonic decay in heavy atoms can provide an additional benchmark of this theoretical framework. It is also necessary to improve our understanding of muonic cascades in atoms, to investigate theoretically and experimentally the spectrum of particles created within muonic transitions from some highly excited state to the ground state. For this purpose, the present study introduces bound-free and free-free internal electron-positron pair creation accompanying muonic transitions between atomic levels. It turned out to be possible to observe in muonic atoms some behaviors similar to those in nuclear pair conversion. For instance, the pair produc-

tion with a bound electron possesses a maximum in the low-energy energy region. Conversely, when both the electron and positron are created as free, the probability monotonically increases as a function of the transition energy of the muon. The magnitude of the received numbers is also, surprisingly, the same as in the case of nuclear pair conversion. The corresponding results are included in Ref. [5].

Nuclear excitation by resonant positron annihilation

The time-reversed process of internal pair conversion, nuclear excitation by resonant positron annihilation (NERPA), can play an important role in the interactions of positrons with matter. NERPA constitutes a way to excite nuclei which is alternative to photo- and Coulomb excitation. In particular, NERPA can resonantly induce monopole transitions. NERPA is potentially relevant in numerous applications connected with positron-matter interaction and is also anticipated to provide novel means for the investigation of the structure of deformed nuclei and for nuclear model tests, as it can energy-selectively excite transitions of any multipolarity.

We conclude that the NERPA transition rate is the largest in medium-Z and heavy elements with the nuclear transition energy near the maximum of the cross section at about 2 MeV. In the elements satisfying these properties and possessing a metastable state populated by NERPA, the slow subsequent γ-decay may provide appropriate time gating for the observation of the reaction. Because of their cross section, together with their lifetime, ^{115}Sn and ^{115}In were found to be most suitable for possible measurements. The NERPA process is significantly enhanced for some elements such as e.g. ^{115}Sn.

We identified the strongest NERPA excitation so far for a 13.5-MeV giant dipole resonance (GDR) in ^{208}Pb. Since for such resonances the total nuclear level width is in the MeV range, these resonances are associated with the highest integrated NERPA cross sections. For instance, the estimation of the NERPA cross section integrated with the effective resonance width reaches $3.4 \cdot 10^4$ b·eV for the mentioned GDR, exceeding previous values for, e.g., ^{115}In [110, 111] by 8 orders of magnitude. GDRs can be efficiently excited even with a broadband positron beam generated in laser-plasma interactions by existing novel methods [41, 97]. For instance, for a positron beam with a 0.5-MeV width, Coulomb excitation of the GDR is strongly suppressed, since it requires positron kinetic energies higher by $2mc^2$ than NERPA. Therefore, exciting GDRs with laser-generated positron beams may be a viable alternative to observe NERPA, circumventing the difficulties caused by the low nuclear line width in the elements studied so far [110,111]. Furthermore, NERPA may be utilized for a selective excitation of a certain energy region of a giant resonance, enabling the investigation of the thermal evolution of the GDR width and structure. Normally such studies are done by Coulomb excitation experiments [117, 118] which does not allow a selective excitation but only an energy-selective detection of the subsequent γ decays. For the corresponding results one can refer to Refs. [1, 4]

Internal pair conversion following Coulomb excitation

In collision experiments at heavy ion accelerators it will be possible to observe bound-free and free-free pair production in the Coulomb field of heavy ions during their collision [23]. A new mechanism for pair production has been introduced in this work, i.e., nuclear-resonant electron-positron pair creation in heavy ion collisions.

The first theoretical results, presented in Chapter IV, show that at a sufficiently high experimental positron energy resolution it is possible to identify this process on the background of the

non-resonant pair production, which is going to be investigated in the mentioned experiments at FAIR. Therefore, upcoming experimental investigations are anticipated to bring fruitful results.

Pair creation in heavy ion channeling

We have shown that pair conversion via nuclear excitation in heavy ion collisions can be significantly enhanced by multiple periodic collisions in a crystal channeling experiment. This promising technique has been also investigated in the present work. In the reference frame of the traveling ions, the electromagnetic field of the periodic crystal structure may be regarded as a field of virtual photons with well-defined, equidistantly spaced discrete frequencies. For sufficiently fast ions, these frequencies are boosted into the MeV range, surpassing the pair creation threshold. In a direct channeling pair creation process, at photon energies above this threshold value, a free-free or bound-free pair can be created. In addition, when the virtual-photon frequency equals to the frequency of a nuclear transition in the channeling ion, a two-step resonant process occurs. In this channel the nucleus is excited, then it decays by internal pair conversion. As it has been shown, due to the coherent nature of the excitation, pair creation proceeding via nuclear resonances yields a quadratic scaling with the number of collisions, resulting in observable pair conversion rates.

Pair creation with channeling ions may also be regarded as a feasible alternative to photoproduction, since such intense coherent gamma-ray sources do not exist yet. These studies complement pair conversion by different strong electromagnetic fields such as optical or X-ray lasers [25]. The ion kinetic energies required for such investigations can be reached by present and upcoming experimental facilities, such as, e.g., FAIR. The kinetic energies of laser-generated ion beams have been constantly increasing in recent years (see, e.g., Ref. [43]), therefore, such ion beams may also be considered in the future for pair creation studies via channeling. Our results in this field can be found in Ref. [3].

Parity violation in unconventional superconductors

Weak-interaction effects have been investigated in this thesis on the example of parity violation phenomena in unconventional p-wave superconductors like UGe_2, where superconducting and ferromagnetic phases coexist. The presented calculation shows that the effect can be 3 orders of magnitude stronger than for the s-wave case which has been investigated before [164]. The required magnetic fields can be presently generated.

For instance, the amplitude of the periodic magnetic field required for the measurement with a characteristic size of the circular Josephson junction of $L = 0.1\ \mu$m is $B_t = 4.5 \cdot 10^{-18}\,$T. The magnitude of these magnetic fields are close to that which can be generated with present-day Superconducting QUantum Interference Devices (SQUIDs, see e.g. Ref. [179]).

The effect can be further improved by employing the experimental scheme of § 35. For instance, for the system treated in § 35, the parity violation effect appeared to be 7 orders of magnitude stronger than in the case of the earlier proposals [21,163]. Therefore, parity violation effects in superconductors are anticipated to be measurable in future experimental studies. This kind of measurements opens the way to investigate parity violation phenomena in relatively compact experimental setups. These results can be found in Ref. [2].

Outlook

In the present work several nuclear effects in atomic and solid-state physics have been investigated. However, these studies may be extended and there are some related processes which may be investigated subsequently.

Firstly, the discussed internal pair conversion process with a free or bound created electron can be considered as a second step of different mechanisms of nuclear excitation, which leads to numerous practical applications. For instance, in analogy to the investigated internal pair conversion after nuclear Coulomb excitation in heavy ion collisions, one can consider pair creation following nuclear photo-excitation by γ-rays with MeV energies. This can be of relevance for applications in material investigation, as it allows to detect certain nuclear transitions in compound materials.

Furthermore, one may consider the related process of photoionization via nuclear excitation, i.e. a scheme in which the nucleus is first excited by a photon, then the excited nuclear state formed this way decays by internal conversion. This process constitutes a competing channel of the well-known photoionization of atoms, however, with the active involvement of nuclear degrees of freedom. In contrast to pair production, here, the exciting photon may have lower energies in the X-ray regime. In this range of the electromagnetic spectrum, intense sources are readily available or are being built [43, 91, 92]. It would be interesting to study quantum interference effects between the direct and the nuclear-resonant photoionization amplitudes, which lead to Fano-type asymmetries [13] of the spectral lines.

The investigation of the NERPA process can be extended to benchmark certain nuclear models by measuring the structure of nuclear excitations. This may include, e. g., scanning the sublevels within giant resonances, or the level structure of complex nuclei.

Our studies on pair creation in nucleus-nucleus collisions included cases when a light nucleus is scattered on a heavy one. As the results show, the monochromatic positron line may be observed if the positron detectors resolution is high enough. Therefore, it would be desirable to extend our description to the case when both colliding partners are heavy ions.

One of the most promising effects for future extensions is pair production by ion planar channeling. Two possible reactions have been introduced in the present work, namely, direct pair production and pair creation via nuclear resonant excitation. One can consider also nonlinear direct pair production by two or more equivalent photons in the strong field of the crystal. Transition rates of these pair creation mechanisms may turn out to be significant, and thus lower ion kinetic energies would be needed to perform the channeling experiments.

As for parity non-conservation in superconductors, further schemes could be used to improve its observability. This work mostly discussed the improvement of the effect caused by the use of unconventional superconductors in the region of coexistence of superconducting and ferromagnetic phases. An additional method for an enlargement of the effect due to realization of a more complicated superconducting loop has been also introduced. However, one may also develop other geometries of the supposed experiment, or a significant enhancement may appear by the utilization of a different superconducting material. The formalism developed in the present thesis is general enough to allow for the treatment of further superconductors.

Appendix A

Evaluation of the radial integrals of the internal pair conversion matrix elements

This Appendix contains the evaluation of integrals containing the radial components of the wave functions for a bound electron and a free positron in the central Coulomb field of dimensionless nucleus with a charge Z_0. These radial integrals are defined as follows:

$$
\begin{aligned}
R_1 &= \int_0^\infty g_\kappa g_{\kappa'} h_L(\omega r) r^2 dr \,, \qquad \text{(A.1)}\\
R_2 &= \int_0^\infty f_\kappa f_{\kappa'} h_L(\omega r) r^2 dr \,,\\
R_3 &= \int_0^\infty f_\kappa g_{\kappa'} h_{L-1}(\omega r) r^2 dr \,,\\
R_4 &= \int_0^\infty g_\kappa f_{\kappa'} h_{L-1}(\omega r) r^2 dr \,,\\
R_5 &= \int_0^\infty f_\kappa g_{\kappa'} h_L(\omega r) r^2 dr \,,\\
R_6 &= \int_0^\infty g_\kappa f_{\kappa'} h_L(\omega r) r^2 dr \,.
\end{aligned}
$$

The radial part of the wave function for a free particle with a negative energy ($\epsilon = -E < -1$) and the Dirac angular momentum quantum number κ (i.e. the annihilating positron) is known analytically [62]:

$$
\begin{aligned}
f_\kappa(r) &= \sqrt{E+1} N [G_\kappa(r) - e^{-2i\eta} \tilde{G}_\kappa(r)] \,, \qquad \text{(A.2)}\\
g_\kappa(r) &= i\sqrt{E+1} N [G_\kappa(r) + e^{-2i\eta} \tilde{G}_\kappa(r)] \,, \qquad \text{(A.3)}
\end{aligned}
$$

where the functions

$$
\begin{aligned}
G_\kappa(r) &= r^{\gamma-1} e^{ipr} \, {}_1F_1(a; b; -2ipr) \,, \qquad \text{(A.4)}\\
\tilde{G}_\kappa(r) &= r^{\gamma-1} e^{ipr} \, {}_1F_1(a+1; b; -2ipr) \,, \qquad \text{(A.5)}
\end{aligned}
$$

are given in terms of the hypergeometric functions ${}_1F_1$ [66], the normalization constant is given by

$$
N = \frac{(2p)^\gamma e^{-\pi B/2} |\Gamma(a+1)|}{2\sqrt{\pi p}\,\Gamma(b)} \,, \qquad \text{(A.6)}
$$

and the further introduced quantities are:

$$\begin{aligned} \gamma &= \sqrt{\kappa^2 - (\alpha Z_0)^2}\,; \quad e^{-2i\eta} = \frac{\gamma + iB}{-\kappa + iB/E}\,; \\ p &= \sqrt{E^2 - 1}\,; \quad B = \frac{\alpha Z_0 E}{p}\,; \\ a &= \gamma + iB\,; \quad b = 2\gamma + 1\,. \end{aligned} \tag{A.7}$$

For a bound particle with energy E' and principal quantum number n, the bound-state Dirac quantum number κ' (i.e. for the annihilated bound electron), the radial part of the wave function has the form [65]:

$$\begin{aligned} g_{\kappa'}(r) &= \sqrt{1+E'}N_0 r^{\gamma'-1}e^{-p_0 r} \\ &\times \left[\left(\frac{n'+\gamma'}{E'} - \kappa'\right) {}_1F_1(-n', 2\gamma'+1, 2p_0 r) - n'\,{}_1F_1(1-n', 2\gamma'+1, 2p_0 r)\right], \end{aligned} \tag{A.8}$$

$$\begin{aligned} f_{\kappa'}(r) &= \sqrt{1-E'}N_0 r^{\gamma'-1}e^{-p_0 r} \\ &\times \left[\left(\frac{n'+\gamma'}{E'} - \kappa'\right) {}_1F_1(-n', 2\gamma'+1, 2p_0 r) + n'\,{}_1F_1(1-n', 2\gamma'+1, 2p_0 r)\right], \end{aligned} \tag{A.9}$$

where

$$N_0 = \frac{(2p_0)^{\gamma'+1/2}}{\Gamma(2\gamma'+1)} \sqrt{\frac{(1+E')\Gamma(2\gamma'+n'+1)}{4n'!((n'+\gamma')/E' - \kappa')(n'+\gamma')/E'}}\,, \tag{A.10}$$

with the bound Sommerfeld energy eigenvalues:

$$E' = \left(1 + \frac{(\alpha Z_0)^2}{(n - |\kappa'| + \gamma')^2}\right)^{-1/2}, \tag{A.11}$$

with the definitions $p_0 = \sqrt{1-E'^2}$, $n' = n - |\kappa'|$ and $\gamma' = \sqrt{\kappa'^2 - (\alpha Z_0)^2}$.

Inserting these wave functions into the expressions for the radial integrals following [62], one arrives to:

$$R_1 = i\sqrt{E-1}N \sum_{l=1}^{L+1} \frac{H_{L,l}}{\omega^l}\left(\tilde{I}_1^l + e^{-2i\eta}\tilde{I}_2^l\right), \tag{A.12}$$

$$R_2 = \sqrt{E+1}N \sum_{l=1}^{L+1} \frac{H_{L,l}}{\omega^l}\left(\tilde{I}_3^l - e^{-2i\eta}\tilde{I}_4^l\right),$$

$$R_3 = \sqrt{E+1}N \sum_{l=1}^{L} \frac{H_{L,l}}{\omega^l}\left(\tilde{I}_1^l - e^{-2i\eta}\tilde{I}_2^l\right),$$

$$R_4 = i\sqrt{E-1}N \sum_{l=1}^{L} \frac{H_{L,l}}{\omega^l}\left(\tilde{I}_3^l + e^{-2i\eta}\tilde{I}_4^l\right),$$

$$R_5 = \sqrt{E+1}N \sum_{l=1}^{L+1} \frac{H_{L,l}}{\omega^l}\left(\tilde{I}_1^l - e^{-2i\eta}\tilde{I}_2^l\right),$$

$$R_6 = i\sqrt{E-1}N \sum_{l=1}^{L+1} \frac{H_{L,l}}{\omega^l}\left(\tilde{I}_3^l + e^{-2i\eta}\tilde{I}_4^l\right),$$

where $H_{L,l} = \frac{(-i)^{L+2-l}}{2^{l-1}} \frac{(L+l-1)!}{(l-1)!(L-l+1)!}$, and the radial integrals are:

$$\begin{aligned}
\tilde{I}_1^l &= \int_0^\infty G_\kappa(r) g_{\kappa'}(r) r^{2-l} e^{i\omega r} dr\,, \qquad \text{(A.13)}\\
\tilde{I}_2^l &= \int_0^\infty \tilde{G}_\kappa(r) g_{\kappa'}(r) r^{2-l} e^{i\omega r} dr\,,\\
\tilde{I}_3^l &= \int_0^\infty G_\kappa(r) f_{\kappa'}(r) r^{2-l} e^{i\omega r} dr\,,\\
\tilde{I}_4^l &= \int_0^\infty \tilde{G}_\kappa(r) f_{\kappa'}(r) r^{2-l} e^{i\omega r} dr\,.
\end{aligned}$$

The four integrals $\tilde{I}_i^l$ can be calculated separately in an analytical form for different bound states. For instance, in the case of the $1s_{1/2}$ bound state, one can have following results:

$$\tilde{I}_1^l = N_0 \frac{\Gamma(\gamma+\gamma'-l+1)}{(p_0 - i(p+\omega))^{\gamma+\gamma'-l+1}} {}_2F_1\left(a, \gamma+\gamma'-l+1; b; \frac{2p}{p+\omega+ip_0}\right), \qquad \text{(A.14)}$$

$$\tilde{I}_2^l = N_0 \frac{\Gamma(\gamma+\gamma'-l+1)}{(p_0 - i(p+\omega))^{\gamma+\gamma'-l+1}} {}_2F_1\left(a+1, \gamma+\gamma'-l+1; b; \frac{2p}{p+\omega+ip_0}\right), \qquad \text{(A.15)}$$

and

$$\tilde{I}_3^l = -\sqrt{\frac{1-E'}{1+E'}}\tilde{I}_1^l\,, \qquad \text{(A.16)}$$

$$\tilde{I}_4^l = -\sqrt{\frac{1-E'}{1+E'}}\tilde{I}_2^l\,, \qquad \text{(A.17)}$$

where the normalization constant is

$$N_0 = (2\alpha Z)^{\gamma'+1/2} \sqrt{\frac{1+\gamma'}{2\Gamma(2\gamma'+1)}}. \qquad \text{(A.18)}$$

Appendix B

Cross section for a two-step process

The present Appendix contains the derivation of the total cross section for the two-step NERPA-γ process, i.e. NERPA followed by a radiative decay of the nucleus. This derivation is done with the extension of the formalism developed in Refs. [17,67,180]. In those works, the authors describe nuclear excitation by electron capture, also followed by γ-emission.

Let us describe the initial state of the system consisting of the nucleus, the bound electron and the free positron by the state function

$$|\Psi_i\rangle = |N_0\rangle_n \otimes |\pi\rangle_\pi \otimes |0\rangle_r \otimes |0\rangle_e, \tag{B.1}$$

which is written as a direct product of the state functions for the nucleus, the pair to be annihilated (π, electron+positron), the vacuum state of the photon field $|0\rangle_r$ and the remaining bound electrons $|0\rangle_e$. In analogy, one can also write the state function of the intermediate state (final state of NERPA):

$$|\Psi_m\rangle = |N_1^*\rangle_n \otimes |0\rangle_\pi \otimes |0\rangle_r \otimes |0\rangle_e, \tag{B.2}$$

and of the final state of NERPA-γ

$$|\Psi_f\rangle = |N_2^*\rangle_n \otimes |0\rangle_\pi \otimes |\vec{k}\sigma\rangle_r \otimes |0\rangle_e\,, \tag{B.3}$$

where $|\vec{k}\sigma\rangle_r$ describes the state of the created photon. $\vec{k}$ is the wave vector of this photon and σ describes its polarization state. We also take into account an additional possible type of intermediate states in which the nucleus is in an excited state, together with an excitation of other bound electrons:

$$|\Psi_{f'}\rangle = |N_2^*\rangle_n \otimes |0\rangle_\pi \otimes |0\rangle_r \otimes |e_{f'}\rangle_e, \tag{B.4}$$

where $|e_{f'}\rangle_e$ describes some excitations of one or more bound electrons. All these four wave functions are mutually orthogonal, and one can construct projector operators projecting on all

of these four sub-spaces:

$$\begin{aligned} I &= \sum_i |i\rangle\langle i| \,, \\ M &= \sum_m |m\rangle\langle m| \,, \\ F &= \sum_f |f\rangle\langle f| \,, \\ F' &= \sum_{f'} |f'\rangle\langle f'| \,, \end{aligned} \tag{B.5}$$

for the set of initial states (basis $|i\rangle = |N_i\rangle_n \otimes |\pi_i\rangle_\pi \otimes |0\rangle_r \otimes |0\rangle_e$ – some nuclear and pair state with the absence of photons and bound electron excitations), the set of intermediate states (basis $|m\rangle = |N_m\rangle_n \otimes |0\rangle_\pi \otimes |0\rangle_r \otimes |0\rangle_e$ – some nuclear state with the absence of photons, pairs and bound electron excitations), the set of final states (basis $|f\rangle = |N_f\rangle_n \otimes |0\rangle_\pi \otimes |\vec{k}_f \sigma_f\rangle_r \otimes |0\rangle_e$ – some nuclear and photon state with the absence of pairs and bound electron excitations) and the set of additional states (basis $|f'\rangle = |N'_f\rangle_n \otimes |0\rangle_\pi \otimes |0\rangle_r \otimes |e_{f'}\rangle_e$ – some nuclear and bound electron excitations with the absence of pairs and photons). Here, and in what follows, the summation over the i, m, f and f' indexes means the summation over discrete states and integration over continuum states of all subsystems involved. Neglecting two- or more-photon states, one can write the approximate completeness relation for the projectors as

$$I + M + F + F' = \mathbf{1} \,, \tag{B.6}$$

with $\mathbf{1}$ being the unity operator.

The total Hamiltonian consists of four independent parts for nuclear (n), electron-positron (π), photon (r) and bound electrons (e), and of three interactions:

$$H = H_n + H_\pi + H_r + H_e + H_{n\pi} + H_{nr} + H_{ne} + H_{\pi r} + H_{\pi e} + H_{er} \,. \tag{B.7}$$

The specific form of these Hamiltonians is not relevant for the present derivation. Most of them can be found in Ref. [17]. With the help of the projection operators one can split this Hamiltonian into a sum of zero-order and perturbation parts as

$$H = H_0 + V, \tag{B.8}$$

where the zero-order Hamiltonian consists of parts of H which is diagonal in the subspaces,

$$H_0 = IHI + MHM + FHF + F'HF', \tag{B.9}$$

and the perturbation is

$$\begin{aligned} V &\equiv H - H_0 \\ &= IHM + IHF + MHI + MHF \\ &+ FHI + FHM + IHF' + MHF' \\ &+ FHF' + F'HI + F'HM + F'HF \,. \end{aligned} \tag{B.10}$$

Here, MHI accounts for the NERPA process in the lowest order.

Now we introduce the transition operator [129]:

$$T(z) = V + VG(z)V\,, \tag{B.11}$$

where the Green operator of the system is [129]

$$G(z) = (z - H)^{-1}\,, \tag{B.12}$$

and z is a complex energy variable. The differential cross section for the process going between its initial and final states, following Fermi's golden rule, is defined in terms of the transition operator as [181]

$$\frac{d\sigma_{if}}{d\Omega_k}(E) = \frac{2\pi}{F_i}\lim_{\epsilon\to 0+}|\langle\Psi_f|T(E+i\epsilon)|\Psi_i\rangle|^2\rho_f\,, \tag{B.13}$$

where Ω_k is the angle of the emitted photon, F_i is the flux of incoming positrons and ρ_f denotes the density of the final photonic states.

Using the Lippmann-Schwinger equation, one can write the Born-type series for the transition operator with the zero-order Green operator $G_0 = (z - H_0)^{-1}$ as [129]

$$T(z) = V + VG_0(z)V + VG_0(z)VG_0(z)V + \ldots\,. \tag{B.14}$$

Since the initial and final states of these process belong to well-defined subspaces, one may consider the following projection of the transition operator only:

$$FTI = FVI + FVG_0VI + FVG_0VG_0VI + \ldots\,. \tag{B.15}$$

Here, the first term does not give any contribution to the NERPA process, it corresponds to direct photo-annihilation of the pair. The second term (second order in V) yields

$$\langle\Psi_f|FT^{(2)}I|\Psi_i\rangle = \sum_m \frac{\langle\Psi_f|H_{nr}|m\rangle\langle m|H_{n\pi}|\Psi_i\rangle}{z - E_m^0}, \tag{B.16}$$

where E_m^0 denotes the unperturbed energy eigenvalue of the state $|m\rangle$.

When continuing the perturbation expansion of the FTI in an assumption that in the first step one has $\Psi_i \to \Psi_m$ transition (NERPA process) and on the last step one has $\Psi_m \to \Psi_f$ transition (γ-photon emission), one may notice that the third order in V does not give any contribution to the total two-step process. The fourth order in V yields two terms with the proper initial and final states:

$$\begin{aligned} FVG_0VG_0VG_0VI &= FH_{nr}MG_0M \\ &\times (H_{nr}FG_0FH_{nr} + H_{n\pi}IG_0IH_{n\pi} + H_{ne}F'G_0F'H_{ne})MG_0MH_{n\pi}I\,. \end{aligned} \tag{B.17}$$

The first term describes emission and re-absorption of a virtual photon, the second one the creation and annihilation of a virtual electron-positron pair, and the third one a forward and backward gamma exchange between the nucleus and some bound electron.

The first term can be rewritten as

$$FH_{nr}MG_0MH_{nr}FG_0FH_{nr}MG_0MH_{n\pi}I = \sum_{m,m'} FH_{nr}MG_0|m\rangle\langle m|H_{nr}FG_0FH_{nr}|m'\rangle\langle m'|G_0MH_{n\pi}I\,. \tag{B.18}$$

The diagonal matrix element in the equation above is

$$\langle m|H_{nr}FG_0FH_{nr}|m\rangle = \sum_f \frac{\langle m|H_{nr}|f\rangle\langle f|H_{nr}|m\rangle}{z - E_f^0}\,,$$

where the eigenvalue equation $H_0|f\rangle = E_f^0|f\rangle$ holds. Using the equality

$$\lim_{\epsilon\to 0+} \frac{1}{x + i\epsilon} = P\left(\frac{1}{x}\right) - i\pi\delta(x)\,, \tag{B.19}$$

where the $P(\frac{1}{x})$ denotes the principal value, one can decompose the diagonal matrix element expression into

$$\sum_f \frac{\langle m|H_{nr}|f\rangle\langle f|H_{nr}|m\rangle}{E + i\epsilon - E_f^0} = \Delta E_m^{\rm NSE} - \frac{i}{2}\Gamma_m^{nr}\,, \tag{B.20}$$

where the nuclear self-energy correction is

$$\Delta E_m^{\rm NSE} = P\sum_f \frac{\langle m|H_{nr}|f\rangle\langle f|H_{nr}|m\rangle}{E + i\epsilon - E_f^0}\,, \tag{B.21}$$

and the radiative decay width of the nuclear state m is

$$\Gamma_m^{nr} = i\pi\sum_{f^0} |\langle m|H_{nr}|f0\rangle|^2. \tag{B.22}$$

In a similar manner, the radiative decay of the hole in the electron shell can be accounted for.

The second and the third terms in Eq. (B.18) can be decomposed in a similar way. Using the same abbreviations for the corresponding diagonal matrix element one can write:

$$\langle m|H_{n\pi}IG_0IH_{n\pi}|m\rangle = \Delta E_m^{\rm VP} - \frac{i}{2}\Gamma_m^{n\pi}\,, \tag{B.23}$$

where ΔE_m^{VP} is a vacuum polarization-self-energy correction to the nuclear state m and $\Gamma_m^{n\pi}$ is its internal pair conversion width. In analogy for the other diagonal matrix elements holds:

$$\langle m|H_{ne}F'G_0F'H_{ne}|m\rangle = \Delta E_m^{\rm NP} - \frac{i}{2}\Gamma_m^{ne}\,, \tag{B.24}$$

with ΔE_m^{NP} being the nuclear polarization correction to the nuclear states m, and Γ_m^{ne} is its internal conversion width.

Now the matrix elements of three terms in Eq. (B.18) for the fourth order in V can be rewritten as

$$\langle m|H_jG_0H_jG_0H_jG_0H_j|m\rangle = \sum_{m'} \frac{\langle m|H_jG_0H_j|m'\rangle\langle m'|H_jG_0H_j|m\rangle}{z - E_{q'}}\,,$$

where the index j stands for nr, $n\pi$ and ne. In analogy to Refs. [17, 67], one can adopt the so-called isolated resonances approximation by taking only a given m' state into account instead of a summation. This approximation is valid if the energy difference between neighboring

resonances is large compared to their total natural widths, which holds true for the considered nuclear transitions.

Higher even-order terms (6-th order, 8-th order, etc.) can be taken into account by a summation of the geometric series

$$\frac{1}{z-E_m^0}\sum_{k=0}^{\infty}x^k=\frac{1}{z-E_m^0}\frac{1}{1-x}\,, \tag{B.25}$$

where the dimensionless variable x denotes

$$\begin{aligned} x=\frac{1}{z-E_m^0}\,(\langle m|H_{nr}FG_0FH_{nr}|m\rangle+\langle m|H_{n\pi}IG_0IH_{n\pi}|m\rangle &+ \langle m|H_{ne}F'G_0F'H_{ne}|m\rangle \\ &+ \langle m|H_{er}FG_0FH_{er}|m\rangle)\,. \end{aligned} \tag{B.26}$$

Therefore, one obtains

$$\frac{1}{z-E_m^0}\sum_{k=0}^{\infty}x^k=\frac{1}{z-E_m^0-\Delta E_m^{\mathrm{VP}}-\Delta E_m^{\mathrm{NSE}}-\Delta E_m^{\mathrm{NP}}-\Delta E_m^{\mathrm{ESE}}+\frac{i}{2}\Gamma_m^{n\pi}+\frac{i}{2}\Gamma_m^{nr}+\frac{i}{2}\Gamma_m^{ne}+\frac{i}{2}\Gamma_m^{er}}\,. \tag{B.27}$$

It is now possible to write the final equation for the total process amplitude as

$$\langle\Psi_f|FT^{(2)}I|\Psi_i\rangle=\sum_m\frac{\langle\Psi_f|H_{nr}|m\rangle\langle m|H_{n\pi}|\Psi_i\rangle}{z-E_m^0-\Delta E_m^0+\frac{i}{2}\Gamma_m}, \tag{B.28}$$

where the total energy correction is $\Delta E_m^0=\Delta E_m^{\mathrm{VP}}+\Delta E_m^{\mathrm{NSE}}+\Delta E_m^{\mathrm{NP}}+\Delta E_m^{\mathrm{ESE}}$, and the total natural width of the excited state is defined as $\Gamma_m=\Gamma_m^{n\pi}+\Gamma_m^{nr}+\Gamma_m^{ne}+\Gamma_m^{er}$. This expression helps us to obtain the result for the angular-differential cross section:

$$\begin{aligned} \frac{d\sigma_{if}}{d\Omega_k}(E) &= \frac{2\pi}{F_i}\frac{|\langle\Psi_f|H_{nr}|\Psi_m\rangle|^2}{(E-E_m)^2+\frac{1}{4}\Gamma_m^2} \\ &\times\ |\langle\Psi_m|H_{n\pi}|\Psi_i\rangle|^2\rho_f\,, \end{aligned} \tag{B.29}$$

where the corrected energy is $E_m=E_m^0-\Delta E_m^0$.

By integrating over the photon emission solid angle Ω_k and averaging over the magnetic quantum numbers of leptons, nuclear states and positron directions, one receives the following expression for the total cross section of a given channel $i\to m\to f$:

$$\sigma_{i\to m\to f}(E)=\frac{2\pi^2}{p^2}\frac{\Gamma_{\mathrm{NERPA}}\Gamma_2^{\gamma}}{\Gamma_m}L_m(E-E_m)\,. \tag{B.30}$$

Where $p=\sqrt{E^2-m^2c^4}$ is the modulus of the initial positron momentum. Here, the following notations are used:

$$\Gamma_{\mathrm{NERPA}} = \Gamma_{i\to m}, \tag{B.31}$$

$$\Gamma_2^{\gamma} = \Gamma_{m\to f}, \tag{B.32}$$

with

$$\Gamma_{i\to m} = \frac{2\pi}{4(2I_i+1)} \sum_{M_i,M_m,m_e,m_p,} \int d\Omega_p |_e\langle 0| \otimes {}_r\langle 0| \otimes {}_\pi\langle 0| \otimes {}_n\langle N_1^*|H_{n\pi}|N_0\rangle_n|\pi\rangle_\pi|0\rangle_r|0\rangle_e|^2\rho_i \,,$$

$$\Gamma_{m\to f} = \frac{2\pi}{2I_m+1} \sum_{M_f,M_m,\sigma} \int d\Omega_k |_e\langle 0| \otimes {}_r\langle \vec{k}\sigma| \otimes {}_\pi\langle 0| \otimes {}_n\langle N_2^*|H_{n\pi}|N_1^*\rangle_n|0\rangle_\pi|0\rangle_r|0\rangle_e|^2\rho_f \,.$$

Here, the summation is performed: over projections of nuclear-angular momenta M_i, M_m and M_f for nuclear states N_0, N_1^* and N_2^* correspondingly; over angular momenta of annihilated electron (m_e) and positron (m_p); over polarizations of emitted photon (σ). For positron momentum, flux, and state density holds [129]:

$$p^2 = (2\pi)^3 F_i \rho_i \,, \tag{B.33}$$

and the normalized Lorentz profile describing the resonance line shape is

$$L_m(E-E_m) = \frac{1}{2\pi} \frac{\Gamma_m}{(E-E_m)^2+\Gamma_m^2/4} \,. \tag{B.34}$$

Expression (B.30) can be used for the description of the considered two-step NERPA-γ process, when using for E_m and Γ_m to the energy and the total width of the intermediate state excited by NERPA.

Appendix C

Mean spin value

In this Appendix we provide the calculation of the mean spin value of the Cooper pair in a p-wave unconventional superconductor in the case of the coexistence of superconducting and ferromagnetic phases.

In the present work, the model for the coexistence of superconductivity and ferromagnetism described in Ref. [182] for the case of an isotropic material is used. This formalism is extended here for anisotropic materials. In this model, the Hamiltonian is given as

$$H = \sum_{k\sigma}(\epsilon - \mu - \sigma M)c^{+}_{k\sigma}c_{k\sigma} - \frac{1}{2\nu}\sum_{kk',\sigma\sigma'} V(kk')c^{+}_{k\sigma}c^{+}_{-k\sigma'}c_{-k'\sigma'}c_{k'\sigma}, \tag{C.1}$$

where $\sigma = \pm 1$ indexes denote single-particle spin states, k is the single-particle momentum, ϵ denotes the non-magnetic part of the quasi-particle energy, and $c^{+}_{k\sigma}$ and $c_{k\sigma}$ are quasi-particle creation and annihilation operators, respectively. Furthermore, μ is the chemical potential, ν is the sample volume, V stands for the pairing potential, and the magnetization is $M = U(n_+ - n_-)/2$, defined in terms of the Stoner parameter U and number of pairs with the spin in the direction of the magnetization (n_+) and in the opposite direction (n_-). The Stoner parameter depends on the pressure, but it is independent of the temperature. In the ferromagnetic phase, only the pairs with spins parallel to the field can exist. One has to introduce two gap parameters $\Delta_\pm$ for spins in the direction of magnetization (+) and in the opposite direction (−).

In Ref. [182], the Matsubara Green's functions [183] for this Hamiltonian are constructed, and, after summation over Matsubara frequencies, the equations are obtained for the magnetization, number of particles and gap parameters. By replacing all summations by continuum integrals in dimensionless energy units, rescaled by the factor $\frac{\hbar^2}{2m^*}$, one receives the equations

$$M = \frac{U}{64\pi^3}\int_0^\infty d\epsilon_0 \int_0^\pi d\theta \int_0^{2\pi} d\phi \sin(\theta)\sqrt{\epsilon_0}\left(\frac{\epsilon_- \tanh(E_-/2T)}{E_-} - \frac{\epsilon_+ \tanh(E_+/2T)}{E_+}\right), \tag{C.2}$$

$$1 = \frac{V}{64\pi^3}\int_{\epsilon_{F+}-\omega_+}^{\epsilon_{F+}+\omega_+} d\epsilon_0 \int_0^\pi d\theta \int_0^{2\pi} d\phi \left(\frac{\sqrt{\epsilon_0}\sin^3\theta}{E_+}\tanh(E_+/2T)\right), \tag{C.3}$$

$$1 = \frac{V}{64\pi^3}\int_{\epsilon_{F-}-\omega_-}^{\epsilon_{F-}+\omega_-} d\epsilon_0 \int_0^\pi d\theta \int_0^{2\pi} d\phi \left(\frac{\sqrt{\epsilon_0}\sin^3\theta}{E_-}\tanh(E_-/2T)\right), \tag{C.4}$$

$$1 = \frac{1}{32\pi^3}\int_0^\infty d\epsilon_0 \int_0^\pi d\theta \int_0^{2\pi} d\phi \sin(\theta)\sqrt{\epsilon_0} \times\left(2 - \frac{\epsilon_- \tanh(E_-/2T)}{E_-} - \frac{\epsilon_+ \tanh(E_+/2T)}{E_+}\right), \tag{C.5}$$

where the following quantities have been introduced:

$$\epsilon_{F\pm} = \mu \pm M, \tag{C.6}$$

$$\epsilon_\pm = \epsilon - \epsilon_{F\pm}, \tag{C.7}$$

$$E_\pm = \sqrt{\epsilon_\pm^2 + \sin^2\theta\Delta_\pm^2}, \tag{C.8}$$

$$\omega_\pm = 0.01\epsilon_{F\pm}. \tag{C.9}$$

The integration over variables ϵ_0, θ and ϕ corresponds to the integration over the three-dimensional momentum of the pair. Equation (C.2) is the expression for the magnetization in the ferromagnetic superconductor. Eq. (C.3), together with Eq. (C.4), presents the gap equation for pairs polarized in or opposite to the direction of the magnetization. Finally, Eq. (C.5) expresses the conservation of the number of pairs.

In an isotropic case, considered before in Ref. [182], the relation $\epsilon = \epsilon_0$ holds. However, for anisotropic materials, during the change of the summation over $\vec{k}$ to three dimensional integration, the angular integrals in spherical coordinates remain the same, however, the radial variables are changed:

$$k^2 = k_0^2\left(\left(\frac{c}{a}\sin\theta\cos\phi\right)^2 + \left(\frac{c}{b}\sin\theta\sin\phi\right)^2 + \left(\frac{c}{c}\cos\theta\right)^2\right), \tag{C.10}$$

with a, b, c being the crystal cell parameters. Thus, one has 3 integrals over k_0, θ and ϕ, which change to integrals over ϵ_0, θ and ϕ, and the energy in all equations depends on the angles:

$$\epsilon = \epsilon_0\left(\left(\frac{c}{a}\sin\theta\cos\phi\right)^2 + \left(\frac{c}{b}\sin\theta\sin\phi\right)^2 + \left(\frac{c}{c}\cos\theta\right)^2\right). \tag{C.11}$$

Finally, one arrives to 4 equations, Eqs. (C.2-C.5), for 4 the variables $M, \Delta_\pm, \mu$, with U, V and T as parameters. These equations have to be solved self-consistently. The sought-after mean spin value is given by $\eta = 2M/U$. The Stoner parameter U is determined by the Curie temperature T_C at a certain pressure [184]. It is possible to obtain it by a self-consistent solution of Eqs. (C.2) and (C.5) with $\delta \equiv 0$ and assuming the condition that the magnetization appears at temperatures $T < T_C$ only. The method of this solution is similar to the method for the calculation of η presented below. The pairing parameter V is determined by the condition that at temperatures below the critical SC temperature, $T < T_{sc}$, the following should hold: $\Delta \neq 0$, and at $T > T_{sc}$ there is no superconductivity ($\Delta = 0$).

The following algorithm can be used for the self-consistent solution of the full set of equations [Eqs. (C.2)-(C.5)] to evaluate η for certain values of U and V (parameters of the SC):

(i) With the help of Eq. (C.3) [or Eq. (C.4)] one can construct the function $\Delta(k)$ in such a way that $\Delta_\pm = \Delta(\mu \pm M)$. It is possible to do so since both equations depend on the combinations $\mu \pm M$ only.

(ii) By Eqs. (C.2) and (C.5) one can construct the equations

$$M = \mp\frac{U}{2}W(\mu \pm M), \tag{C.12}$$

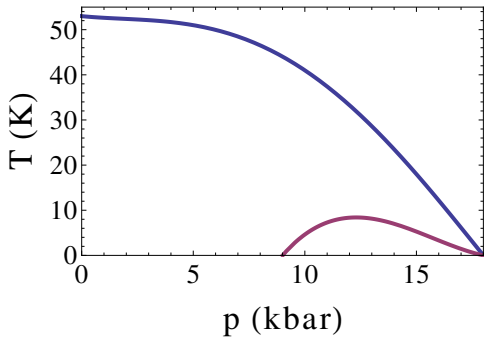

Figure C.1 – The p–T phase diagram for UGe_2 [185]. The lower curve $10\times T_{sc}(p)$ corresponds to the critical temperature of superconductivity, the upper one to the Curie critical temperature of ferromagnetism, $T_C(p)$.

where

$$W(k) = 1 - \frac{1}{16\pi^3}\int_0^\infty d\epsilon_0 \int_0^\pi d\theta \int_0^{2\pi} d\phi \sqrt{\epsilon_0}\sin\theta\left(1 - \frac{\epsilon_\pm \tanh(E_\pm/2T)}{E_\pm}\right). \tag{C.13}$$

(iii) Let us take $x = \mu - M$, yielding two simple equations, namely:

$$M = \frac{U}{2}W(x)\,, \quad M = -\frac{U}{2}W(x+2M)\,, \tag{C.14}$$

which deliver the final equation for x,

$$W(x) = -W(x + UW(x))\,. \tag{C.15}$$

(iv) From x one can obtain the values of all parameters as follows:

$$M = \frac{U}{2}W(x) \tag{C.16}$$
$$\mu = x + M\,, \tag{C.17}$$
$$\Delta_- = \Delta(x) \tag{C.18}$$
$$\Delta_+ = \Delta(x+2M)\,. \tag{C.19}$$

Let us note that these equations have a solution with $M \neq 0$ in the case when $U > U_c$ only. U_c is the critical value of the Stoner parameter and it depends on T.

Using this numerical algorithm one can perform the calculations for the cell parameters of UGe_2, namely, $a = 14.928$ pm, $b = 4.116$ pm, $c = 4.036$ pm [177]. In this work these calculations have been performed for different pressures and temperatures both in the region of the coexistence of ferromagnetic and superconductive phases [185] as well as in the pure ferromagnetic region (see Fig. C.1). It appears (see Fig. C.2) that at all pressures between approximately 9 and 12 kbar, the value of η is almost unity for all temperatures $T < T_{sc}$, however, above 12 kbar, η decrees with the increase of the pressure. These numerical results show that at some pressures in the region of interest where T_C is much larger than T_{sc}, and η is equal to unity.

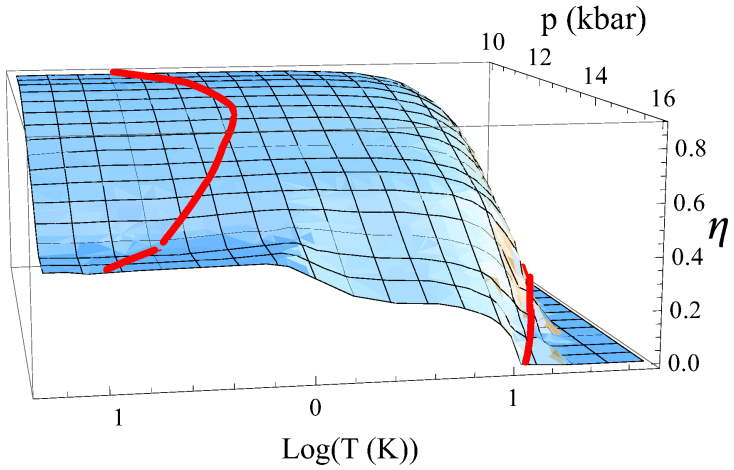

Figure C.2 – The dependence of the mean spin η on the pressure and temperature in the regions $T < T_{sc}$ (below the first red curve) and $T_{sc} < T < T_C$ (between the red curves). The data on $T_{sc}(p)$ and $T_C(p)$ are taken from Ref. [185].

Bibliography

[1] N. A. Belov and Z. Harman. *Phys. Lett. B*, 741:61, 2015.

[2] N. A. Belov and Z. Harman. arXiv:1411.1878. 2014.

[3] N. A. Belov and Z. Harman. arXiv:1411.5711. 2014.

[4] N. A. Belov and Z. Harman. To be published.

[5] N. A. Belov and Z. Harman. To be published.

[6] A. Pálffy. *Cont. Phys.*, 51:471, 2010.

[7] D. S. Hughes and C. Eckart. *Phys. Rev.*, 36:694, 1930.

[8] J. H. Bartlett and J. J. Gibbons. *Phys. Rev.*, 44:538, 1933.

[9] E. Fermi. *Z. Phys.*, 60:320, 1930.

[10] P. Güttinger. *Z. Phys.*, 64:749, 1930.

[11] G. Breit and F. W. Doermann. *Phys. Rev.*, 36:1262, 1930.

[12] S. Goudsmit and R. F. Bacher. *Z. Phys.*, 66:13, 1930.

[13] E. U. Condon and G. H. Shortley. *The Theory of Atomic Spectra*. Cambridge University Press, 1963.

[14] J. R. Crespo López-Urrutia, P. Beiersdorfer, D. W. Savin, and K. Widmann. *Phys. Rev. Lett.*, 77:826, 1996.

[15] S. Sturm, F. Kohler, J. Zatorski, A. Wagner, Z. Harman, G. Werth, W. Quint, C. H. Keitel and K. Blaum. *Nature*, 506:467, 2014.

[16] H. Casimir. *Nature*, 126:953, 1930.

[17] A. Pálffy, W. Scheid, and Z. Harman. *Phys. Rev. A*, 73:012715, 2006.

[18] L. W. Alvarez. *Phys. Rev.*, 52:134–135, 1937.

[19] C. S. Wu, E. Ambler, R. W. Hayward, D. D. Hoppes, and R. P. Hudson. *Phys. Rev.*, 105:1413, 1957.

[20] M.A. Bouchiat and C. Bouchiat. *Rep. Progr. Phys.*, 60(11):1351, 1997.

[21] A. I. Vainshtein and I. B. Khriplovich. *Sov. Phys. JETP Lett.*, 20:34, 1974.

[22] C. K. Agger and A. H. Sørensen. *Phys. Rev. A*, 55:402, 1997.

[23] FAIR Conceptual Design Report. Gesellschaft für Schwerionenforschung, `www.fair-center.de/fileadmin/fair/publications_FAIR/FAIR_CDR.pdf`, 2001.

[24] V. V. Okorokov. *Sov. Phys. JETP Lett.*, 2:111, 1965.

[25] Extreme Light Infrastructure European Project. `www.extreme-light-infrastructure.eu`, 2011.

[26] J. Berges, D. Gelfand, and J. Pruschke. *Phys. Rev. Lett.*, 107:061301, 2011.

[27] J. Berges, J. Pruschke, and A. Rothkopf. *Phys. Rev. D*, 80:023522, 2009.

[28] F. Hebenstreit, A. Ilderton, M. Marklund, and J. Zamanian. *Phys. Rev. D*, 83:065007, 2011.

[29] F. Hebenstreit, J. Berges, and D. Gelfand. *Phys. Rev. D*, 87:105006, 2013.

[30] R. Pohl, A. Antognini, F. Nez, F. D. Amaro, F. Biraben, J. M. R. Cardoso, D. S. Covita, A. Dax, S. Dhawan, L. M. P. Fernandes, A. Giesen, Th. Graf, Th. W. Hänsch, P. Indelicato, L. Julien, C.-Y. Kao, P. Knowles, E.-O. Le Bigot, Y.-W. Liu, J. A. M. Lopes, L. Ludhova, C. M. B. Monteiro, F. Mulhauser, T. Nebel, P. Rabinowitz, J. M. F. dos Santos, L. A. Schaller, K. Schuhmann, C. Schwob, D. Taqqu, J. F. C. A. Veloso, and F. Kottmann. *Nature*, 466:213, 2010.

[31] R. Pohl, H. Daniel, F. J. Hartmann, P. Hauser, F. Kottmann, V. E. Markushin, M. Mühlbauer, C. Petitjean, W. Schott, D. Taqqu, and P. Wojciechowski-Grosshauser. *Phys. Rev. Lett.*, 97:193402, 2006.

[32] G. B. Andresen et al. *Nature*, 468(7324):673, 2010.

[33] O. Adriani et al. *Phys. Rev. Lett.*, 111(8):081102, 2013.

[34] E. G. Adelberger et al. *Rev. Mod. Phys.*, 83(1):195, 2011.

[35] G. Mühllehner and J. S Karp. *Phys. Med. Biol.*, 51:R117, 2006.

[36] C. M. Surko, G. F. Gribakin, and S. J. Buckman. *J. Phys. B*, 38(6):R57, 2005.

[37] Josef Speth and Adriaan van der Woude. *Rep. Progr. Phys.*, 44(7):719, 1981.

[38] J. Wambach, V. A. Madsen, G. A. Rinker, and J. Speth. *Phys. Rev. Lett.*, 39:1443, 1977.

[39] E. Borie and G.A. Rinker. *Rev. Mod. Phys.*, 54(1), 1982.

[40] P. A. M. Dirac. *Proc. Roy. Soc. A*, 117:610, 1928.

[41] G. Sarri et al. *Phys. Rev. Lett.*, 110(25):255002, 2013.

[42] A. Gonoskov, I. Gonoskov, C. Harvey, A. Ilderton, A. Kim, M. Marklund, G. Mourou, and A. Sergeev. *Phys. Rev. Lett.*, 111:060404, 2013.

[43] A. Di Piazza, C. Müller, K. Z. Hatsagortsyan, and C. H. Keitel. *Rev. Mod. Phys.*, 84:1177, 2012.

[44] H. Chen et al. *Phys. Rev. Lett.*, 105(1):015003, 2010.

[45] A. M. Fedotov, N. B. Narozhny, G. Mourou, and G. Korn. *Phys. Rev. Lett.*, 105:080402, 2010.

[46] M. Ruf, G. R Mocken, C. Müller, K. Z. Hatsagortsyan, and C. H Keitel. *Phys. Rev. Lett.*, 102(8):080402, 2009.

[47] A. Di Piazza, E. Lötstedt, A. I. Milstein, and C. H. Keitel. *Phys. Rev. Lett.*, 103(17):170403, 2009.

[48] A. R. Bell and John G. Kirk. *Phys. Rev. Lett.*, 101:200403, 2008.

[49] R. Schützhold, H. Gies, and G. Dunne. *Phys. Rev. Lett.*, 101:130404, 2008.

[50] C. Müller, A. B. Voitkiv, and N. Grün. *Phys. Rev. Lett.*, 91(22):223601, 2003.

[51] R. Alkofer, M. B. Hecht, C. D. Roberts, S. M. Schmidt, and D. V. Vinnik. *Phys. Rev. Lett.*, 87:193902, 2001.

[52] G. Baur, K. Hencken, and D. Trautmann. *Phys. Rep.*, 453:1, 2007.

[53] G. Q. Li and C. Gale. *Phys. Rev. Lett.*, 81:1572, 1998.

[54] C. R. Vane, S. Datz, P. F. Dittner, H. F. Krause, C. Bottcher, M. Strayer, R. Schuch, H. Gao, and R. Hutton. *Phys. Rev. Lett.*, 69:1911, 1992.

[55] K. Rumrich, K. Momberger, G. Soff, W. Greiner, N. Grün, and W. Scheid. *Phys. Rev. Lett.*, 66:2613, 1991.

[56] W. Greiner, B. Müller, and J. Rafelski. *"Quantum Electrodynamics of Strong Fields: With an Introduction into Modern Relativistic Quantum Mechanics"*. Springer Publishing Company, Inc., 1985.

[57] A. N. Artemyev, T. Beier, J. Eichler, A. E. Klasnikov, C. Kozhuharov, V. M. Shabaev, T. Stöhlker, and V. A. Yerokhin. *Phys. Rev. A*, 67:052711, 2003.

[58] P. Helander and D. J. Ward. *Phys. Rev. Lett.*, 90:135004, 2003.

[59] A. E. Shabad and V. V. Usov. *Nature*, 295:215, 1982.

[60] M. E. Rose and G. E. Uhlenbeck. *Phys. Rev.*, 48:211, 1935.

[61] S. D. Bloom. *Phys. Rev.*, 88:312, 1952.

[62] P. Schlüter, G. Soff, and W. Greiner. *Phys. Rep.*, 75:327, 1981.

[63] P. Schlüter, G. Soff, and W. Greiner. *Z. Phys. A*, 303:189, 1981.

[64] A. N. Vasil'ev. *Functional Methods in Quantum Field Theory and Statistical Physics*. CRC Press, 1998.

[65] V. B. Berestetskii, E. M. Lifshitz, and L. P. Pitaevskii. *Relativistic Quantum Theory*. Pergamon Press, 1971.

[66] M. Abramowitz and I.A. Stegun. *Handbook of Mathematical Functions*. National Bureau of Standards, 1972.

[67] A. Pálffy, Z. Harman, and W. Scheid. *Phys. Rev. A*, 75:012709, 2007.

[68] A. Pálffy and Z. Harman. *Phys. Rev. A*, 77(4):042704, 2008.

[69] A. R. Edmonds. *Angular Momentum in Quantum Mechanics*. Princeton University Press, 1996.

[70] F. Salvat. *Comp. Phys. Comm.*, 90:151, 1995.

[71] U. Becker, N. Grün, and W. Scheid. *J. Phys. B*, 20(9):2075, 1987.

[72] A. Passoja. *Z. Phys. A*, 325:299, 1986.

[73] R. J. Lombard, C. F. Perdrisat, and J. H. Brunner. *Nucl. Phys. A*, 110(1):41, 1968.

[74] A. H. Wuosmaa. *Phys. Rev. C*, 57:R2794, 1998.

[75] NuDat 2.6 Database of the National Nuclear Data Center. `www.nndc.bnl.gov/nudat2/`.

[76] S. C. Wu. *Nuclear Data Sheets*, 110:681, 2009.

[77] F. G. Kondev. *Nuclear Data Sheets*, 109:1527, 2008.

[78] F. G. Kondev and S. Lalkovsky. *Nuclear Data Sheets*, 112:707, 2011.

[79] F. G. Kondev and S. Zhu. *Nuclear Data Sheets*, 109:699, 2008.

[80] F. G. Kondev. *Nuclear Data Sheets*, 101:521, 2004.

[81] M. J. Martin. *Nuclear Data Sheets*, 108:1583, 2007.

[82] M. S. Basunia. *Nuclear Data Sheets*, 108:633, 2007.

[83] H. Grotch and E. Kazes. *J. Phys. G*, 1(5), 1975.

[84] W. R. Johnson, S. A. Blundell, and J Sapirstein. *Phys. Rev. A*, 37(8), 1988.

[85] V. A. Yerokhin and A. Surzhykov. *Phys. Rev. A, 82*, 82, 2010.

[86] M. E. Rose. *Relativistic Electron Theory*. John Wiley & Sons, 1961.

[87] F. J. Hartmann and R. Bergmann. *Z. Phys. A*, 305, 1982.

[88] E. M. Lifshitz, L. D. Landau, L. P. Pitaevskii, and V. B. Berestetskii. *Theoretical Physics. Volume IV. Quantum Electrodynamics.* Elsevier Science and Technology Books, 1982.

[89] W. R. Johnson, D. J. Buss, and C. O. Carroll. *Phys. Rev.*, 135:A1232, 1964.

[90] R. D. Present and S. C. Chen. *Phys. Rev.*, 85(3):447, 1952.

[91] Stanford LCLS Specifications, `https://slacportal.slac.stanford.edu/sites/lcls_public/Instruments/SXR/Pages/Specifications.aspx`.

[92] European XFEL Project, `http://xfel.desy.de/technical_information/photon_beam_parameter/`.

[93] A. Pálffy and H. A. Weidenmüller. *Phys. Rev. Lett.*, 112:192502, 2014.

[94] J. P. Blaizot, J. F. Berger, J. Dechargé, and M. Girod. *Nucl. Phys. A*, 591(3):435, 1995.

[95] L. P. Gaffney et al. *Nature*, 497(7448):199, 2013.

[96] C. Müller and C. H Keitel. *Nature Photonics*, 3(5):245, 2009.

[97] G. Sarri, K. Poder, J. Cole, W. Schumaker, A. Di Piazza, B. Reville, D. Doria, B. Dromey, L. Gizzi, A. Green, G. Grittani, S. Kar, C. H. Keitel, K. Krushelnick, S. Kushel, S. Mangles, Z. Najmudin, A. G. R. Thomas, M. Vargas, and M. Zepf. arxiv:1312.0211. 2014.

[98] G. A. Mourou and T. Tajima. *Science*, 331(7):41, 2011.

[99] K. W. D. Ledingham, P. McKenna, and R. P. Singhal. *Science*, 300(5622):1107, 2003.

[100] P. McKenna, K. W. D. Ledingham, T. McCanny, R. P. Singhal, I. Spencer, M. I. K. Santala, F. N. Beg, K. Krushelnick, M. Tatarakis, M. S. Wei, E. L. Clark, R. J. Clarke, K. L. Lancaster, P. A. Norreys, K. Spohr, R. Chapman, and M. Zepf. *Phys. Rev. Lett.*, 91:075006, 2003.

[101] K. W. D. Ledingham, I. Spencer, T. McCanny, R. P. Singhal, M. I. K. Santala, E. Clark, I. Watts, F. N. Beg, M. Zepf, K. Krushelnick, M. Tatarakis, A. E. Dangor, P. A. Norreys, R. Allott, D. Neely, R. J. Clark, A. C. Machacek, J. S. Wark, A. J. Cresswell, D. C. W. Sanderson, and J. Magill. *Phys. Rev. Lett.*, 84:899, 2000.

[102] K. M. Spohr, M. Shaw, W. Galster, K. W. D. Ledingham, L. Robson, J. M. Yang, P. McKenna, T. McCanny, J. J. Melone, K.-U. Amthor, F. Ewald, B. Liesfeld, H. Schwoerer, and R. Sauerbrey. *New J. Phys.*, 10(4):043037, 2008.

[103] O. Kocharovskaya, R. Kolesov, and Y. Rostovtsev. *Phys. Rev. Lett.*, 82:3593, 1999.

[104] F. Vagizov, V. Antonov, Y. V. Radeonychev, R. N. Shakhmuratov, and O. Kocharovskaya. *Nature*, 508(7494):80, 2014.

[105] R. Röhlsberger, H.-C. Wille, K. Schlage, and B. Sahoo. *Nature*, 482(7384):199, 2012.

[106] R. Röhlsberger, K. Schlage, B. Sahoo, S. Couet, and R. Rüffer. *Science*, 328(5983):1248, 2010.

[107] J. Gunst, Y. A. Litvinov, C. H. Keitel, and A. Pálffy. *Phys. Rev. Lett.*, 112:082501, 2014.

[108] K. P. Heeg, H.-C. Wille, K. Schlage, T. Guryeva, D. Schumacher, I. Uschmann, K. S. Schulze, B. Marx, T. Kämpfer, G. G. Paulus, R. Röhlsberger, and J. Evers. *Phys. Rev. Lett.*, 111:073601, 2013.

[109] T. J. Bürvenich, J. Evers, and C. H. Keitel. *Phys. Rev. Lett.*, 96:142501, 2006.

[110] D. B. Cassidy, A. W. Hunt, P. Asoka-Kumar, B.V. Bhat, T.E. Cowan, R.H. Howell, K.G. Lynn, A.P. Mills Jr., J.C. Palathingal, and J.A. Golovchenko. *Phys. Rev. C*, 64(5):054603, 2001.

[111] T. Saigusa and S. Shimizu. *Hyp. Int.*, 89(1):445, 1994.

[112] D. Bucurescu. *Phys. At. Nucl.*, 70(8):1336, 2007.

[113] D. P. Grechukhin and A. A. Soldatov. *Sov. Phys. JETP*, 47:6, 1978.

[114] V. M. Kolomietz. *J. Phys. G: Nucl. Part. Phys.*, 16(4):615, 1990.

[115] E. L. Church and J. Weneser. *Phys. Rev.*, 103:1035, 1956.

[116] A. Bohr and B. R. Mottelson. *Nuclear Structure. Volume I.* World Scientific, 1998.

[117] G. Enders, F. D. Berg, K. Hagel, W. Kühn, V. Metag, R. Novotny, M. Pfeiffer, O. Schwalb, R. J. Charity, A. Gobbi, R. Freifelder, W. Henning, K. D. Hildenbrand, R. Holzmann, R. S. Mayer, R. S. Simon, J. P. Wessels, G. Casini, A. Olmi, and A. A. Stefanini. *Phys. Rev. Lett.*, 69:249, 1992.

[118] M. P. Kelly, K. A. Snover, J. P. S. van Schagen, M. Kicińska-Habior, and Z. Trznadel. *Phys. Rev. Lett.*, 82:3404, 1999.

[119] F. Bečvář, P. Cejnar, R. E. Chrien, and J. Kopecký. *Phys. Rev. C*, 46:1276, 1992.

[120] S. Helmrich, K. Spenneberg, and A. Pálffy. *Phys. Rev. C*, 90:015802, 2014.

[121] A. Avdeenkov, S. Goriely, S. Kamerdzhiev, and S. Krewald. *Phys. Rev. C*, 83:064316, 2011.

[122] M. Kmieciek, A. Maj, J. Styczeń, P. Bednarczyk, M. Brekiesz, J. Grębosz, M. Lach, W. Męczyński, M. Ziębliński, K. Zuber, A. Bracco, F. Camera, G. Benzoni, B. Million, S. Leoni, O. Wieland, B. Herskind, D. Curien, N. Dubray, J. Dudek, N. Schunck, and K. Mazurek. *Acta Phys. Pol. B*, 36, 2005.

[123] E. Litvinova and N. Belov. *Phys. Rev. C*, 88(3):031302, 2013.

[124] S. Goriely, E. Khan, and M. Samyn. *Nucl. Phys. A*, 739(3–4):331, 2004.

[125] A. Messiah. *Quantum Mechanics*. Dover Publications, New York, 1999.

[126] A. R. Edmonds. *Angular Momentum in Quantum Mechanics*. Princeton, New Jersey, 1957.

[127] B. Elbek. *Determination of Nuclear Transition Probabilities by Coulomb Excitation*. Ejnar Munksgaards Forlag, 1963.

[128] E. V. Tkalya. *Nucl. Phys. A*, 539(2):209, 1992.

[129] R. G. Newton. *Scattering Theory of Waves and Particles*. New York, 2002.

[130] G. Audi, F. G. Kondev, M. Wang, B. Pfeiffer, X. Sun, J. Blachot, and M. MacCormick. *Chin. Phys. C*, 36:1157, 2012.

[131] A. Winter and K. Adler. *Nucl. Phys. A*, 319:518, 1979.

[132] U. Becker, N. Grün, and W. Scheid. *J. Phys. B*, 20:2075, 1987.

[133] V. V. Okorokov. *Sov. J. Nucl. Phys.*, 2:719, 1965.

[134] Y. Nakano, Y. Takano, T. Ikeda, Y. Kanai, S. Suda, T. Azuma, H. Bräuning, A. Bräuning-Demian, D. Dauvergne, Th. Stöhlker, and Y. Yamazaki. *Phys. Rev. A*, 87(6):060501, 2013.

[135] Y. Nakano, C. Kondo, A. Hatakeyama, Y. Nakai, T. Azuma, K. Komaki, Y. Yamazaki, E. Takada, and T. Murakami. *Phys. Rev. Lett.*, 102:085502, 2009.

[136] Y. Nakai, Y. Nakano, T. Azuma, A. Hatakeyama, C. Kondo, K. Komaki, Y. Yamazaki, E. Takada, and T. Murakami. *Phys. Rev. Lett.*, 101:113201, 2008.

[137] E. Testa, P. N. Abufager, F. Bosch, A. Bräuning-Demian, H. Bräuning, M. Chevallier, C. Cohen, D. Dauvergne, A. Gumberidze, A. L'Hoir, R. Kirsch, C. Kozhuharov, D. Liesen, P. H. Mokler, J.-C. Poizat, C. Ray, R. D. Rivarola, J. P. Rozet, Th. Stöhlker, S. Toleikis, M. Toulemonde, D. Vernhet, and P. Verma. *Phys. Rev. A*, 76(6), 2009.

[138] C. Kondo, S. Masugi, Y. Nakano, A. Hatakeyama, T. Azuma, K. Komaki, Y. Yamazaki, T. Murakami, and E. Takada. *Phys. Rev. Lett.*, 97:135503, 2006.

[139] S. Andriamonje, K. Beckert, M. Chevallier, C. Cohen, D. Dauvergne, J. Dural, H. Eickhoff, B. Franzke, H. Geissel, R. Kirsch, A. L'Hoir, P. H. Mokler, R. Moshammer, F. Nickel, F. Nolden, J.-C. Poizat, H.-T. Prinz, H. Reich, J. Remillieux, F. Sanuy, C. Scheidenberger, D. Schmaus, M. Steck, Th. Stöhlker, and M. Toulemonde. *J. Phys. B*, 30(22):5099, 1997.

[140] S. Andriamonje, M. Chevallier, C. Cohen, N. Cue, D. Dauvergne, J. Dural, R. Genre, Y. Girard, R. Kirsch, A. l'Hoir, J.-C. Poizat, Y. Quéré, J. Remillieux, D. Schmaus, and M. Toulemonde. *Phys. Lett. A*, 164(2):184, 1992.

[141] Th. Stöhlker. Private communication, 2014.

[142] V. V. Balashov and I. V. Bodrenko. *Phys. Lett. A*, 352(1–2):129, 2006.

[143] S. Shindo and Y. H. Ohtsuki. *Phys. Rev. B*, 14:3929, 1976.

[144] H. Crawford and R. H. Ritchie. *Phys. Rev. A*, 20:1848, 1979.

[145] Yu. L. Pivovarov and A. A. Shirokov. *Sov. J. Nucl. Phys.*, 44:569, 1986.

[146] Yu. L. Pivovarov, A. A. Shirokov, and S. A. Vorobiev. *Nucl. Phys. A*, 509:800, 1990.

[147] N. Cue and J. C. Kimball. *Phys. Rep.*, 125:69, 1985.

[148] J. D. Jackson. *Classical Electrodynamics*. Wiley & Sons, Inc., 3-rd edition, 1999.

[149] Yu. L. Pivovarov et al. *Nucl. Inst. Meth. B*, 119:283, 1996.

[150] O. Brüning et al. *The LHC Design Report*. 2004. CERN Report No. 2004-003, `http://lhc.web.cern.ch`.

[151] H. Daido, M. Nishiuchi, and A. S. Pirozhkov. *Rep. Prog. Phys.*, 75(5):056401, 2012.

[152] T. Esirkepov, M. Borghesi, S. V. Bulanov, G. Mourou, and T. Tajima. *Phys. Rev. Lett.*, 92:175003, 2004.

[153] A. Salam and J. C. Ward. *Phys. Lett.*, 13(2):168, 1964.

[154] S. L. Glashow. *Phys. Rev.*, 130:2132, 1963.

[155] S. Weinberg. *Phys. Rev. Lett.*, 19:1264, 1967.

[156] C. S. Wood, S. C. Bennett, D. Cho, B. P. Masterson, J. L. Roberts, C. E. Tanner, and C. E. Wieman. *Science*, 275(5307):1759, 1997.

[157] S. C. Bennett and C. E. Wieman. *Phys. Rev. Lett.*, 82:2484, 1999.

[158] F. Faglioni and P. Lazzeretti. *Phys. Rev. A*, 67:032101, 2003.

[159] W. M. Snow, C. D. Bass, T. D. Bass, B. E. Crawford, K. Gan, B. R. Heckel, D. Luo, D. M. Markoff, A. M. Micherdzinska, H. P. Mumm, J. S. Nico, A. K. Opper, M. Sarsour, E. I. Sharapov, H. E. Swanson, S. B. Walbridge, and V. Zhumabekova. *Phys. Rev. C*, 83(2), 2011.

[160] V. M. Shabaev, A. V. Volotka, C. Kozhuharov, G. Plunien, and Th. Stöhlker. *Phys. Rev. A*, 81:052102, 2010.

[161] J. Sapirstein, K. Pachucki, A. Veitia, and K. T. Cheng. *Phys. Rev. A*, 67:052110, 2003.

[162] L. N. Labzowsky, A. V. Nefiodov, G. Plunien, G. Soff, R. Marrus, and D. Liesen. *Phys. Rev. A*, 63:054105, 2001.

[163] O. L. Zhizhimov and I. B. Khriplovich. *Sov. Phys. JETP*, 55(4), 1982.

[164] I. B. Khriplovich. *Parity Nonconservation in Atomic Phenomena*. OPA, Amsterdam, 1991.

[165] V. P. Mineev, K. Samokhin, and L. D. Landau. *Introduction to Unconventional Superconductivity*. CRC Press, 1999.

[166] R. P. Feynman. *The Feynman lectures on physics. Vol. 3*. Addison-Wesley, 1963.

[167] P. J. Mohr, B. N. Taylor, and D. B. Newell. *Rev. Mod. Phys.*, 84:1527, 2012.

[168] L. J. Buchholtz and G. Zwicknagl. *Phys. Rev. B*, 23:5788, 1981.

[169] N. Cabibbo. *Phys. Rev. Lett.*, 10:531, 1963.

[170] S. S. Saxena, P. Agarwal, K. Ahilan, F. M. Grosche, R. K. W. Haselwimmer, M. J. Steiner, E. Pugh, I. R. Walker, S. R. Julian, P. monthoux, G. G. Lonzarich, A. Huxley, I. Sheikin, D. Braithwaite, and J. Flouquet. *Nature*, 406:587, 2000.

[171] M. Zegrodnik and J. Spalek. *Acta Phys. Pol. A*, 121(2):801, 2012.

[172] D. V. Shopova and D. I. Uzunov. *Phys. Rev. B*, 72:024531, 2005.

[173] B. D. Josephson. *Phys. Lett.*, 1(7):251, 1962.

[174] J. Q. You and F. Nori. *Nature*, 474:589, 2011.

[175] A. A. Golubov, M. Yu. Kupriyanov, and E. Il'ichev. *Rev. Mod. Phys.*, 76:411, 2004.

[176] K. Suzuki, F. Wastin, A. Ochiai, T. Shikama, Y. Suzuki, Y. Shiokawa, T. Mitsugashira, T. Suzuki and T. Komatsubara. *J. All. Comp.*, 213/214:178, 1994.

[177] P. Boulet, A. Daoudi, M. Potel, H. Noel, G.M. Gross, G. Andre, and F. Bouree. *J. All. Comp.*, 247(1/2):104, 1997.

[178] Springer Materials Database. `www.springermaterials.com`.

[179] C. A. Sackett. *Nature*, 505:166, 2014.

[180] A. Pálffy, Z. Harman, A. Surzhykov, and U. D. Jentschura. *Phys. Rev. A*, 75:012712, 2007.

[181] J. R. Taylor. *Scattering Theory*. New York, 2000.

[182] X. Jian, Jingchuan Zhang, Qiang Gu, and Richard A. Klemm. *Phys. Rev. B*, 80:224514, 2009.

[183] A. A. Abrikosov, L. P. Gor'kov, and I. E. Dzyaloshinskii. *Methods of Quantum Field Theory in Statistical Physics*. Pergamon, 1965.

[184] C. Kittel. *Introduction to Solid State Physics*. John Wiley & Sons, 1953.

[185] A. Huxley, Ilya Sheikin, Eric Ressouche, Nolwenn Kernavanois, Daniel Braithwaite, Roberto Calemczuk, and Jacques Flouquet. *Phys. Rev. B*, 63:144519, 2001.

Acknowledgments

I would like to express my special appreciation and thanks to my advisor Priv.-Doz. Dr. Zoltán Harman. I would like to thank you for encouraging my research and for allowing me to grow as a research scientist. Your advice on both, research and on my career, has been priceless. I would especially like to thank Hon. Prof. Christoph H. Keitel for his constant interest and kind support of my work. Very useful discussions with Dr. Stanislav Tashenov are also kindly appreciated.

I would also like to thank all the members of our division for Theoretical Quantum Dynamics and Quantum Electrodynamics at Max Planck Institute for Nuclear Physics in Heidelberg. The useful discussions and your support helped me a lot within the work on my PhD thesis. I separately thank Dr. Stefano Cavaletto, Dr. Natalia Oreshkina, Bastian Sikora, Dr. Oleg Skoromnik and Dr. Jacek Zatorski for proofreading of this thesis.

I would also like to thank Prof. Dr. Jürgen Berges, Priv.-Doz. Dr. José Ramón Crespo López-Urrutia and Prof. Dr. Ullrich Schwarz for serving as my committee members.

A special thanks to my family. I would like express the sincere appreciation to my parents.

At the end I would like to thank my beloved wife Ekaterina. Your love and patience are helping me instantly.